EBERHARD-KARLS-UNIVERSITÄT
TÜBINGEN
Fakultät für Mathematik und Physik

UNIVERSITÀ DEGLI STUDI
DI TRENTO
Facoltà di Scienze MM. FF. e NN.

Diplomarbeit-Elaborato finale

Corso di laurea specialistica in fisica-Diplomstudiengang Physik

A simulation study of space based missions for Ultra High Energy Cosmic Ray search

**Simulationsstudie
eines weltraumgestützten
Observatoriums für ultra hoch
energetische kosmische Strahlung**

**Studio di simulazione
di un osservatorio
nello spazio per la rivelazione
di raggi cosmici ad energia ultra alta**

Betreuer: Prof. Dr. Andrea Santangelo
Relatore: Prof. Dr. Stefano Vitale

A.A. 2007/2008

Diplomand/Laureando: Francesco Fenu

Kepler center-IAAT Tübingen
June 2008

Eberhard Karls
Universität
Tübingen

EBERHARD-KARLS-UNIVERSITÄT
TÜBINGEN
Fakultät für Mathematik und Physik

UNIVERSITÀ DEGLI STUDI
DI TRENTO

UNIVERSITÀ DEGLI STUDI
DI TRENTO
Facoltà di Scienze MM. FF. e NN.

A simulation study of space based missions for Ultra High Energy Cosmic Ray search

Diplomarbeit / Elaborato finale

Corso di laurea specialistica in fisica-Diplomstudiengang Physik
A.A. 2007/2008

Francesco Fenu

Contents

Introduction - UHECRs: a new frontier in astronomy?

Although Cosmic Rays science is already more than 90 years old many basic questions on their nature and origin remain still unanswered. It is in general believed that the understanding of these extrasolar and extragalactic particles will probably challenge our fundamental view of the universe. In particular new astrophysics and possibly new physics could emerge from the understanding of the part of the spectrum at highest energies, in excess of 10^{19} eV, that is in the energy region of Ultra High Energy Cosmic Ray. Because of their extreme energies they could probe physics not accessible to the current ground based accelerator while as well opening new observational windows on the Universe.

Many new theories have been developed to try to explain the existence of particles with energies up to 3×10^{20} eV. Where are those particles coming from and which physical mechanism could be capable of creating them is still unknown. Theoretical studies are aimed either to the search of acceleration mechanisms capable of bringing particles up to these energies (Bottom-up production) or to implement still speculative models capable of producing particles with such an enormous energy from the decay of some supermassive particle (Top-down models). The existence of non Standard Model particles (like WIMPS) or other exotic phenomena like strings or topological defects could be at the base of the creation of those particles. In this view could be extremely interesting to check if those theories are confirmed by observations.

Another really great chance offered by Cosmic Rays is the new observational windows that could be opened on the universe by these messengers. In fact at the present time we have information on our universe just from electromagnetic radiation. Ultra High Energy charged Cosmic Rays or neutrinos could be used for future observations of objects not observable in any other observational range.

However there is still high uncertainty on the total flux, the energy spectrum, the existence of small and/or large scale anisotropies in the flux of

Ultra High Energy Cosmic Rays. This is due to the low statistics of measured events at these extreme energies. What we need to provide an answer to the still open observational questions is larger statistics. Worth to be noticed is the fact that at the present time has started its activity the Auger South array (3.000 km^2), up to now the largest running ground based array for the search of Ultra High Energy Cosmic rays. In the next years an even bigger Auger North array (21.000 km^2) is also planned. It is clear however that to further improve statistics, ground arrays are no longer enough. It has been in fact suggested, that, to improve the statistics by a factor of 10 or more, the next experimental efforts should be devoted to the monitoring of much bigger amounts of atmosphere from space. From space we can reach exposures up to several orders of magnitude greater than the one actually reachable from ground.

The idea of observing Extended Air Showers from Space was developed already many years ago, in the late seventies, but it has been deeply studied just in the last decade. The basic idea is the observation of the (300-400 nm) UV fluorescence tracks of relativistically propagating Ultra High Energies Cosmic Ray in the atmosphere. In this thesis we will mainly investigate the expected performances of the Extreme Universe Space Observatory "family" of experiments: from the original concept of EUSO onboard the ESA Columbus module, to JEM-EUSO (EUSO onboard the Japanese ISS Kibo module) and S-EUSO (a free flyer concept).

Aim of our thesis is therefore the assessment of the capabilities of a future Cosmic Rays space observatory. Which is the threshold in energy, the energy and direction resolution are fundamental aspects that must be studied before the construction of any space mission of this kind. In order to make this study we used the ESAF code that is the end to end simulation code developed in the framework of EUSO. We adapted ESAF to the JEM-EUSO instrument and we began the implementation of S-EUSO.

The thesis is organized as follows: the first chapter is devoted to some general aspect about Cosmic Rays science, the second to the Extended Air Shower detection and the third to the description of the instruments we will simulate. Then the fourth will be a description of the software and in the last one we will present and comment the results we obtained.

Chapter 1

Observational properties and production mechanisms of Cosmic Rays

1.1 Introduction

1.1.1 Birth of a new science

The era of Cosmic Ray (CR) science began in the first decade of the twentieth century after the discovery of the ionizing radiation emitted by radioactive materials [1] [4]. It was, in fact, very well known that electroscopes discharged spontaneously near sources of natural radioactivity. However, another specific feature had also been observed: the existence of ionizing radiation even in absence of radioactive sources, in other words the existence of "background" radiation. It was Rutherford who firstly suggested natural radioactivity from the Earth as the candidate for being the source of this background radiation and in fact it was well known that rocks are natural radioactive sources. In 1910 a series of key experiments was conducted by Theodore Wulf [2] who measured the ionizing radiation to fall down from 6×10^6 ions m $^{-3}$ to 3.5×10^6 ions m^{-3} from the bottom to the top of the Eiffel Tower, much less than what expected on the base of the absorption coefficient of gamma rays. In the years 1911-1913, the Austrian physicist Victor F. Hess started a campaign of balloon flights carrying electrometers up to more than 5000m. Hess results were surprising: the ionization rate was found to decrease up to $\sim$ 1 km above the sea level and then to strongly increase with the altitude reaching a flux four times higher than the one measured at sea level. Hess explained this feature in the radiation flux as the result of a strong injection of radiation from the outer space [3]. This idea, confirmed

by several experiments, led to the birth of Cosmic Ray science and brought Hess to be awarded the Nobel prize in 1936. It was Millikan, who believed these were gamma rays with more penetrating power, to name, in 1925, the unknown radiation *Cosmic Rays.* Other important discoveries were done in the following years. The first detection in 1929 of CR's secondaries in cloud chamber was made by Skobeltsyn.

Always in the same year, Böthe and Kolhörster demonstrated the charged particle nature of CRs measuring the correlation between count rates of two different Geiger counters (see Fig. 1.1) placed one above the other and separated by a thick absorber [6]. If CRs were γ photon primaries one would have observed just uncorrelated events in the two Geigers. In fact a photon originated shower is able to generate mainly electrons as secondaries and those particles are not penetrating enough to trigger both of the counters. The fact that correlation between counts occurred in both instruments was a clear indication that primaries were charged particles. Further proofs of the charged nature of CRs has been given by J. Clay who saw a dependency in the CR flux with the geographic latitude [11]. Some year later B. Rossi predicted the so called east west effect [12] an asymmetry in the arrival direction of the CR. Both of those effects were due to the presence of the geomagnetic field that affects the trajectory of charged particles. Those results definitively confirmed the charged nature of CR primaries.

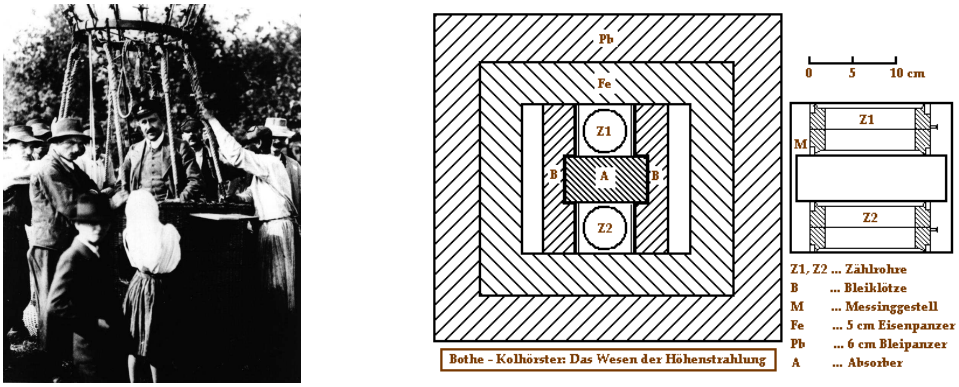

Figure 1.1: Hess pioneering flights [5] Boethe and Kolhoerster apparatus [6].

Some year later P. Auger observed the correlation between the count rates of two horizontally separated counters [24] [26]. Those were the first observations of Extended Air Showers (EAS) which is a "bubble" of secondaries particles generated by high energy primaries moving trough the atmosphere (see chapt. 2). It was demonstrated using the width of the shower front that the energy of the primary could be as high as 10^{14} eV.

In order to reach higher energies was necessary to wait till mid forties. In fact in this period began the construction of giant arrays of particle detectors. The first example was that build by G. Zatsepin in Pamir station. At the end of the forties it was therefore clear that CRs were high energy particles coming from the space. It was not clear which could have been the mechanism capable of producing them. The first hint to solve this puzzle was given by E. Fermi in 1949 who proposed the mechanism since then called with his name. He essentially postulated a stochastic process capable of accelerating particles to very high energy through a repetitive process (see sec. 1.2). Up to now this is the only suitable candidate capable of explaining (but not completely) the Cosmic Ray's spectrum.

In the fifties balloon flights and later the beginning of the space era made possible an extraordinary improvement in the knowledge of the CR nature. The shape of the spectrum became clear and finally in 1963 J.Linsley announced the discovery of the highest energy particle since then known [9]. This discovery at the Volcano Ranch array [10] is considered as the birth of the Ultra High Energy Cosmic Ray (UHECR) science.

In 1966 an important step in the field was the prediction of the so called Greisen Zatsepin Kuzmin (GZK) effect by Greisen Zatsepin & Kuzmin that is the suppression in the spectrum of events due to photopion production of protons with the Cosmic Microwave Background observed around 5×10^{19} eV (see sec. 1.3.1).

The first attempt to detect a CR shower by means of fluorescence light was done at Cornell university by K. Greisen in 1967 [87]. At the time they detected light from CR shower using a system of 500 photomultipliers arranged in 10 modules. Each of the modules was equipped with a Fresnel Lens pointing to a portion of the sky. This experiment was the first of a new family of detectors: the atmospheric fluorescence detectors.

Always in 1967 the Haverah Park array became operative [13]. This was an array of water Cerenkov detectors operating for more than 20 years aiming at detection of particles of the highest part of the spectrum. After 20 years 4 particles with an energy above 10^{20} eV were detected.

Another really important CR's observatory was Fly's eye [15] . This experiment took data from 1981 to 1993 measuring the highest energy particle ever seen: in November 1991 a shower having energy of $3.2 * 10^{20}$ eV was observed. As continuation of this last experiment in 1994 a new fluorescence detector has been build in the site where previously Fly's eye was located. This was the HiRes array [17], a system of two arrays of UV telescopes on the top of two hills. Those stations will detect at the same time a shower developing in the atmosphere. The fact that the shower is detected by both stations 13 km far from each other will make possible a better reconstruction

of the direction. This observatory is still operating.

The Akeno Giant Air Shower Array (AGASA) [22] [23], was an array of particle detectors having an area of more than 100 km^2. The array was build by 111 surface scintillation devices and 27 underground muon detectors. This is up to the time the array that has measured the highest number (12) of events over 10^{20} eV.

We will talk about the controversy between AGASA and High Resolution Fly's Eye (HiRes) fluxes in section 1.3.2.

In these years is becoming operative another UHECR observatory: the Pierre Auger Observatory (PAO) [24] [26]. Its aim is to give an unprecedented reach statistics of events by combining in the same array the two measurements techniques (fluorescence and particle detectors).

Future instruments and in particular space based arrays are described in chapt. 3.

Although CRs have been discovered since almost 100 years a large number of questions still remains opened: where are those particles coming from? How have those particles been produced? How do they propagate to the Earth? Furthermore many aspects of UHECRs science are challenging the current physics scenario. This is the reason why this science is generating big interest in the community. The next generation observatories is for sure bringing a clearer view on the astrophysical nature of CR and probably many surprises even in theoretical physics.

1.1.2 Observational evidences: Composition

The composition of CR on top of the atmosphere is summarized in Table 1.1.2 . This composition refers to the energy range 10^8 - 10^{10} eV where the flux is high [74].

Particle type	Percentage
Protons	86%
Alpha particles	11%
Electrons	2%
Heavier elements	1%

Table 1.1: CR's composition between 10^8 - 10^{10} eV [27].

In Fig. 1.2 we can see the abundance of the elements on the top of the atmosphere compared with solar system abundances.

We see that unless the two spectra are similar they present some significant difference. Those differences explain a lot about the propagation of CRs.

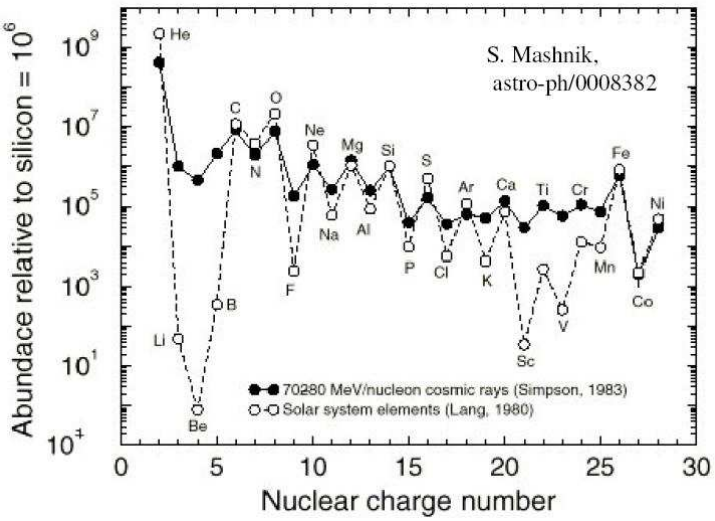

Figure 1.2: Abundance of CRs species.

First of all, we assume that the produced CR composition is the same as the composition of solar system. This is not by itself obvious but we can assume that the sun is a typical "citizen" of the galaxy. This means a second generation star that formed from the collapse of a nebula. For this reason observing spectral lines in the sun and analyzing meteorites we can expect a similar composition to the case of the supernova remnant (were the CR acceleration took place).

We can therefore say that if there is a difference in the abundance ratios something must have happened between the production site and the observer. After those assumptions we can check a posteriori if the entire picture is compatible with the observed ratios.

First we observe in Fig. 1.2 the fact that in CR composition there is an overabundance of light elements (like beryllium, lithium and boron) compared with solar system abundances. Second, an overabundance in CRs of the elements just below iron is observed. In the CR there is also an underabundance of hydrogen and helium compared to the heavy elements.

The reason for those differences is in a process called spallation [75]. The heavy CRs will be confined in the galactic volume and will encounter the very abundant nuclei of hydrogen in the ISM. This will cause the fragmentation process schematized in figure 1.3.

Essentially what happens is that there is a production of lighter elements and a destruction of heavier.

Writing the transfer equation will be possible to describe how much

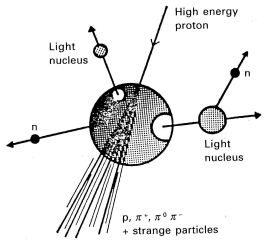

Figure 1.3: Simplified view of spallation scattering [76].

matter the CRs have traversed and to have an indication of how much time do our particle remained in the galaxy. From this point we learn that the particle should be confined in our galaxy. In fact from the solution of the transfer equation we see that particles have flown a really long time in an environment with densities comparable with the interstellar medium density. In this time they should have traversed thousands of times the galactic thickness.

However there is another essential point: the information carried by CR clocks. Those are radioactive particles that decay during the flight. From the ratio between some isotope we can therefore infer the age of CRs. This is however a much longer time than the one obtained by the spallation method. Particles however could not have flown in galaxy disc for such a long time otherwise we would measure much stronger spallation features (all the heavy elements would be destructed and we would observe just lighter elements). The two measurements are compatible just in the case we postulate the particles are flying in a lower density environment. This volume turns out to be the halo of the galaxy already seen in radio waves and around some other galaxy. Composition of CRs at UHE is still subject of debate and no conclusive evidence has been obtained up to now.

The final conclusion of this chapter is that we can learn from CRs also a lot of information about our galactic magnetic fields and the structure of the galaxy itself.

1.1.3 Observational evidences: Spectrum

The spectrum of CRs extends for 13 orders of magnitude in energy ranging from 10^8 to 10^{21} eV and for 33 order of magnitudes in flux from 10^4 to 10^{-29} particles per $(m^2 * sr * GeV)$.

In Fig. 1.5 we report the "all particle" spectrum obtained by S. Swordy of Chicago University. As can be seen, there is a flattening of the spectrum at low energy. This is an effect due to the solar wind and interplanetary

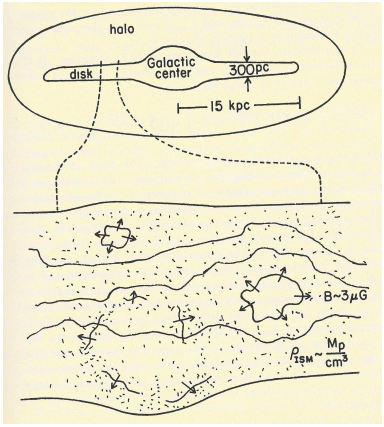

Figure 1.4: Simplified view of CRs confinement volume in the galaxy.

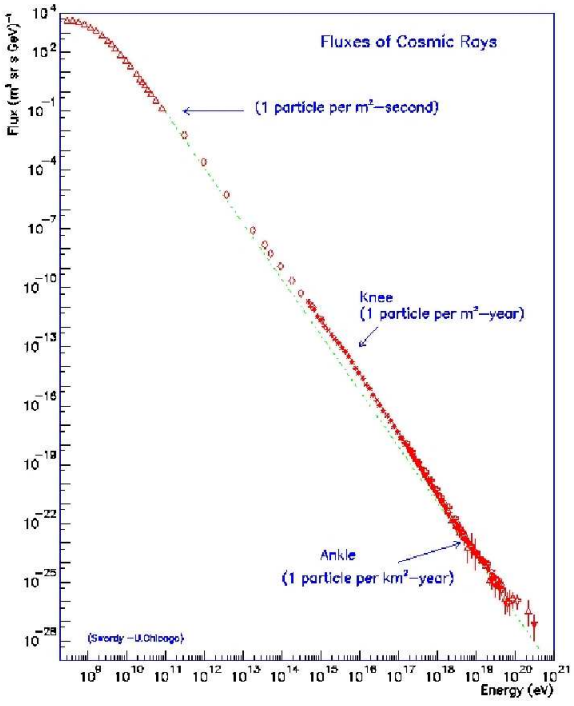

Figure 1.5: CR's spectrum [30].

magnetic field. In fact the lower energy particles are kept away from the solar system. For the same reason a correlation of the lower part of the spectrum with the solar activity is observed. When the activity of the sun is high

we observe less particles in this range of energy. At even lower energies we observe a diminishing flux for decreasing energies and at the lowest energies we would again observe an increasing flux for decreasing energies (this is due to the anomalous CRs component).

Above 10^{10} eV the flux is not more correlated with the solar activity and the spectrum is generally described by a power law $\frac{dN}{dE} = E^{-\gamma}$ where E is the primary particle energy and the spectral index is $\gamma \simeq 2.7$. Several features are however observed in the spectrum. At $E \sim 10^{15}\ eV$ the spectral index γ changes to $\simeq 3.3$, in other words a softening in the spectrum is observed. This features is usually called *the knee*. The knee has been observed by Kulikov and Khristiansen in 1956 [32] . This transition has been explained both with a loss of efficiency in the production mechanism (see section 1.2) and/or a loss in the capability of the Galactic Magnetic field (10^{-4} - 10^{-6} G [31])to confine CRs in the galactic volume. The physics in this part of the spectrum is however not fully explained. A comprehensive review on the nature of the knee has not been written in the scope of this thesis. The interested reader can find an overview in [37].

Another softening in the spectrum has been observed by several experiments [57] . This transition occurs around $10^{17.8}$ - $10^{17.9}$ eV. The slope goes from a steepness of ~ 3 to $\sim$ 3.2-3.3. This transition is called *second knee*. Also on the nature of this *second knee* there is still an open debate.

At $E \sim 10^{18}$ eV the flux flattens again to a $\gamma \simeq 2.5$. This feature is called *the ankle*. Above the ankle no confinement in our galaxy is possible , implying that CRs produced by galactic accelerators will escape our galaxy. It has therefore been suggested that at *the ankle* we do observe the rise of an extragalactic component in the CR's spectrum [33].

However there is not a total agreement about this theoretical interpretation. In recent years especially after the second knee discovery a new theory has been developed by Berezinsky et al. [34] [35] [36]. The authors interpret features like *the knees* uniquely as a loss of efficiency in CRs production of the supernovas. The first knee would be associated with protons while the second knee would be associated with iron. Between first and second *knee* we should therefore observe a heavier composition. This model has in this range the advantage of allowing a better source economy. In fact in the traditional view between *ankle* and the *knee* other galactic sources (other than Supernovae) would have to be present. According to the Berezinsky model the transition between galactic and extragalactic component would occur at the second knee. *The ankle* would therefore be the result of another effect: the interaction between CRs and CMB. CRs will interact with the Cosmic Microwave Background (CMB) by means of two processes. The first one is the photopion production (see chapter on GZK effect). The second is

the pair production generated by CMB photons (see formula 1.1).

$$p + \gamma \rightarrow p + e^+ + e^- \tag{1.1}$$

The latter effect starts to became dominant above 10^{18} eV. In the end, the effect of both pair production and photopion production processes will be visible in the flux plot with the hardening of the spectrum after *the ankle* as result of the pair production interaction.

At even higher energies (above 4×10^{19} eV) the GZK cut-off is expected.

The combined effect of those processes is also visible in the modification factor plot where a dip between 10^{18} and 3×10^{19} eV can be seen (see [36]).

1.2 Production mechanisms

One of the crucial questions in CR research is which physical mechanism is capable of accelerating particles up to energies of 3×10^{20} eV. In fact the sun, the biggest source of CRs arriving at the earth, is capable of producing particles just to $E \sim 10^{10}$ eV.

It was Enrico Fermi who, in 1949 [64], firstly suggested an acceleration mechanism capable of transferring to a single particle the kinetic energy stored in galactic clouds via multiple repeated interactions. This mechanism, known as Fermi Mechanism, is up to the present time the only mechanism theoretically capable of accelerating protons up to an energy of 10^{15} eV. Above this energy, there is still an open debate on how the Fermi mechanisms could be extended to the highest energies observed. We will present here just some qualitative overview of the mechanisms. We invite the reader to look in [58] in order to have a more detailed explanation.

1.2.1 Second order Fermi Mechanism

The basic idea proposed by Fermi was that a particle will encounter a moving cloud scattering within it many times in the magnetic field turbulences and coming out with an increased energy [58]. After multiple encounters with the same or other clouds the energy could be increased up to very high values.

However as explained in [65] this mechanism is not able of accelerating particles up to very high energies. Even if this model reproduces the shape of the spectrum it results to be not enough efficient. We will see that the average gain in each encounter will be of the order of β_{cl}^2 (Lorentz factor of the cloud) which is too low. In fact making the calculation we obtain $\beta_{cl}^2 \simeq 10^{-7}$. Each encounter will increase the energy just by this factor. Furthermore the probability that a particle will encounter many clouds is really low and not

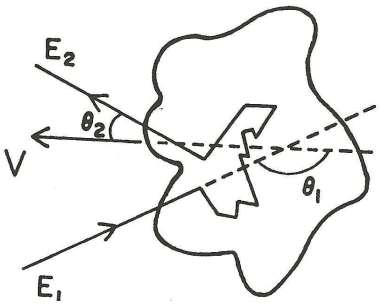

Figure 1.6: Second order Fermi mechanism.

compatible with the extreme energies observed in nature. In conclusion we have to look for a more efficient version of the Fermi mechanism.

1.2.2 First order Fermi Mechanism or shock acceleration

Even if in the previous paragraph we saw that the second order Fermi mechanism cannot explain by itself the CRs production we will now see that something of Fermi's idea will succeed if applied to a particular environment. This environment is the shocked gas (for example) in the proximity of a Supernova Remnant (SNR) [65] .

In the case of a supernova the SNR speed will exceed the sound velocity in the interstellar medium. This will cause the formation of a sharp transition in the thermodynamical quantities in the proximity of what is called shock.

A particle being on one side of the shock will acquire a zero mean velocity with respect to the gas around it after a certain number of scatterings. Every time the particle will traverse the shock it will encounter the gas on the other side always with a head-on collision.

In the end considering all the possible angles of entering and exit the average gain will be:

$$\xi \sim 4/3\beta_s \tag{1.2}$$

Where β_s is the Lorentz factor of the shock. Equation 1.2 is the reason of the name first order Fermi mechanism. The efficiency here is much higher than in the case seen in the previous chapter. This makes this model a more suitable candidate for being the production mechanism for CRs. Furthermore the supernova shock is much faster than the magnetic cloud seen before.

A further feature this model can reproduce is the shape of the CR spectrum [65].

Another point is the maximum energy reachable. Here we have to take into account essentially two points. First of all the dimension of the acceleration

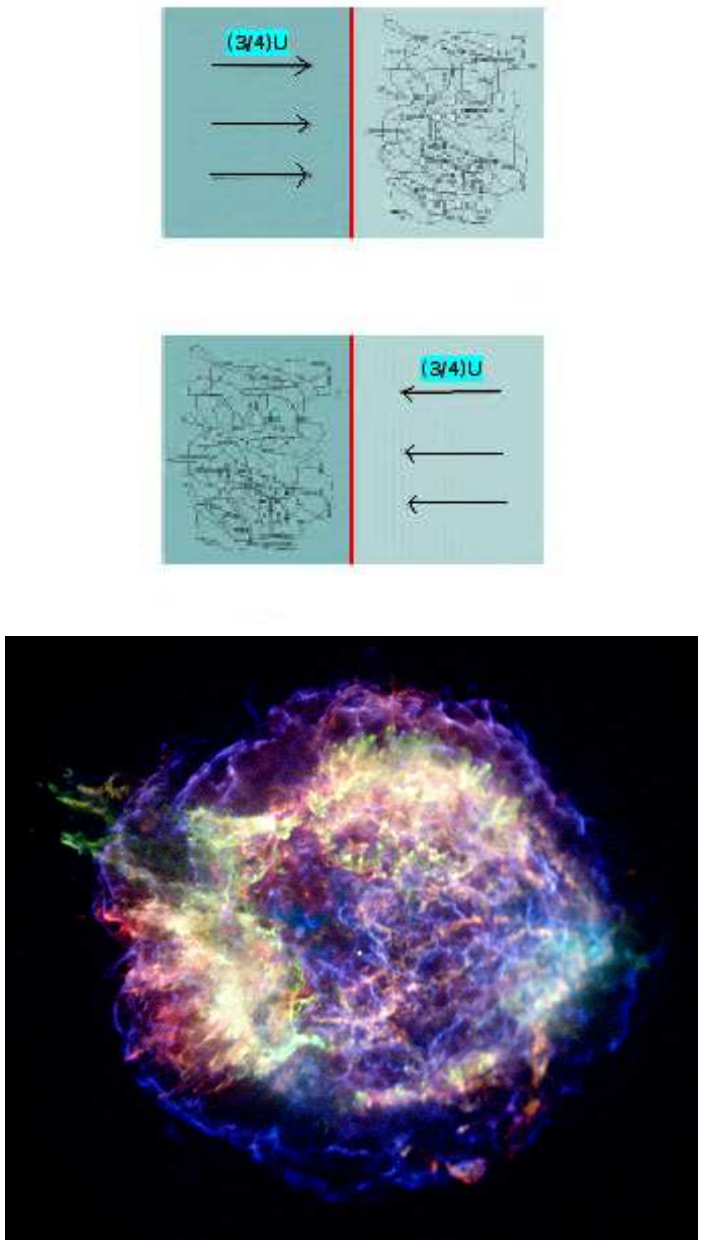

Figure 1.7: A scheme of first order Fermi mechanism [72] and a SNR [73].

engine has to be much larger than the gyro-radius of the particle. In fact when the energy increases the magnetic fields in the gases before and after the shock will be less able to bend the particle trajectory. The particle magnetic rigidity will increase with the energy. In one word the probability of escape

from the SNR region will increase. The second factor is the accelerator lifetime. The SNR will stay in the stage of being capable of accelerating particles just for more or less 1000 years. This limits the maximum number of shock crossings. In the end more quantitative calculations give a maximum energy of the order of 10^{15} eV for protons. This is already a fist step in order to explain the spectrum of CRs. However the range above this energy,as we will see in section 1.3 remains up to the time totally unexplained [1].

1.3 Ultra High Energy Cosmic Rays

UHECR are still a mystery. First of all we do not know the production mechanisms. At the moment anyone would be able to produce particles with an energy up to 10^{21} eV. Many theories have been developed to solve this puzzle. They will group in two categories: bottom-up and top-down mechanisms. The bottom-up theories are those explaining the high energies as the result of an acceleration process while top down as the result of the decay of super heavy particles (X particles) not predicted by Standard Model.

We summarize some of them here [90] :

- Bottom-Up
  - Diffusion acceleration (Fermi Mechanism)
  - Unipolar induction (Induced electric field by torsion of magnetic fields lines for example in Neutron Stars)

[1] But, are supernova remnants capable to explain the observed flux of CRs? Indeed if we consider a galactic volume of the order of $10^{67} cm^3$, a CRs energy density of the order of $0.5\text{eV}/cm^3$ and $t_{GD} \sim 10^7$ years. We define t_{GD} like the characteristic time a CR will remain confined in the galaxy (see section 1.1.2) . We make an estimate of the energy necessary to replenish the loss of CR in out galaxy:

$$L_{CR} = \frac{vol_{GD}\rho_E}{t_{GD}} \simeq 3 \times 10^{40} erg/sec \tag{1.3}$$

This is fully compatible with the theory of acceleration from SNRs. We can expect in our galaxy 3 supernovae each century each of them being capable of accelerating CRs for 1000 years. Each of them will also produce a certain amount of energy that on average is known. In the end we conclude that being the energy produced by SNRs in the galaxy:

$$L_{SNR} \simeq 10^{42} erg/sec \tag{1.4}$$

even an efficiency of 0.01 would be able of producing the population of CR in the galaxy. The SNRs are therefore very good candidates for being responsible of CRs spectrum up to the knee.

  - Non linear particle wave acceleration

- Top-Down
  - Production of X particles by topological defects
  - Production of X particles by Wipzilla's decay

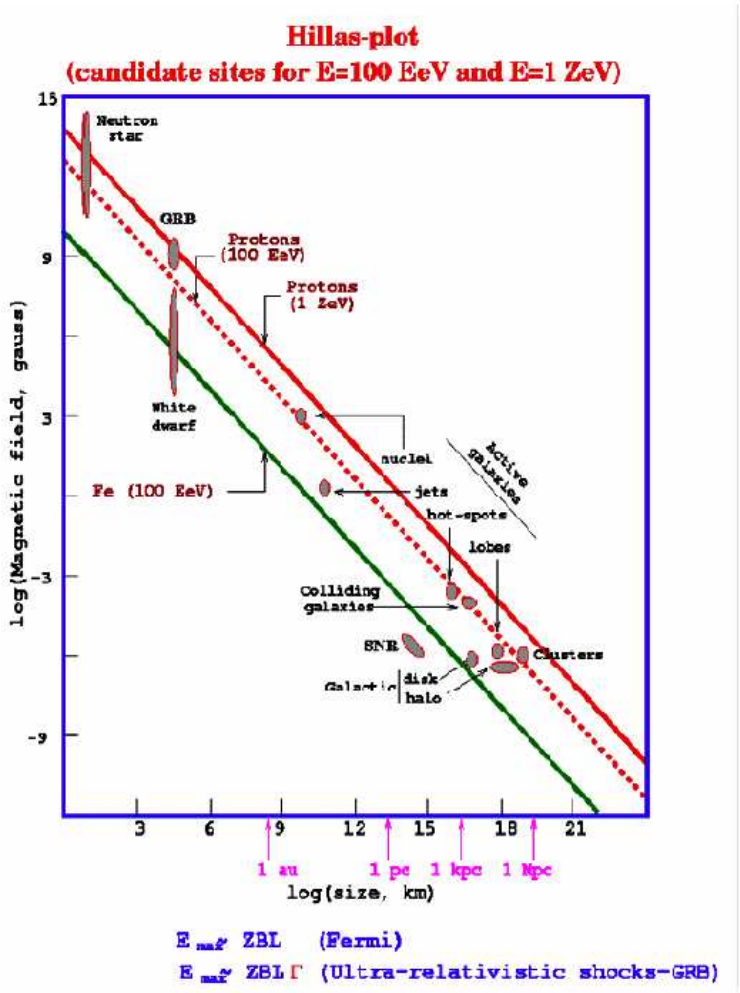

Figure 1.8: Hillas plot [38].

Up to the time none of those models is able to explain the observed production. However recently some hint of clustering of CRs coming from AGN has been found [78] [79]. If confirmed this result would make Bottom-Up theories much more plausible.

Concerning the bottom-up models there is no astrophysical object proven to be capable of accelerating particles up to 10^{21} eV and even if we extend the Fermi mechanism up to those energies problems remain.

The minimum requirement for an acceleration site is the containment in the acceleration region. This leads to the relation for the maximum energy.

$$E_{max} = \gamma eZBR \tag{1.5}$$

Where e is the proton charge, Z the atomic number, B the magnetic field and R the dimension of the accelerator. This doesn't mean that astrophysical objects are able to produce particles with such an energy but simply that they could (assuming a suitable acceleration mechanism is provided). We stress however that the maximum energy reachable does not depend on the mechanism.

In order to look for plausible UHECRs sources we can show the Hillas plot (see Fig. 1.8). Hillas, in his paper in 1984 [38], reviewed the possible sources of cosmic rays. In his plot we have on the x axis the size of the accelerator and on the y axis the magnetic field. He put on this plot many astrophysical objects. Furthermore it's possible to draw the relation between magnetic field and size in order to reach a particular energy. If an object is under the line characterizing 10^{20} eV than it would be impossible to produce particles with such an energy for this object. We see that the basic condition for accelerating UHECR are satisfied just by few candidates.

Let's give a short overview of those potential accelerators. All the sources listed in the following are studied assuming modellizations with the most optimistic parameters.

The first candidate could be in the shocks in structure formation due to gravitational attraction [39]. Those shocks exceeding several tenths of Mpc are originated by accretion flows during structures formation. As an example: a 50 Mpc shock could be able of accelerating particles up to 10^{20} eV if the condition of a nG intergalactic and μG in the shock magnetic fields are reached. There are however problems in the efficiency of this mechanism and furthermore the fact that those particles will have to make a really long path will make them suffer from pair production and photopion production that will degrade the energy.

Clusters of galaxies could be other suitable candidates. Magnetic fields of 5 μG and dimensions of 550 kpc have been observed [40]. According to Hillas criteria those could be a possible accelerator of UHECRs. However more careful studies have shown that in this environment energies just up to 10^{19} eV can be reached [41].

Other possibility could be given by radiogalaxies [42]. It has been suggested

that hot spots in Fanaroff-Riley type II galaxies could accelerate CRs up to 10^{21} eV. Hot spots are termination shocks of the jets exiting the galaxy and encountering the intergalactic medium. They have dimensions up to 100 kpc and an estimated magnetic field up to 10 μG. Furthermore energy losses should not be a critical aspect here. Those considerations make radiogalaxies good candidates for being CRs accelerators.

Going toward smaller objects we will encounter Active Galactic Nuclei (AGN). Those objects could be source of UHECRs. In fact their central engine is believed to have fields of the order of 5G in a region having size of 0.02 pc [45] . The main problem is the fact that being the central part of the AGN a region with a really high photon density a large energy loss is expected. One possibility could be that as a result of pion production neutron are produced [46]. Neutrons are not confined and therefore they can escape the central region. Once they left this region neutrons will decay in protons. However this will work just for neutrons with an energy not much higher than 10^{18} eV. Always related to AGNs the acceleration could occur in the shocks at the boundary between jets and intergalactic medium. Actually as we already said a correlation between AGNs and arrival direction of UHECRs has been probably detected [78] [79]. Those studies by the Auger collaboration made AGNs together with Gamma Ray Burst (GRB) the best candidates for being at the origin of the highest part of the CR spectrum.

The extreme case of acceleration in a jet is the case of GRB. Those phenomena are giant outbursts in gamma range. They are of cosmological origin (as proven by their redshift). They originate in jets. The first suggestion that GRB are at the origin of the highest part of the spectrum originates from the fact that two of the highest energy CRs arrivals direction is coincident with some GRB [47] [48] [49]. Doubts are all related with the large distance of those sources. Particle's energy should therefore be degraded.

Other possible sites are shocks originated in galaxies collisions [50] . These shocks have size of the order of 30 kpc. A shock field of the order of 20 μG could accelerate particle up to 10^{20} eV.

The last possibility are pulsars. Those really compact objects have fields larger than 10^{12} G. Those objects could accelerate protons up to 10^{20} eV. In those environments there is not a shock acceleration but a direct one in the really strong potential differences originated in the proximity of the rotating Neutron Star (NS). Other possibility would be of an acceleration of iron nuclei in the magneto dynamic winds in the proximity of young neutron stars. In NSs scenarios UHECR would be of galactic origin therefore all the problems related to energy degradation would be avoided.

As we already said CRs could be generated by some top-down model. Those models state that UHECR are generated in the decay of super massive

X particles (having mass of the order of 10^{25} eV). How those particles are generated (or even if they can exist) has not been proven at all. One distinctive feature is the flat energy spectrum of particles they can generate. Another feature is the different predicted composition compared to bottom-up models. The decay of those massive particles produces in the end nucleons and mesons. As result in those models neutrinos and γs are the predominant part compared to nucleons.

On the production mechanisms of X particles there are many speculative models. We will cite some of them. They are essentially grouped in two classes: the first is related to topological defects and the other is related to cold dark matter.

In the category topological defects we find for example monopoles. In 1983 Hill [51] proposed the monopole annihilation model. Monopoles are point-like topological defects that could have originated in the early universe. A monopole and a anti-monopole will annihilate and form a spectrum of particles. The spectrum could be approximated to a power law $E^{-\frac{3}{2}}$ with a cutoff around 10^{25} eV. Other topological defects are cosmic strings. Those are one dimensional defects whose mass is of the order of $3 \times 10^{10} M_{\odot}$ per pc. There are many models of strings being considered as UHECRs sources. Superconducting strings [52], emission of X at cusps in ordinary strings and hybrid models [53] are just some examples of what could be tried with those models.

In the category cold dark matter we find all those models using the decay of heavy relics from the early universe [54].

Worth to mention are also a number of hybrid models involving many never observed processes (like Z-burst model) [55] [56].

We have however to say that measured neutrino and γ flux puts strong constraints on these models.

1.3.1 GZK effect

The second part of the mystery is how UHECRs propagate to Earth. In 1966 Greisen [82] and independently Zatsepin and Kuzmin [83] predicted the effect since then known as GZK effect. These authors calculated that a proton having an energy above $5 * 10^{19}$ eV should suffer of an energy degradation process due to photopionproduction with CMB photons. Here we can have a look to the processes that we are considering.

$$\gamma + p \rightarrow n + \pi^{+} \tag{1.6}$$

$$\gamma + p \rightarrow p + \pi^0 \rightarrow p + \gamma + \gamma \tag{1.7}$$

$$\gamma + p \rightarrow p + n\pi \tag{1.8}$$

As result we will obtain other nucleons having lower energy as the primary and of course photons, neutrinos and muons.

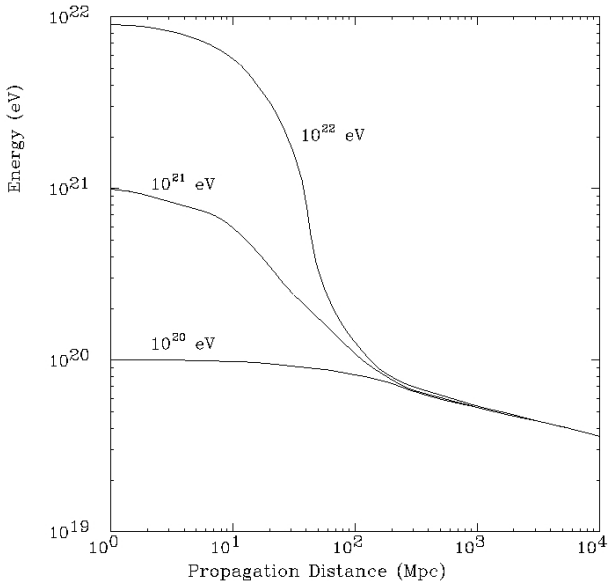

Figure 1.9: Degradation of proton energy due to GZK effect [59].

It has been calculated by the authors of GZK papers that protons with such an energy won't have the possibility to traverse more than some Mpc in the intergalactic medium which is filled with CMB . Above this energy no protons should be observed unless:

- Nearer sources are present
- Some unknown physical mechanism is producing such UHECR in the vicinity of the earth
- The GZK model is not correct.

For both the first two cases there are some difficulties. For the first hypothesis at any wavelenght no clear counterpart is thought to be the site of cosmic ray production. Concerning the second case we could try to explain

the production in the vicinity of the earth with some top down mechanism. However we are here in a fully speculative model domain: none of these theories has been proven yet.

As a matter of fact such particles have been observed and up to the moment it still remains an highly uncertain picture about the origin of these particles. Even the presence of the GZK itself is not guaranteed even if in the last years some observation seems to give a hint that would suggest the existence of an flux decline above $4 * 10^{19}$ eV.

Heavier particles are suffering by this kind of losses starting from a higher energy. Other messengers such as neutrinos are not even suffering this effect. This could be the way by which high energy particles avoid the GZK cutoff.

As conclusion the questions of whether this cutoff exists, where are super GZK particles coming from and which eventual physical process should produce those particle are to be addressed by a future space mission.

1.3.2 Agasa-HiRes-Auger

In recent years data from the detectors AGASA [68] [69]and HiRes [66] [67] have originated a debate on UHECRs. As we will see in chapter 2 the first one is a fluorescence detector the second a ground particle detector for CRs secondaries. The two arrays do not agree in the measurement of the flux at extreme energies.

As can be seen in Fig. 1.10 the flux measured by AGASA is not compliant with the GZK effect while HiRes data do. More recently the puzzle has been solved by the PAO [70]. The basic idea of this technique is to combine the two techniques in order to calibrate the two methods. An array of 1600 particle detectors are deployed in the Pampa in Argentina together with 4 fluorescence telescopes observing the atmosphere above the detectors from some hill around the detection area. The surface of this array is more than 3000 km^2. We invite the reader to look in chapter 2 for a better explanation on the Auger structure.

Another array called Auger North in the north hemisphere with an area of 21000 km^2 is planned.

The preliminary results of Auger are apparently showing a result compliant with the GZK flux strengthening the hypothesis of wrong calibration of the AGASA array. About this point and about recent developments in the AGASA-HiRes controversy we invite the reader to look the spectrum in Fig. 1.12 and [71].

Another really important but still debated Auger result is the clustering of UHECR events in correspondence with AGN [78] [79]. A correlation between the position of AGNs and UHECRs events seems to have been detected. The

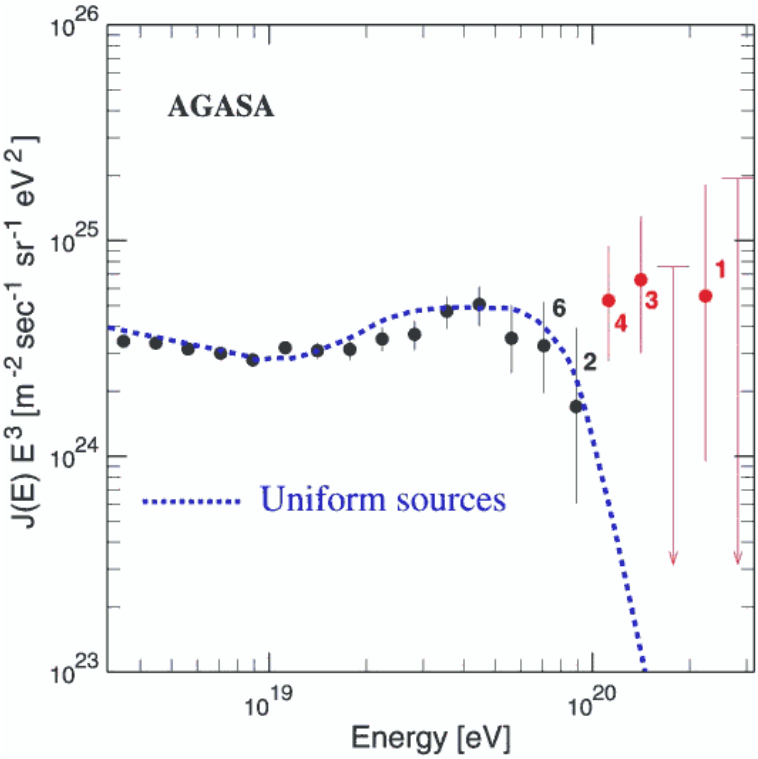

Figure 1.10: AGASA (red dots) and HiRes (black dots) [84] [85].

Auger collaboration claims that this correlation is statistically significant at 99%. It might well be that with Auger we are opening the era of particle astronomy observing sources of UHECRs.

However Auger tells also that in order to identify the sources and more important to measure their spectrum much more statistics is needed. For this reason to monitor a bigger atmosphere sample the next step would be a detector in the space since ground detectors have reached their maximum extension limit.

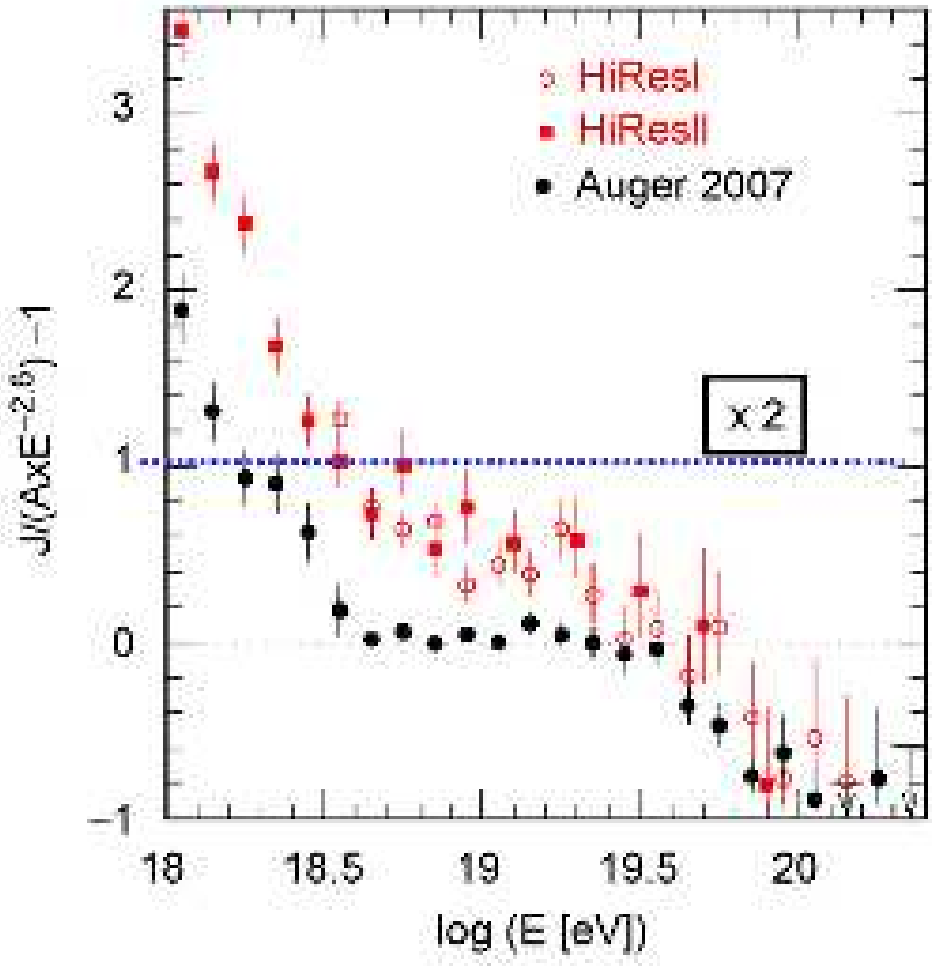

Figure 1.11: Cosmic rays spectrum obtained with Auger compared with HiRes spectrum using a reference spectrum $AE^{-2.6}$. Picture taken from [71].

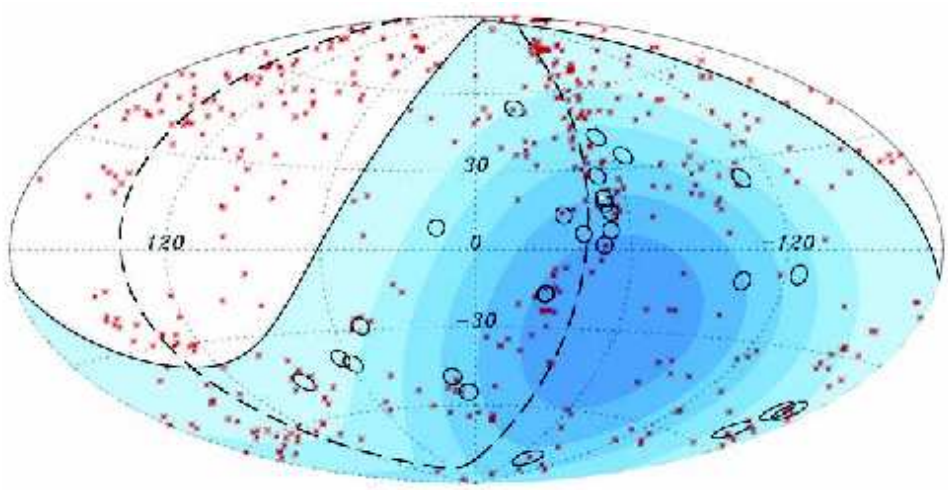

Figure 1.12: Auger sky map in galactic coordinates. With different colors is represented the relative exposure. The darker the area corresponds to the greater the exposure. The solid line indicates the limit of the field of view. Circles are representing the 27 highest energy UHECR events detected by Auger. Red points are AGN taken from the 12th edition of catalog of AGN. Picture taken from [78].

Chapter 2

Phenomenology and measurements of Extended Air Showers

In this chapter we will focus our attention on the phenomenology of Extensive Air Showers and on the way we could measure energy, direction and mass of the primary particle.

When a high energy particle enters the atmosphere it can collide with the atoms of the atmosphere. After the first encounter a cascade starts.

The particle will generate secondaries which will further generate other particles. Seen from an external observer the shower will look like a cloud of particles flying through the atmosphere producing florescence and Cerenkov light. Therefore the shower can be seen by a distant observer like a luminous "bubble" moving trough the atmosphere at the speed of light.

2.1 Electromagnetic shower

If the primary particle is a γ photon the leading physical processes are Bremsstrahlung and pair production. We see in pictures 2.3 the two scattering processes.

The so called Bremsstrahlung is emission of photons related to the acceleration of charged particles in nuclear electric fields. This process is dominant for charged particles at high energies. At lower energy other processes like ionization and collisional losses will prevail.

Pair Production is the process of an electron-positron pair production in proximity of a nucleus by an high energy photon. The photon energy has to be greater than the sum of the rest energy of an electron and a positron. At

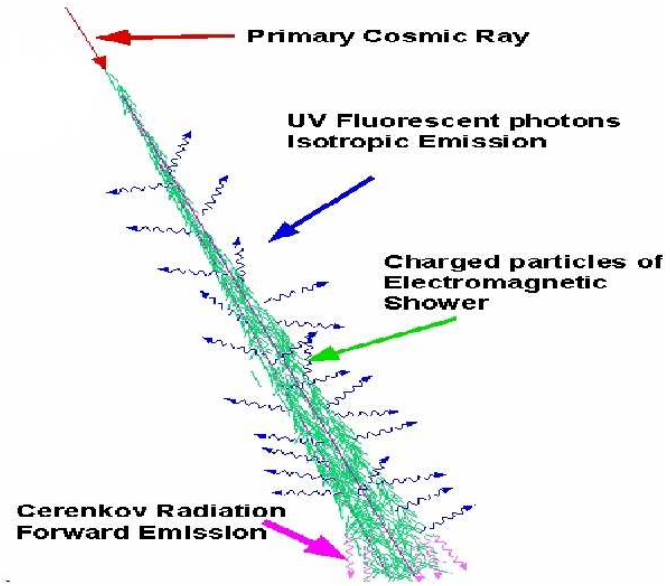

Figure 2.1: Light emission in an EAS. Picture taken from [96].

lower energy other processes like Compton scattering start to be competitive with pair production.

These process will generate the cascade. After n steps the number of particles is (in a first and very simplifying approximation) equal to $N_p = 2^n$ (see Fig. 2.2 and [80]). That's assuming that in each step the number of particles will double. This is of course a strong approximation that neglects at first every energy loss and assumes that the processes of Bremsstrahlung and Pair Production will be the only occurring. This is not the case but nevertheless this very simple model will give an explanation to many features of the electromagnetic shower development.

The processes of multiplication will decline as the ionization losses and Compton scattering start to have an efficiency comparable to that of brehms-strahlung and Pair Production. In a simplified model this threshold is reached very fast and the process of multiplication will stop suddenly. This is the point where the shower maximum is reached. Let's call the energy at which the process stops critical energy (E_c). This is by definition the energy at which the collisional and ionization energy losses for the electrons equal the radiational losses like Bremsstrahlung. In addition to that in this energy range photons begin to loose energy more through Compton scattering than

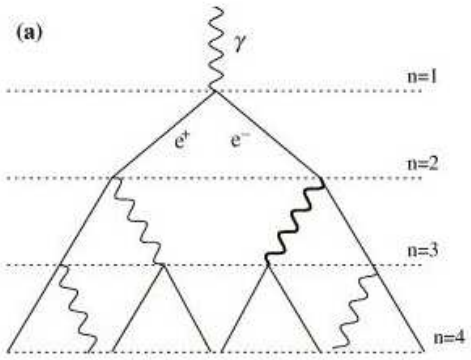

Figure 2.2: Base principle of an EM shower. Picture taken from [80].

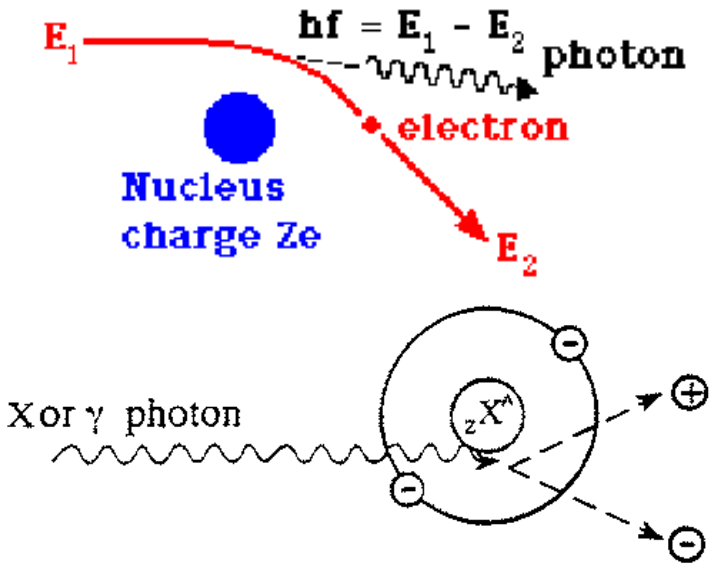

Figure 2.3: Schematic view of Bremsstrahlung process. Picture taken from [43]. Schematic view of pair production process. Picture taken from [44].

through Pair Production. This energy will be in air and for electrons more or less 85MeV.

In conclusion we can extract two basic features of EM showers. The first

is the dependency of the integrated signal from the primary energy. In fact:

$$N_{max} = N_c = \frac{E_0}{E_c} \tag{2.1}$$

Where N_{max} is the maximum number of particles, N_c the number of particles at the critical energy ((E_c)) and E_0 the primary energy.

The second is the dependency of the depth at the maximum from the primary energy. We know that it is also true $N_{max} = 2^n$. It follows:

$$n = \frac{ln(N_{max})}{ln(2)} = \frac{ln(\frac{E_0}{E_c})}{ln(2)} \tag{2.2}$$

And therefore:

$$X_{max} = \tau_{int} n \sim \ln(E_0) \tag{2.3}$$

Whereas τ_{int} is the average lenght a particle will traverse before interacting. That's one of the more important features to calculate the energy of a shower either electromagnetic or (with some adaptations) of any other kind.

This approximation however won't reproduce all the features of the shower. For example the model implies that $\frac{2}{3}$ of the particles are electrons and $\frac{1}{3}$ are photons. This is true at any point of the shower development. This is not the case. In fact photons are overnumbering the electrons. That's because of the multiple photons production that occurs really often and of the losses of electrons in the air.

That's however not the whole story. In fact such highly energetic photons are able to undergo hadronic interaction. That's because their energy is many orders of magnitude higher than the binding energy of the nucleons and therefore they can interact with nucleons. As consequence also a muonic component will be visible in the electromagnetic shower (see next section). To estimate the fraction of this muonic component is critical for ground particle arrays (where also muons can be detected) different is the case for space based observatories.

2.2 Proton shower

The basic difference between an EM shower and the one generated by a hadron is in the kind of interaction that comes into play. Essentially in the case of a hadronic shower in the first interaction $\pi^0, \pi^\pm$ and other hadrons are produced. The hadrons and $\pi^\pm$ will further undergo other hadronic interactions repeating (at a lower energy) the first step. The $\pi^\pm$ however will be able of making other hadronic interactions just at high energies. The

reason is that for relativistic time dilation effects at high energies for an observer in laboratory frame the lifetime of a $\pi^{\pm}$ will be much longer. As consequence those particles will most probably interact before decaying. As the energy gets lower charged pions decay:

$$\pi^{+} \rightarrow \mu^{+} + \nu_{\mu} \tag{2.4}$$

$$\pi^{-} \rightarrow \mu^{-} + \overline{\nu_{\mu}} \tag{2.5}$$

Muons and neutrinos will be produced by this decay. As this point is reached, the hadronic cascade decline and the remaining part is just electromagnetic (see Fig. 2.4). This is because a charged pion interacting will generate many other pions. If pions are able to interact with hadrons the hadronic cascade will therefore grow in size. On the contrary if pions can decay they will produce neutrinos and muons that have low cross sections. The hadronic part of the shower will therefore decline.

The π^{0} decay immediately because their lifetime is really small (8.3×10^{-17} s).

$$\pi^{0} \rightarrow 2\gamma \tag{2.6}$$

Through this channel the electromagnetic part of the shower will be generated. It is important to stress that the EM fraction is the part of the shower producing fluorescence light (see section 2.5) . In fact a lot of electron are produced here while the muons produced in the $\pi^{\pm}$ decay will have a very low cross section and will reach the earth. All of those points can be seen in plots 2.4.

In the approximation of [80] the electromagnetic fraction of the hadronic shower can be calculated to be more than 90% . That means that through the π^{0} decay channel 90% of the primary energy will go to the EM component. Therefore a proton originated shower will result to be more or less 10% less luminous than a photon shower having the same energy.

Which is the depth of the maximum of the hadronic shower? The crucial point here is the energy of the photons generated in the π^{0} decay. Starting from primaries of the same energy the photons in the hadronic shower (from π^{0} decay) will have a lower energy than the primary γ photon itself. That's because of the fact that the single subproducts of a hadronic interaction are each one sharing just a fraction of the primary energy. Using equation 2.2 and 2.3 we can therefore see how the maximum will be reached faster than in the case of a photon generated shower. That's true even if more generations of π^{0} are available. In fact those new generations are originated more forward

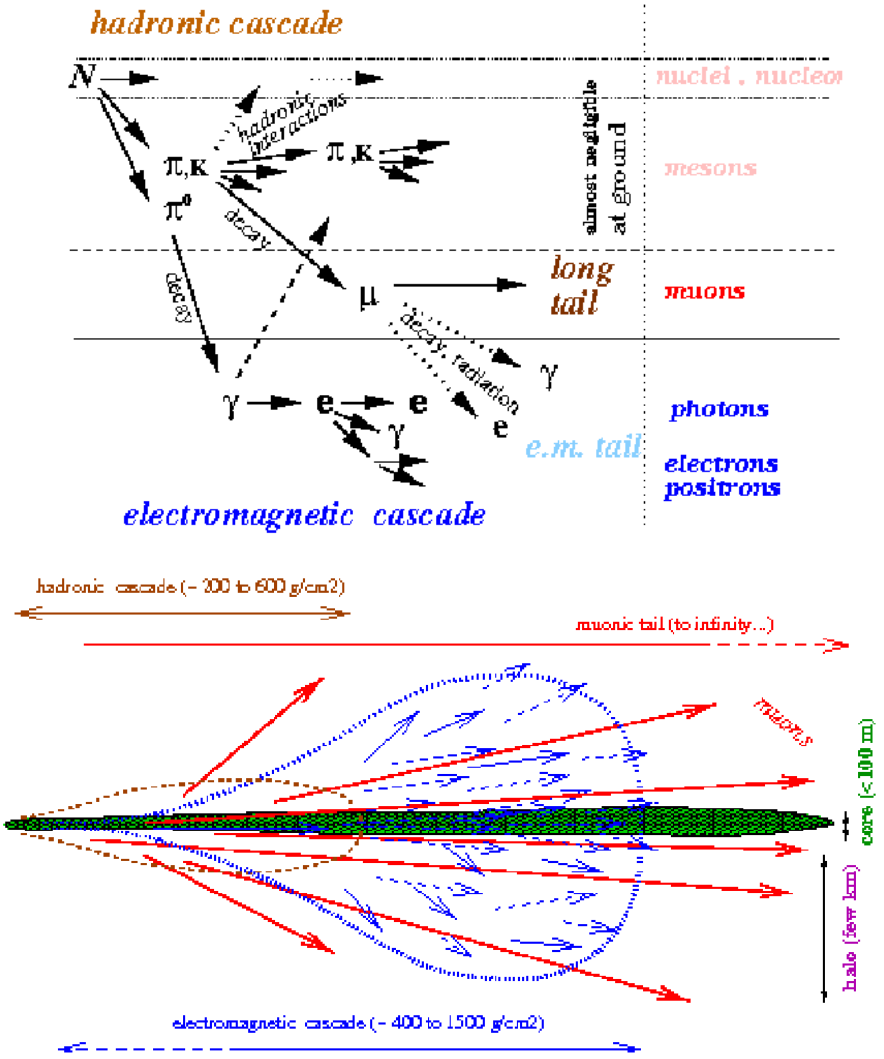

Figure 2.4: Base principle and structure of of an Hadronic shower. Picture taken from [97].

in the shower development and therefore one could expect a longer shower. However the overall contribution of all those subgenerations won't make the shower longer than in the case of a photon generated shower.

These features but particularly the second one (the differences in maximum depth) will be a very useful tools in order to try to distinguish between primary type in a space based observatory.

Worth to be mentioned is another feature: the content of muons $\mu^{\pm}$

detected in a particle detector array on the ground. The photon generated shower will also generate a muonic component. This is because of the hadronic interaction properties of the photon. The hadronic shower however will generate a much stronger muon component than in the electromagnetic case. That's because of the $\pi^{\pm}$ decay. This is the reason of the very different footprints of the two kind of showers when observed from the ground with particle detectors. We will see that for a shower originated by a nucleus this effect is even stronger.

2.3 Nucleus shower

Showers originated by nuclear primaries are, like those generated by protons, driven by hadronic force. There is however a difference.

We analyze these differences by assuming some simplification. For example we can consider the nucleons in the nucleus like non interacting one with the other. In this approximation they can be considered as single particles interacting with air atoms independently from each other. The crucial point is the energy of the single nucleons. We can consider the single nucleon as an isolate incoming nucleon having an energy of $\frac{E_0}{N}$ whereas N is the atomic mass and E_0 is the primary energy of the nucleus. The depth of the maximum will be reached much faster than in the proton and photon case. This is because the energy of the single nucleon is lower and equation 2.3 says that there is a logarithmic dependency between depth and particle energy. The total luminosity won't be that different because the less luminosity for each single nucleon is compensated by the grater amount of nucleons.

We show in Fig. 2.5 and 2.6 the dependency of the depth of the maximum for the tree species we examined. And a comparison between three possible shower profiles (see figures 2.5 2.6).

Another thing we already mentioned is the strong muon component of this kind of showers. In fact being the single nucleons of smaller energy than the nucleus a smaller number of hadronic interactions is needed in order to reach the $\pi^{\pm}$ decay point. Considering that each step a 30% of the energy goes to the electromagnetic fraction the more steps we have the less energy will be kept by $\pi^{\pm}$ at the point where the hadronic cascade declines. Therefore in this kind of showers a bigger fraction of muons on ground is observed.

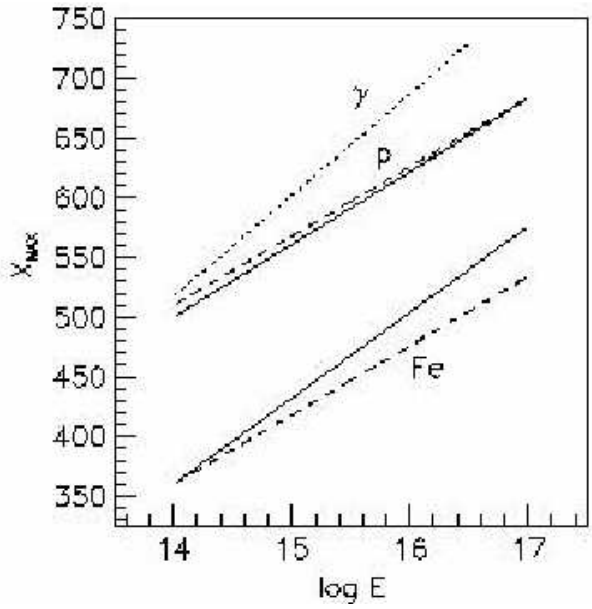

Figure 2.5: Dependency of the depth of the maximum for the tree species. Picture taken from [80].

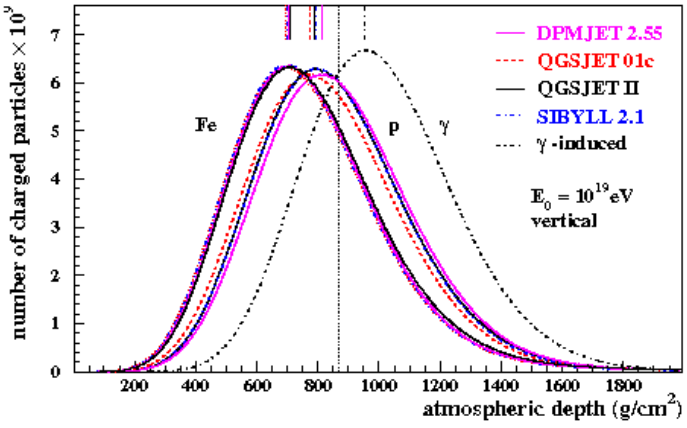

Figure 2.6: Simulated profile of different kinds of showers. Picture taken from [28].

Shower identification-Resume

Just to conclude this section we could summarize the main differences between the three types of shower we talked about before. This

is in order to resume what kind of observable we could use to distinguish the different kind of primaries. We said that starting from the same primary energy in a photon shower the maximum is reached at a much higher depth than in the case of proton. Nucleus showers are even shorter than proton showers. There are however many other differences like for example the muon fraction on the ground. This will be another important tool to calculate the mass of the primary. Obviously this is a tool usable just on ground.

2.4 Neutrino shower

2.4.1 UHE-Neutrino Cross Section

Another point we should stress in dealing with neutrino induced showers is the fact that the cross section of those particles is not more negligible as in the case of solar or supernova neutrinos. The reader could think to neutrinos like those extremely penetrating particles able of traversing a mass like the sun almost without being attenuated. In this case the atmosphere would not be sufficiently massive to make possible any neutrino interaction. However for extreme energies the story is different. In fact the cross section is increasing with the energy as can be seen in plot 2.7. In our range of energies the Cross Section is 8 or 9 orders of magnitude higher than in the case of solar neutrinos which have energies of 10^7 eV.

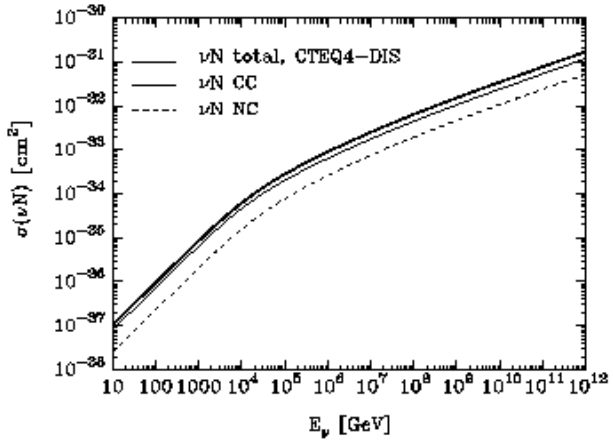

Figure 2.7: Neutrino cross section. Picture taken from [98].

2.4.2 UHE-Neutrino shower phenomenology

The processes involved in the interaction between the neutrinos and nucleus are of two kind: neutral current and charged current.

$$\nu + N \rightarrow \nu + Hadrons(NC) \tag{2.7}$$

$$\nu + N \rightarrow leptons + Hadrons(CC) \tag{2.8}$$

In the first case the reaction itself won't generate a shower distinguishable from hadronic one. In the second case we will observe a mixed shower partially hadronic and partially electromagnetic. Also here the nature of this reaction is not enough to distinguish with reliability from another kind of primary.

We therefore have to look for other properties in order to distinguish neutrino induced showers from hadron generated showers. The first difference is in the lower (but not negligible, as we saw) cross section compared to protons. This will cause a deeper penetration of neutrinos in the atmosphere. The distribution of depth of first interaction (but also depth of maximum) is therefore proportional just to the density of the atmosphere since the neutrinos flux won't be attenuated a lot by the atmosphere. On the contrary in the case of protons the first interaction will be most probably at the top of atmosphere and therefore the depth of the maximum will be dependent from the inclination angle. The more the shower is inclined the higher will be the height of the maximum. This is simply because the flux of protons will be strongly attenuated by the atmosphere. The first interaction will be at the top of the atmosphere and the maximum will be deep for a vertical shower and very high for a horizontal one.

As can be seen in Fig. 2.8 left panel for neutrino showers the altitude of the maximum will be smaller than in the case of showers with proton primary. We can express the differences in the development with other variables: the slant depth of the maximum [1] (see Fig. 2.9). On the right panel we see the shower developments as function of the slant depth.

Of course the problem is to measure the altitude of the maximum. This can be done when the signal from the diffusively reflected Cerenkov light at impact point is measured. This timing information can help us to discriminate between a neutrino shower and a proton one. In fact, neutrinos can develop deeper. Then neutrino showers will also be much nearer to the earth surface

[1] This is the integral of the density of matter traversed calculated along the trajectory of flight.

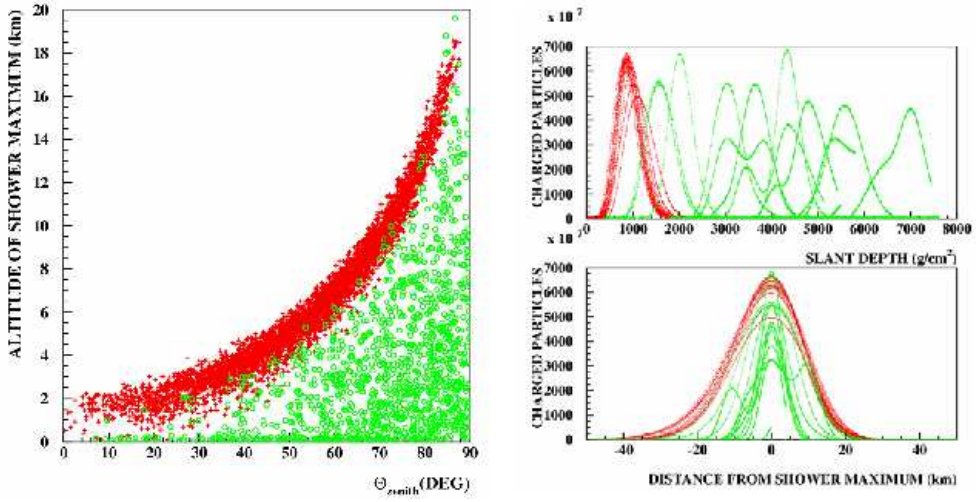

Figure 2.8: Altitude of shower maxima and longitudinal profile of shower (green dots are neutrinos, red are protons). Picture taken from [90].

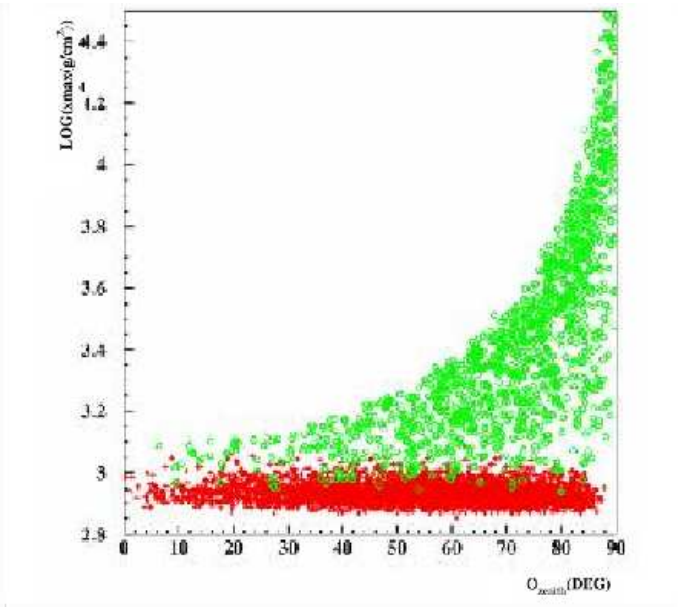

Figure 2.9: Slant depth of shower maxima (green dots are neutrinos, red are protons). Picture taken from [90].

and the time difference between fluorescence maximum and Cerenkov peak will be shorter.

For very inclined showers however the Cerenkov signal won't be visible.

For those cases we have to look for another method. The fact that neutrinos have the power to penetrate much in depth brings the shower to very low altitude and in dense layers of the atmosphere even for very inclined particles. Therefore the evolution of neutrino showers will be on average much faster than the case of proton showers. The time duration of the shower could be used to discriminate between different primaries (look Fig.2.10).

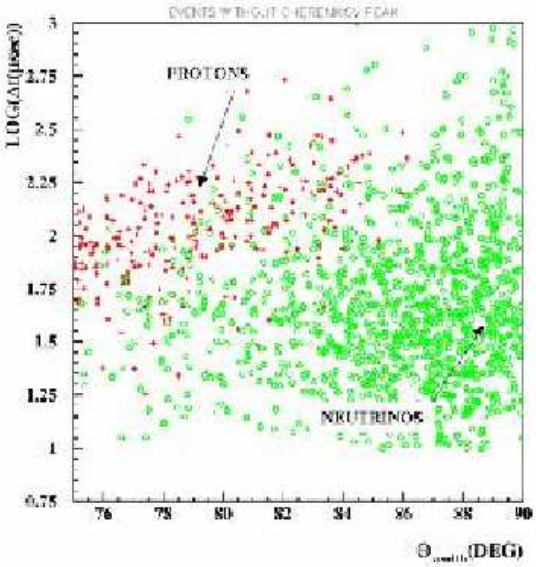

Figure 2.10: Time-angle dependency for very inclined showers (green dots are neutrinos, red are protons). Picture taken from [90].

2.5 Detection techniques

Different detection techniques can be used to detect cosmic rays from low energy up to EECR.

The basic concept concerning the detection of low energy Cosmic Rays (under 10^{15} eV) is that in order to make possible the particle detection we have to reduce as much as possible the amount of atmosphere above the detector. In fact the atmosphere acts as a giant absorber making impossible the detection on the ground. Therefore we have two possibilities: to fly the detector on a balloon or even on a space satellite. There are many types of detectors but essentially we can divide them in two categories.

First we find the so called magnetic detectors. In this particular kind of detectors a magnetic field is used in order to determine the ratio between

charge and mass measuring the deflection of the particle by the field. The combination with another detector gives than the possibility to measure the charge alone. An advantage of this kind of detectors is the very good measurement capability of the properties of the particles. A disadvantage is their very narrow energy range because of the different magnetic rigidity of the particles with different energy.

In the second category we find particle calorimeters. This kind of detectors are made of layers of target material and particle detectors. Essentially in the target a secondary cascade is generated. In the particle detector (or calorimeter) the energy of the cascade is measured. This layout can be combined with other layers in order to know other properties of the primary. The advantage of these detectors is that they have good sensitivity for all the masses. A disadvantage is their high weight. For more detail the reader is invited to look at [29].

For energies above 10^{15} eV we need a much greater detector volume. The most suitable target in this range is therefore the atmosphere. As explained before a very high energy CR will generate a cascade of particles. Either the secondaries (like e^+, e^-, μ^+, μ^-...) reaching the ground or the light produced by the cascade can be detected.

We have respectively ground particle array detectors or fluorescence light detectors [2]. In the first group we find detectors like AGASA [22] [23], KASCADE and KASCADE Grande [81], Volcano Ranch [10] and many others. In the second group HiRes [17], Fly's eye [15] and the EUSO family itself. The PAO is the only array up to now combining both techniques.

In the Volcano Ranch array there was the first detection of a CR above 10^{20} eV. We already talked about it in the historical introduction. This detector was an array of plastic scintillation detectors in New Mexico desert. This consisted of 19 scintillation counters having a surface of 3.3 m^2 deployed on an hexagonal grid having side of 884 m.

In Fig. 2.11 we show an aerial view of another ground particle detector: AGASA.

In the AGASA array 111 surface *particle detectors* were present. Each of them consists of a 2.2 m^2 area plastic scintillator. Furthermore there are other 27 muon detectors divided in several categories according to the size. One detector has 20 m^2 surface, one 15 m^2, six 10 m^2 each, one of 7.2 m^2, three 3.6 m^2 and fifteen of 2.8 m^2 each. In Fig. 2.12 and 2.13 the detectors are shown. They are all particle scintillators. We invite the reader to look in [22] for more detailed information.

[2] Also the Cerenkov beam can be used to detect UHE particles. For example TeV gamma rays are in part detected with Cerenkov Array Telescopes like Magic or HESS.

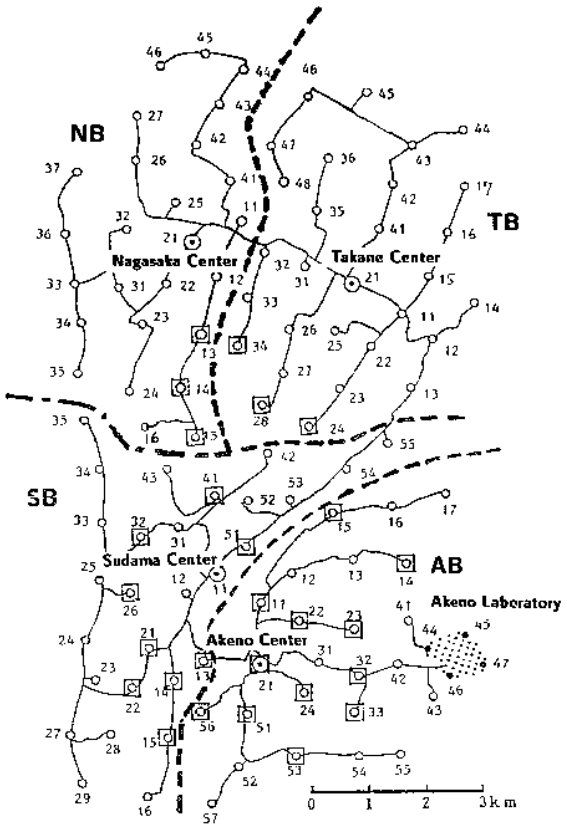

Figure 2.11: Aerial view of the AGASA array. Picture taken from [22].

Also to be mentioned is the Haverah Park array [13]. This was an array of water Cerenkov detectors operating in England from 1967 to 1987. The Cerenkov detectors were galvanized steel tanks, 1.85 m x 1.24 m x 1.29 m high, filled to a depth of 120 cm with water. Those detectors are described in [13]. We show here a picture of the detector (see Fig. 2.14).

In the other family of instruments we find the fluorescence detectors. As we said in the historical introduction the first attempt to detect cosmic ray showers with *fluorescence detectors* has been done at Cornell University in 1967. We invite the reader to go to [87] in order to have a better explanation.

Another really important detector was the Fly's Eye [16]. This array consisted in two station of mirrors 3.3 km apart. The positioning of the 67 telescopes having the diameter of 1.5m was made to have a full coverage of the sky. We can see in Fig. 2.15 an aerial view of one station and a detailed view of one telescope. Those detectors were reflective telescopes focusing the light on photomultipliers. The mirrors are spherical, front aluminized and

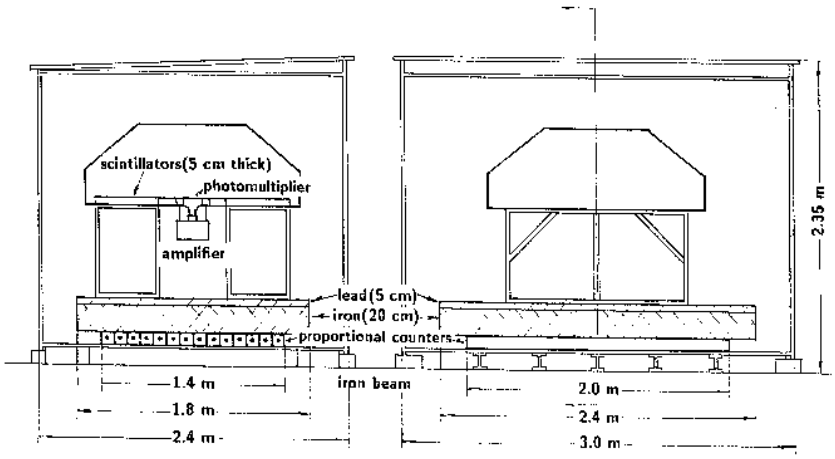

Figure 2.12: AGASA. On the left: a 2.2 m^2 surface detector. On the right 2.8 m^2 μ detector. Figure taken from [22].

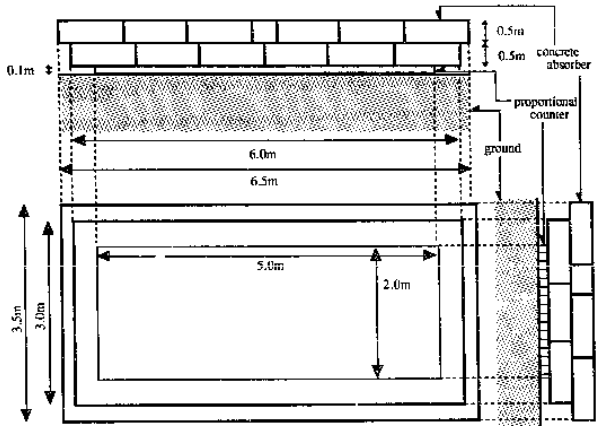

Figure 2.13: AGASA. A 10 m^2 μ detector. Figure taken from [22].

each one of them focused the light on hexagonally packed groups of 12 or 14 light sensing eyes (photomultipliers). The total number of sensing eyes was 880 at Fly's Eye 1 and 460 in Fly's Eye 2. Each photomultiplier was able to cover an hexagonal portion of the sky having dimension of 5 deg. A shutter was available to close the aperture of the telescopes in order to protect them from light and bad weather.

On the same site of Fly's Eye the so called HiRes or High Resolution Fly's Eye array has been constructed. The array started its activity in 1999 and

Figure 2.14: Haverah Park water Cerenkov detector [14].

it consists of two stations separated by 13 km. We invite the reader to check in [17] for more detailed information. Two stations are made respectively of 22 and 42 telescopes each one having 2 m diameter. At the focal plane of each instrument there is a cluster of 256 photomultipliers each one of them covering 1 deg of sky. We show in Fig. 2.16 the structure of one mirror.

We will talk now also of the *hybrid approach*. This is the basic idea of Pierre Auger Observatory [24] [26]. The combination of an array of 1600 water Cerenkov detectors and 4 fluorescence observatories should make the calibration of both techniques possible. PAO consists currently of one site in the southern hemisphere. A second site in the northern hemisphere is planned to be build. The southern is located at Malargüe (Argentina) and it has an extension of 3000 km^2. The northern site will have an extension of 21000 km^2 and will be located in Colorado. The water Cerenkov detectors are located for the southern array on an hexagonal grid and are 1.5 km one from the other. The geometry for the northern site is not decided yet. The water Cerenkov detectors will have a surface area equal to 10 m^2. Four fluorescence detectors each one consisting of 6 telescopes with 1.7 m pupil diameter giving an effective area for light collection of 1.5 m^2 (after taking account the obstruction of the camera) complete the observatory. The radius of the mirror is 3.4 m and the angular size of the spot is 0.5 degree (or $\frac{1}{3}$ of the pixel size). The telescopes are Schmidt cameras. To improve the ratio of the signal to the noise, a UV transmitting filter is placed on the diaphragm. Because of the symmetry of the optical system, the actual focal surface is

Figure 2.15: Aerial view of the Fly's Eye station. Detail of a telescope. Pictures taken from [16].

spherical in shape. It is concentric with the mirror and has a radius of 1743 mm. The camera is an array of 440 hexagonal pixels arranged in such a way to adapt to this spherical surface. The pixels are not regular hexagons, and their shape and size vary slightly over the focal surface. Each Cerenkov detector consists of a polyethylene tank, 3.6 m diameter and 1.55 m high filled with 12000 liters of high purity water. On the top of the tank there are 3 photomultipliers. Signals from the photomultipliers are read by the electronics.

The duty cycle of the water Cerenkov detectors is 100% while for the fluorescence telescopes is 10%. We give in Fig. 2.20 an overview of the water Cerenkov detector and of the fluorescence detector of AUGER.

2.5.1 Fluorescence and Cerenkov emission

We conclude the chapter with some word on the mechanisms that produce the fluorescence light [87]. Here the encounter between the high energy particles

Figure 2.16: HiRes mirror. Picture taken from Auger website.

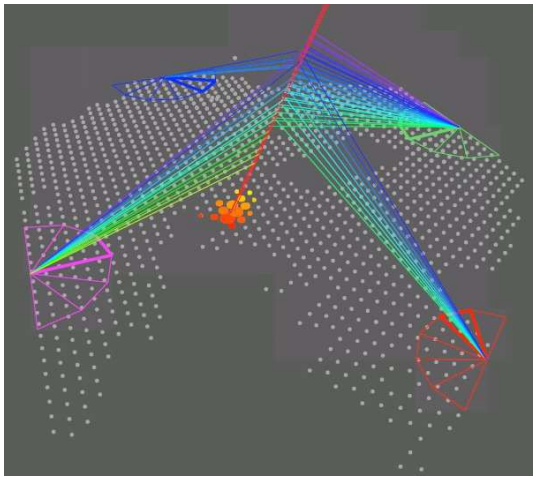

Figure 2.17: Scheme of Auger principle [86]

and air's atoms causes the ionization of the latter and the production of low energy electrons. There are two processes involved in the production of fluorescence light. The first one is a direct one and is caused by the ionization of a molecule of N_2. The molecule is left in an excited and ionized state and

Figure 2.18: View of fluorescence observatory (back) and particle detector (front) in Auger detector [86]

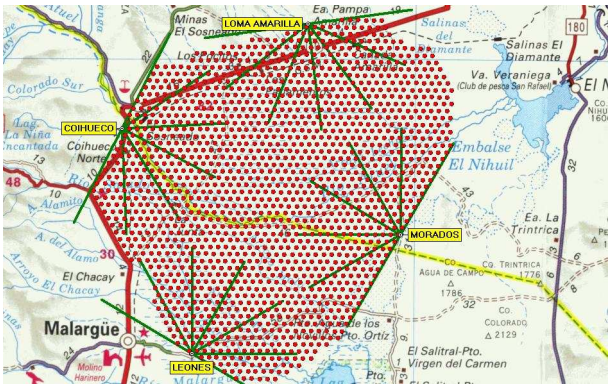

Figure 2.19: Auger-south array map.

the successive decay of it will cause the emission of UV photons. This kind of process gives rise to the first negative band excited state decay. The second process is a two step process and is caused by the excitation of the neutral N_2 after the encounter with secondary electrons generated in the ionization of other N_2 molecules. The two processes are 1N and 2P. We summarize them in Fig. 2.21.

Photons in the range of some tenth of eV (near UV) will be produced. The emission will be discrete: a lot of lines will be observable for both of those processes. The typical decay time for radiative decay is of the order of tenth of nanoseconds.

The efficiency of light production is dependent also from atmospheric conditions. That's because of the other processes concurring with the radiational deexcitation. An excited molecule can emit its energy by mean of a

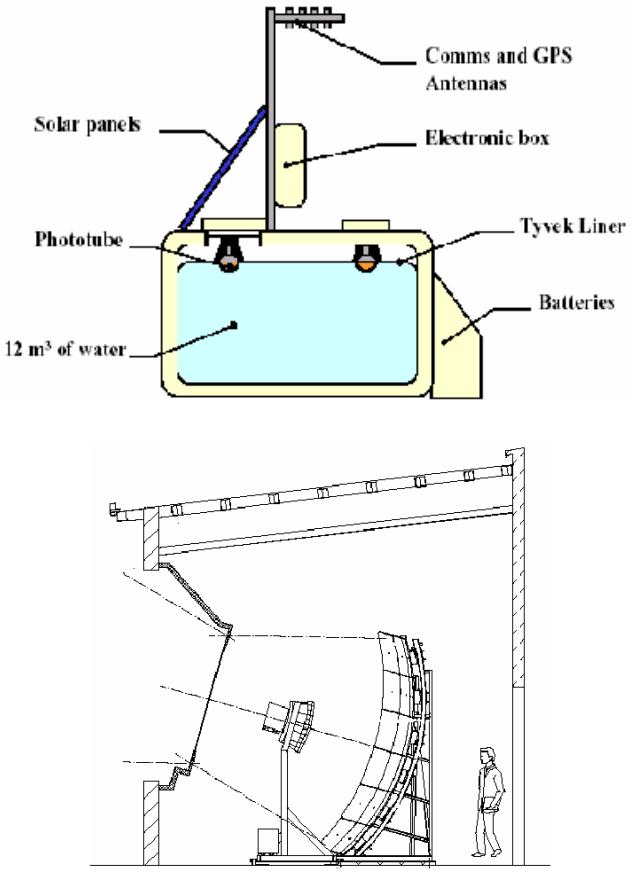

Figure 2.20: Scheme of a water Cerenkov tank of Auger and a fluorescence telescope. Picture taken from [25]

radiative decay or by quenching. There are two types of quenching: internal or collisional quenching. The internal quenching is a process depending on the temperature $k_i \sim e^{\frac{-E}{KT}}$ and it consists in an intermediate and multiple decay process. The mean decay time of this process is therefore $\tau_i = \frac{1}{k_i}$. This process will produce photons but at a much higher wavelenght and therefore outside of the observational window.

The collisional quenching is a process of energy loss due to the collision between the excited molecule and other molecules. This will not involve any radiation emission but there will be an exchange just of kinetic energy. The mean decay time is $\tau_c = \frac{1}{nk_c}$ whereas nk_c is $nk_c = n\sigma vsec^{-1}$. V is the velocity and is equal to $(\frac{8kT}{\pi M})^{\frac{1}{2}}$, σ is the cross section and n the density. We see immediately that the higher the temperature is the shorter the typical

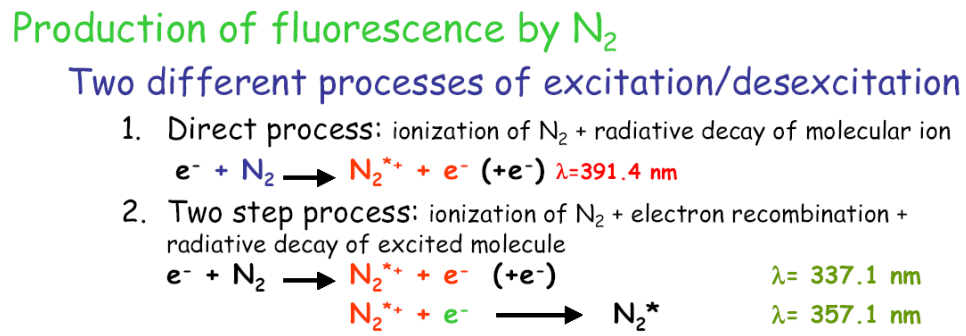

Figure 2.21: Schematization of the Fluorescence process. Courtesy of C. Berat et al., 2002 and D. Lebrun, 2002.

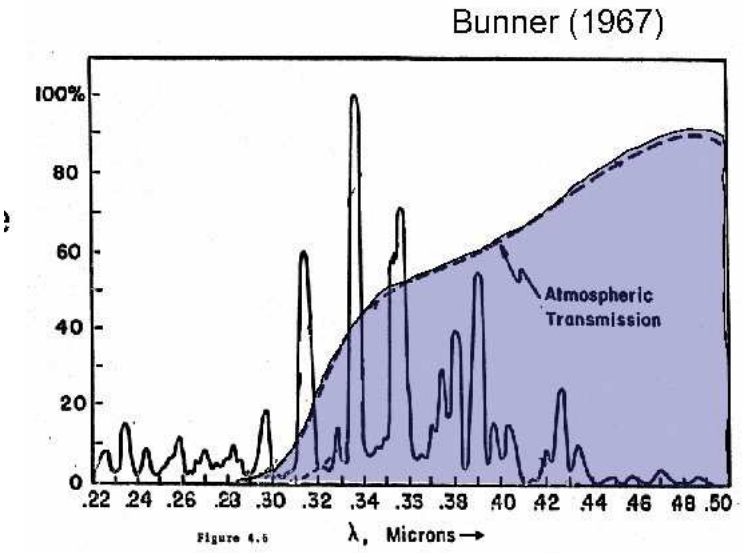

Figure 2.22: Fluorescence emission lines. Fig. taken from [87].

decay time is. Another factor that influences the collisional quenching is the density. For a high density we will have a smaller decay time. This is true because of the higher probability that a molecule has to scatter against other molecules when the temperature and the density are high.

Those two processes are of primary importance because of the fact that the stronger they are the less excited atoms are available for the radiative

decay. However to calculate the so called fluorescence yield [3] is a complicated task and it depends by a lot more factors. We saw the density and temperature. However also the charged particle energy is an important factor. The 1N transition process cross section is not strongly energy dependent. It remains more or less constant over many energy decades [18]. The cross section is however strongly energy dependent for the 2P process [19]. This will be affected from the energy of the secondary electron.

Yield calculations are done usually in N_2. In the real atmosphere there is however also Oxygen which will affect very strongly the 2P process. In fact being Oxygen a really electronegative atom will capture the low energy secondary electrons.

Humidity is a second important factor. The hydrogen present in water will capture the electron and a H^- will be formed.

We see in the end how a detailed calculation of the yield is a really difficult task that depends on many atmospheric parameters. There are different modellizations. We present in Fig. 2.23 a calculated fluorescence yield plot from [20] that shows how the yield of an electron is in a first approximation equal to 4 photons per meter per electron.

That would justify at least the assumption of the shower light intensity being proportional to the number of charged particles.

To conclude let's spend some word on the Cerenkov emission. Cerenkov is a process that occurs when a relativistic particle enters a material with a superluminal velocity. This will cause the formation of a shock wave as illustrated and the production of light concentrated in a cone. The Cerenkov power dissipated by an electron per unit lenght will be equal to:

$$\frac{dW}{dx} = \frac{e^2}{c^2}\int (1 - \frac{1}{\beta^2 Re\epsilon(\omega)})\omega d\omega \tag{2.9}$$

Whereas e is the electron charge, β the Lorentz factor of the electron, ϵ the dielectric constant and ω the photon pulsation. We invite the reader to check in [21] for more detailed calculations.

[3] How many photons are produced by a charged particle traversing the atmosphere per unit lenght.

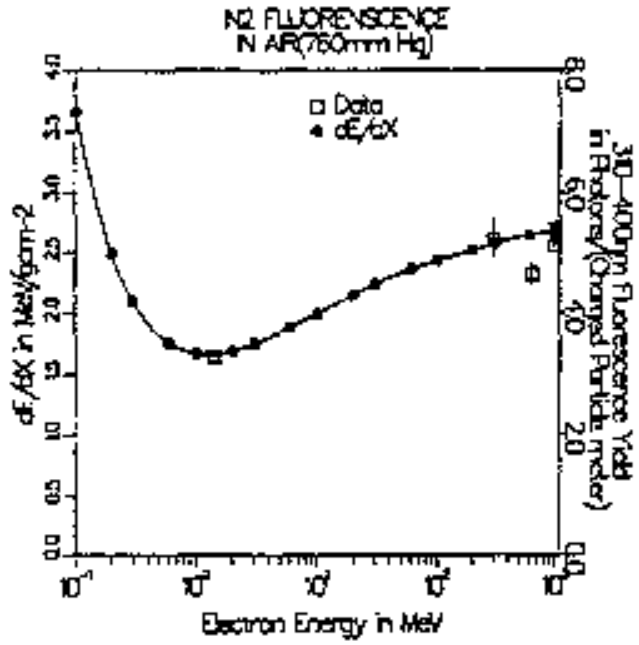

Figure 2.23: Fluorescence yield ad function of energy. Picture taken from [20].

2.5.2 Atmospheric scattering-absorption

Interaction between light and atmosphere is critical for the detection of UHECR from space. This will happen by mean of two processes: absorption and scattering. In the first process we intended mainly the ozone absorption. This process will make the detection of photons with wavelenght under 320 nm impossible. The second one is the scattering. This will be the principal disturbance phenomenon in our observational window.

There are essentially two types of atmospheric scattering: the one of Rayleigh and the one of Mie. The first one is the scattering with the air molecules. The cross section of this process is:

$$\frac{d\sigma}{d\Omega} \propto \frac{1}{\lambda^4} \tag{2.10}$$

Whereas the Ω is the solid angle and λ the wavelenght of the photon.

The other one is the Mie scattering. This is the scattering of light with a spherical or cylindrical object. In this wavelengh range the droplets and grains in suspension in the atmosphere are suitable targets for photons in the UV range. This is a much more complicated task and its cross section depends on many different factors. We cite some of them: grains dimension

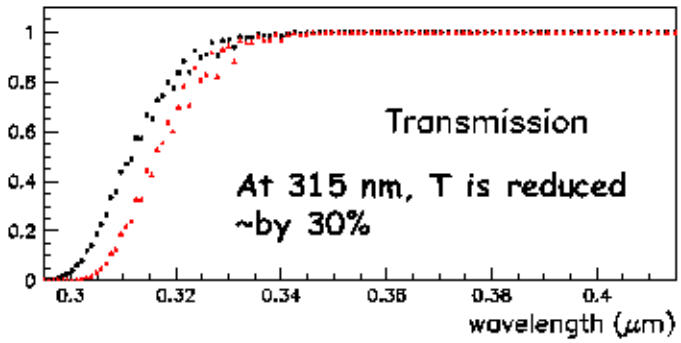

Figure 2.24: Transmission coefficient as function of the emission altitude as would be measured from a space observer. Ozone absorption. Picture taken from [90].

and dielectric constant of the material they are made of. Furthermore dust and aerosols are not uniformly distributed. Altitude, geographic position, pollution and many other factors will influence the presence of those pollutants in the atmosphere.

In the end we can see in Fig. 2.25 a summary of the effects of all the scattering processes involved in the atmosphere.

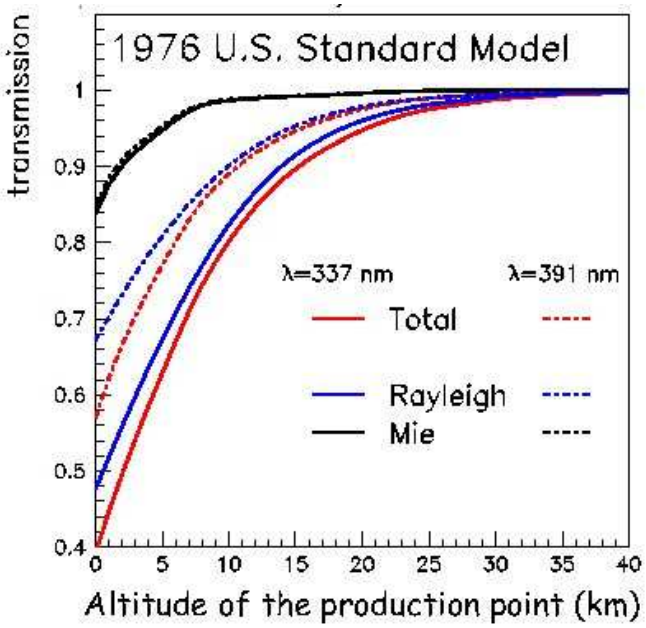

Figure 2.25: Transmission coefficient as function of the emission altitude as would be measured from a space observer. Just scatterings. Picture taken from [90].

All the curves in Fig. 2.25 have been calculated with LOWTRAN7 a computer code which predicts the atmospheric transmittance and thermal radiation emitted by the atmosphere and the Earth.

Chapter 3

Space observation of Ultra High Energy Cosmic Rays

3.1 Introduction

The reason for developing a space based fluorescence detector for the observation of cosmic rays is to increase the statistics at higher energies. Above $5 * 10^{19}$ eV the flux of CRs is of the order of one particle per km^2 per century or, accordingly to the recent measurement by Auger South, even less than that [71]. In order to get a number of events that allows us to identify the sources and their spectrum, we have to monitor a sample of atmosphere as large as possible. From the ISS (at 400 km), with a field of view of $\pm$ 30 degrees, 5 million km^3 of air can be monitored. The geometrical acceptance translates to, in the case of JEM-EUSO, $6 * 10^5$ km^2 sr. For comparison Auger observatory will have a total acceptance of the order of 14000 km^2 sr [88]. S-EUSO, flying at a height of 800 km will reach an aperture of the order of 1.3×10^6 km^2 sr [91]. These are geometrical apertures neither considering any cloud presence nor a duty cycle nor any dead time of the instrument. We give here the formula of the effective aperture taken from EUSO Red Book:

$$A^{eff} = \eta_o \eta_c (1 - \tau_{dead}) \pi^2 H^2 tan^2(\gamma_M) \tag{3.1}$$

whereas η_o is the duty cycle, η_c the cloud coverage efficiency, τ_{dead} is the dead time of the instrument, H the height and γ_M the half field of view angle. This formula is of course valid for space observatories. Such a huge calorimeter will make possible the UHECRs observation.

The detector has to work just at night and without moon. This will severely restrict the duty cycle by a factor of 10. Even at night, without moon, the background reduction is essential for space observatory of UHECRs.

The strongest background source is the so called "Night Airglow". This is due to the dissociation of the molecular oxygen in the sunlight of the day followed by recombination at the night [89]. When two atoms of oxygen recombine they emit UV photons in the observational window. We can quantify this source to be between 250 and 600 photons $/(m^2 * ns * sr)$ [89] [90]. A second background source is the reflection and scattering from starlights and planets. This has been quantified to be between 190 and 320 photons $/(m^2 * ns * sr)$ [90]. These background sources are a true challenge for EUSO-like missions, since we expect just at most some thousand of signal photons within 100 μs for each single shower. Fortunately, as we will see, the signal has a recognizable footprint that makes possible to recognize it in the background sea. However it appears clear that an efficient but selective trigger algorithm is critical for space based fluorescence detectors.

The original idea of detecting an extended air shower from space at night was proposed by J. Linsley in 1979 [95]. As we already explained, a high energy particle will enter the atmosphere and generate a cascade of particles. These particles traversing the atmosphere will produce fluorescence and Cerenkov light. The fluorescence light propagate isotropically and can be detected by an UV camera (sensitive to 300-400 nm) deployed on the ISS space station or on a free flyer. The base principle can be observed in Fig. 3.2. Different is the story for the Cerenkov light. This component will be emitted downward and therefore the direct Cerenkov component won't be detectable from space. There will be however two observable components: the reflected and the dispersed Cerenkov. The first one, generated when the EAS impacts on the ground or on a cloud, has a clearly distinguishable footprint and it adds information on the shower characteristics. The second one is light scattered on the air along the shower track. It will therefore be an amount of light present in the light profile. The profile should therefore be corrected by this component. In Fig. 3.1 we show the bell like time profile of the fluorescence signal and at the end the spike associated to the detection of the diffusively reflected component.

3.2 EUSO

The EUSO acronym stands for Extreme Universe Space Observatory. As we said the idea of detecting air showers from space has been proposed at the end of the seventies by J. Linsley [95]. However because of the technological complexity of such a space mission, no project was studied for more than a decade. In the middle of the 90s, thanks to Y. Takahashi and L. Scarsi, conceptual studies such as the OWL and AIRWATCH projects were carried

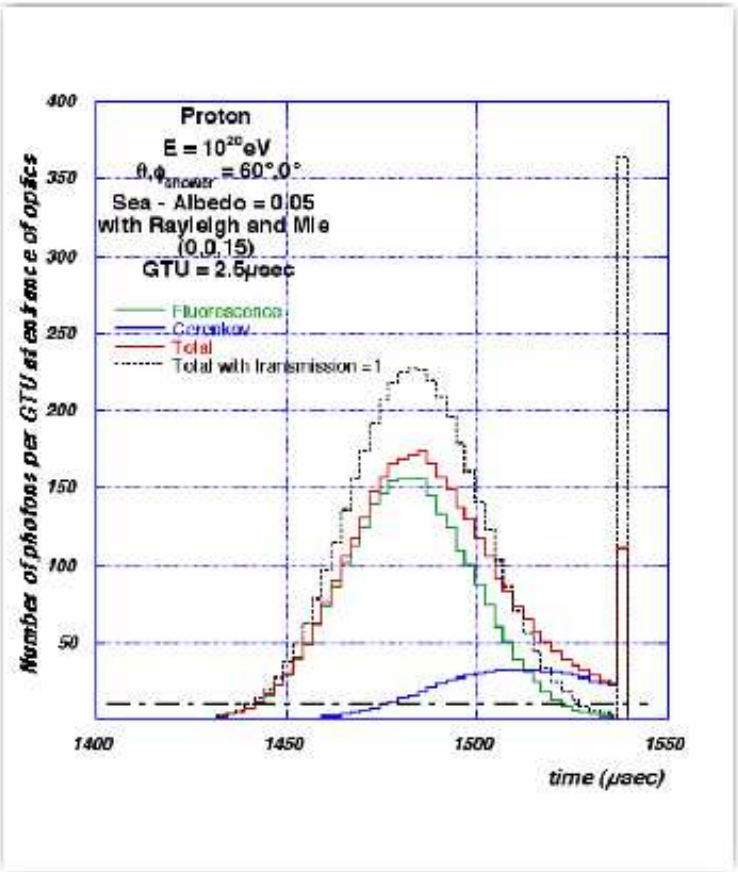

Figure 3.1: Time profile of an EAS viewed from space (photons at the entrance of the optics) [90].

out. In 2000 a proposal to the European Space Agency was submitted for a space based cosmic ray observatory called EUSO [94].

In 2002 a phase A study was committed, by ESA, to Alenia in order to find an accommodation on-board of the ISS for such a complex payload, planned to fly at the end of the decade. However, after changes in the ESA policies, especially after the Columbia disaster, the mission was put by ESA in a standby state.

The EUSO basic idea was to build a UV camera to be attached to the ISS (height 430 km) in order to observe the atmosphere from space. The relevant parameters of the mission are summarized in table 3.1.

In Fig. 3.3 and 3.4 the EUSO structure is shown. We can divide the entire instrument in two major blocks: optics and electronics.

Charachteristic	Value
Height	430 km
Latitude coverage	$\pm$ 51 deg
Orbital period	1.5 hours
Operational life	3 years + 2 extension
Instrument duty cycle	≤ 0.25
Optical band width	330-400 nm
Maximum diameter	2.5 m
Field of view	$\pm$ 30 deg
Focal lenght	$\leq$ 2.5 m
Focal surface radius	1.13 m
Optics structure	Double Fresnel lens
Optics material	PMMA
PMT	R8900M-03-M36
FS layout	X-Y or $\theta - \phi$
Geometric instantaneous aperture	$6.8 \times 10^5 km^2 sr$

Table 3.1: EUSO mission parameters [90].

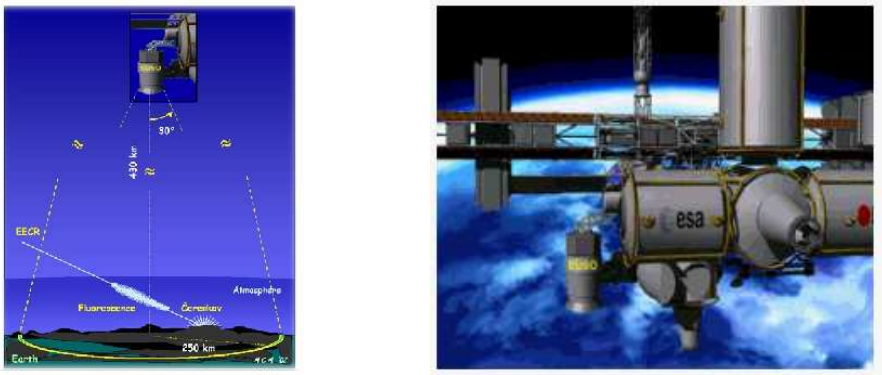

Figure 3.2: Euso principle [90] artistic impression of EUSO.

3.2.1 Optics

The instrument was a refractive camera made by a system of double Fresnel lenses which reproduce the profile of a normal lens.

Ideally we can obtain this structure by shaping a lens in many segments as shown in Fig. 3.5 and then collapsing them on a plane. Rays coming from a side will fall on this new surface with an inclination equal to what it would be in the case of the normal lens (see Fig. 3.6). Of course, this lens

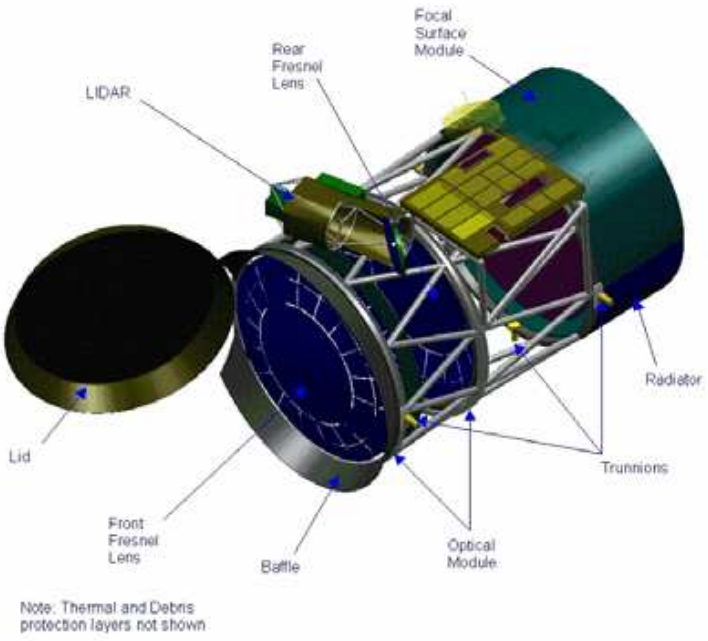

Figure 3.3: EUSO observatory view [90].

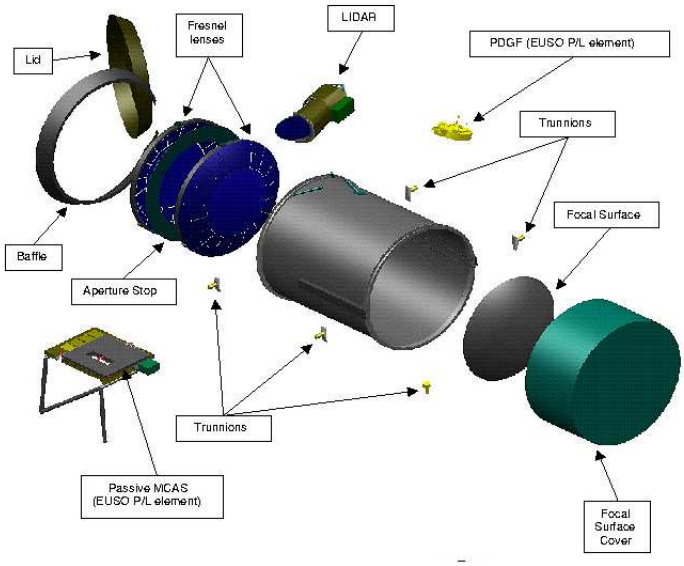

Figure 3.4: EUSO observatory view [90].

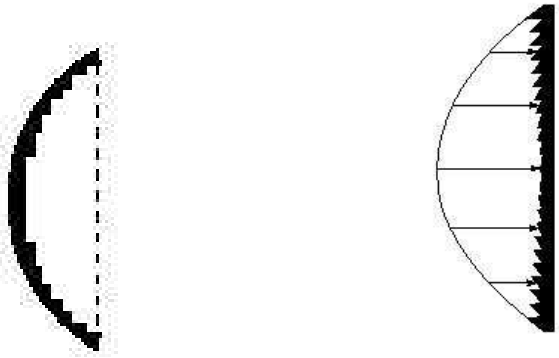

Figure 3.5: Fresnel lens structure [99].

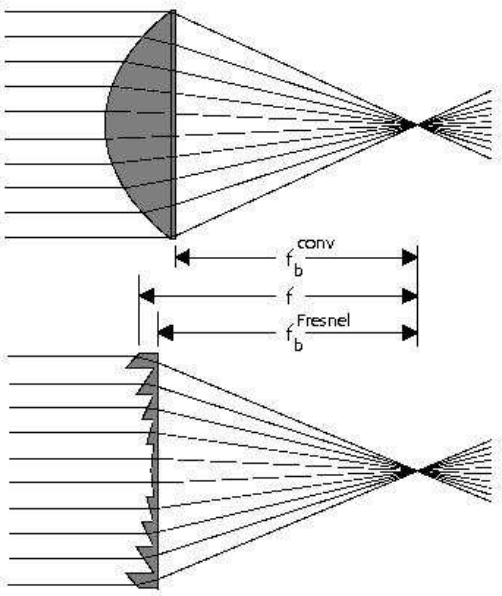

Figure 3.6: Principle of working of a Fresnel lens [99].

won't have the quality of the original one because of the many irregularities present on this new surface.

There are however many advantages in this kind of structure. The first is the large field of view. The second is the short focal lenght. Another important point is the limited weight that can be achieved with this kind

of structure. In fact, in order to reach very large fields of view we need a low ratio between focal lenght and lens diameter. This is simply for a geometrical reason: the nearer is the focus to the lens the bigger is the field that can be seen from the focal surface. Fresnel lenses have the property of having short focal lenghts. This is achieved because of the really small radius of curvature that can be mimicked by Fresnel lenses. In fact looking at the lens maker's formula we find that for a symmetrical lens the smaller is the curvature radius the shorter is the focal lenght. However a small radius of curvature means also a thick lens. That's why a normal lens could never reach those performances: it will be too heavy and will absorb too much. Therefore a Fresnel lens is the best solution in order to have a lens with such properties.

In the phase A of EUSO, the lenses material baseline was the PMMA. This is a plastic material used for this kind of applications. The advantage is that PMMA can be relatively easily shaped and its density is pretty low.

A second critical optics element is the baffle. This is needed to reduce lateral background. With this component we reduce the rate of photons arriving at the lens with a too big entrance angle. In fact the irregularities of the lens can scatter photons so that in the end they could finish on the focal surface contaminating the signal.

In EUSO, also an aperture stop was present. This is a diaphragm to make the aperture narrower in order to reduce vignetting and other aberration effects. Eventually we have the lid, to stop the direct sun light. The lid is closed each time the instrument will be under a too strong light. Otherwise the PMTs could be burnt due to too strong illumination.

Filters are deposed on the PMTs surface to reduce the number of counts originated by photons at other wavelenghts.

The last element of the optics system are the light collectors on each PMT. Those optical parts are thought to reduce geometrical effects of voids between different photomultipliers.

3.2.2 Electronics

The focal surface is made by a highly pixelized, single counting, fast photomultipliers. The baseline for the EUSO mission was the Hamamatsu R8900M-03-M36. This is a 36 channels bialkali photomultiplier. The detection efficiency was around 14% at 30° resulting by the multiplication of the 20% quantum efficiency of the photocatode and 70% of photoelectron collection efficiency. The photomultiplier is square with 27mm side and it weights 27g. About 83% of the detector cross section is sensitive area. The gain when a voltage of 900V was applied is $\simeq 10^6$. The photomultipliers are

organized in groups of four in what is called Elementary Cell (see chapter 5.3.2 and following of EUSO Report on the Phase A Study). In Fig. 3.7, the Elementary Cell is shown.

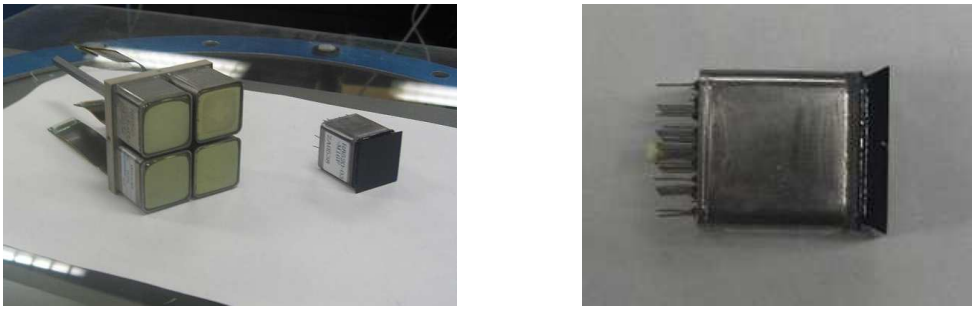

Figure 3.7: A photomultiplier with an elementary cell (left) a photomultiplier seen from the side (right).

The Elementary Cell is the basic unit of the detector. This means that independently from the focal surface layout this unity won't change. At each Elementary Cell one Front End Electronics Chip was attached.

Charachteristic	Value
Section	25.7×25.7 mm
Lenght	27mm
Fraction of sensitive area	0.83
Gain (at 900V)	$\sim 10^6$
Weight	27g
Quantum efficiency	0.2
Photoelectron collection efficiency	0.7
Pixelization	6×6
Pixel size	4.5×4.5 mm
Pulse rise time	1.5 ns
Transit time spread	0.3 ns

Table 3.2: R8900-03-M36 parameters [90].

Elementary Cells are arranged in bigger unities called PDMs [1]. Those are just physical unities not implying any logical elaboration of data. The highest electronics level are called Macrocell. This was an ensemble of Elementary Cells of variable geometry (see Fig. 3.8). At this level was based the triggering logic.

[1] Photo Detection Module.

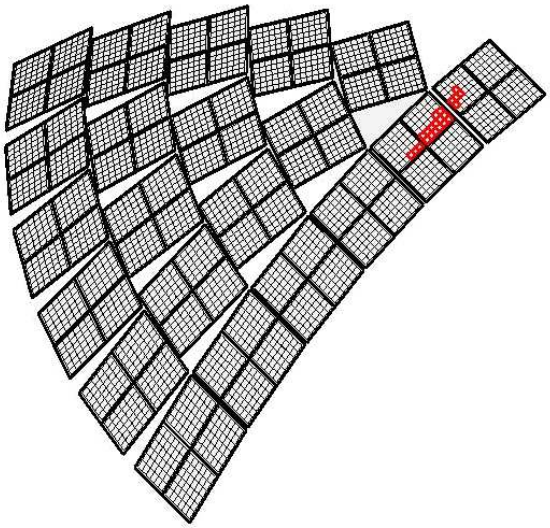

Figure 3.8: A EUSO macrocell.

As result of Phase A Study, there were still two options for the layout under consideration. The first was a θ-ϕ the second was a x-y layout. How those options looked like is shown in Fig. 3.9.

Once the photon hits the sensitive area of the photomultiplier, a photoelectron is produced and the electron cascade is originated, the anodic signal should be collected, amplified and filtered from the noise. These are duties of the so called Front End Electronics. Furthermore this part of the electronics has to count the number of photoelectrons and store the number of counts of each GTU [2] in a ring memory. This is in order to set also a digital threshold on each single pixel. The double hit resolution should be of the order of at least 10 ns but possibly even less. This is because we need single photon counting capability. In fact if we want to reach a threshold as low as possible we have to be able of counting with good reliability also signals done by just a few photons. The Front End Electronics has to be able therefore to discriminate currents just a fraction of what is generated by a single photon. However the photomultiplier should be also able of working in charge integration mode in order to be able of measuring much more intense signals like atmospheric phenomena or meteors.

Another requirement was that the depth of the ring memory had to be

[2]Gate Time Unit. This is the time in which all the counts in a channel are integrated or in other terms the clock for the channels read out. For EUSO it was 2.5 μ s.

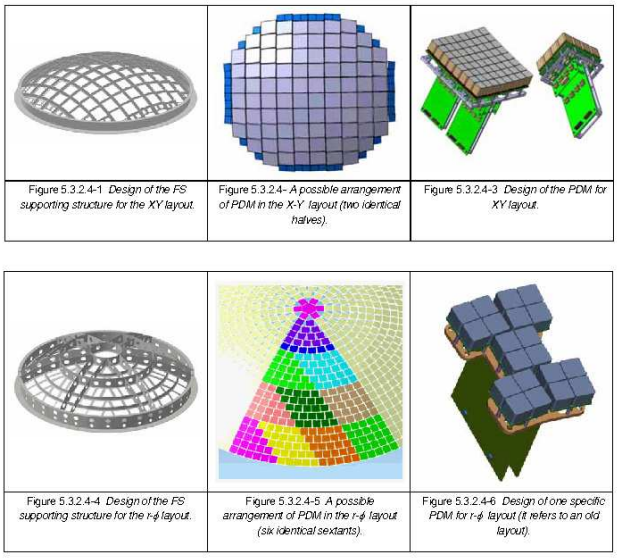

Figure 3.9: Different layouts for euso focal surface [90]. Upper panel: supporting structure, overview and PDM in x-y layout. Bottom panel: supporting structure, overview and PDM in $\theta - \phi$ layout.

at least of 128 GTUs.

The Read Out & Control (RO&C) is a critical element for read out, trigger, data handling and control. Some of those elements were based at the PDM level while some other at the macrocell level. Here are functions like the trigger track finding, the GTU clock, power supply system, interfaces with EC and many others. Last we have, the control electronics where the activity of the lid, the atmospheric sounding device, collection, pre-processing of the scientific data, emergency operations and control of the instrument operative mode is managed.

3.3 JEM-EUSO

Following the standby of EUSO decided by ESA the mission has been reoriented toward a new concept: JEM-EUSO. JEM-EUSO is basically an EUSO-like mission. The instrument is always a digital UV camera attached on the ISS but not more to the Columbus (as it was for EUSO) but to the Japanese module JEM. Some improvements have been introduced in the instrument design and technology. These changes affect mainly the optics, the focal surface and the electronics. The major parameters of the JEM-EUSO mission

are shown in table 3.3.

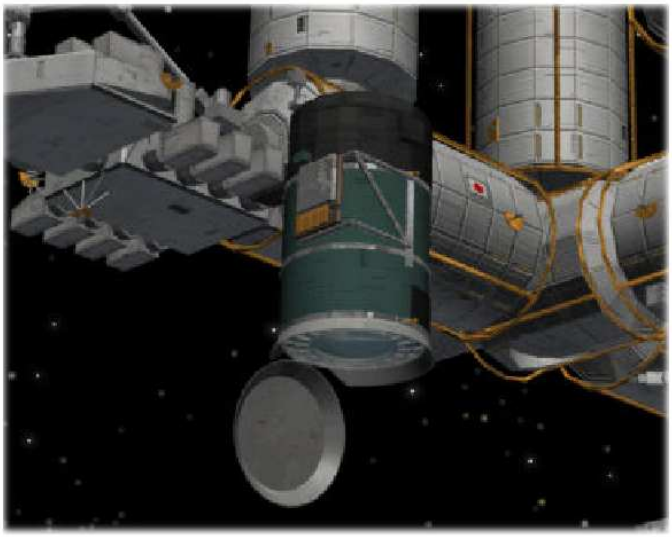

Figure 3.10: JEM-EUSO artistic view.

3.3.1 Optics

The JEM-EUSO optics is always refractive. First of all a new material is used, the so called CYTOP [3]. Compared to the PMMA [4], the baseline for EUSO, in CYTOP we have a 50 % smaller dispersion and a higher UV transparency (90-95 %) [77]. A new design has been also developed at RIKEN (in Japan). The optics remains a system of double Fresnel lenses of 15mm thickness each. However another diffractive plan has been added between the lenses, to reduce chromatic aberration effects. As result both point spread function and absorption are improved. This material is however much denser than the PMMA. This will make the optical system weight 480kg instead of 273kg. This mass can be accommodated within the available resources on the JEM module.

3.3.2 Electronics

Also the focal surface layout has been changed. Now just a x-y layout is considered. This reduces, with respect to EUSO, the voids between the

[3]CYTOP is a UV transmitting fluoropolymer.
[4]PMMA is a UV transmitting polymethyl-methacrylate

Charachteristic	Value
Height	430 km
Latitude coverage	± 51 deg
Orbital period	1.5 hours
Operational life	3 years + 2 extension
Instrument duty cycle	≤ 0.25
Optical band width	330-400 nm
Maximum diameter	2.5 m
Field of view	± 30 deg
Focal lenght	≤ 2.5 m
Focal surface radius	1.13 m
Optics structure	Double Fresnel lens + correction plan
Optics material	CYTOP
PMT	Advanced R8900M-03-M36
FS layout	X-Y
Geometric instantaneous aperture	$6.8 \times 10^5 km^2 sr$

Table 3.3: JEM-EUSO mission parameters [77].

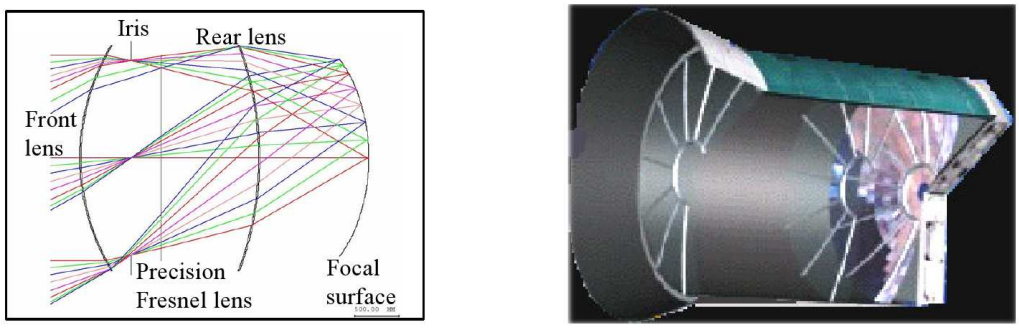

Figure 3.11: JEM-EUSO optics structure [77].

elements and results in a better coverage and better efficiency. In one word more signal will be detected. This kind of structure is shown in Fig. 3.12.

The photomultiplier baseline is always the Hamamatsu R8900M-03-M36 with an improved detection efficiency. This bialkali photomultiplier can reach more than 26% detection efficiency averaged in the range 300-450nm. This has been achieved combining a wavelenght shift layer, a dichroic mirror and GaAsP(Cs) cathode (see Fig. 3.14).

Silicon PMTs [106] are also being studied as possible detectors for JEM-

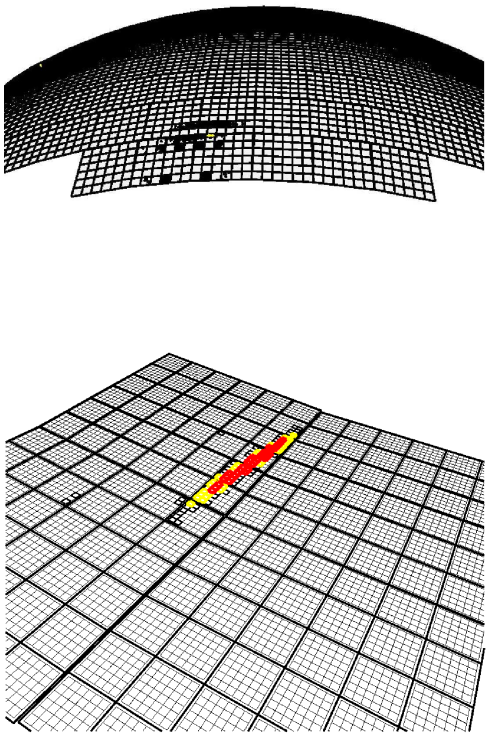

Figure 3.12: JEM-EUSO focal surface layout.

EUSO. In this case an efficiency higher than 50% can be reached. Furthermore, PMTs with different pixel sizes are under study. A finer pixelization would help to increase the signal-background ratio and provide a better resolution. On the other hand, it requires a much heavier readout procedure. Using bialkali cathodes, PMTs with 64 pixels can be easily manufactured. Higher pixelizations are more difficult. Silicon PMTs [106] can easily have 64 pixels, and pixelizations up to 256 pixels are under development.

As in the case of EUSO, four photomultipliers are organized in elementary cells. These organized in groups of 3×3, make a PDM. PDMs are in JEM-EUSO the triggering units. They are shown in Fig. 3.15. At PDM level is executed the trigger algorithm.

Let's look the scheme of Fig. 3.16. Here the logic of the electronics is shown.

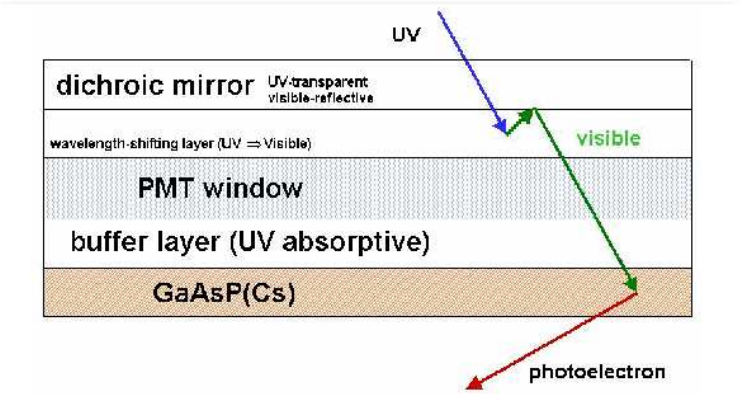

Figure 3.13: Structure of the high efficiency photcatode [90].

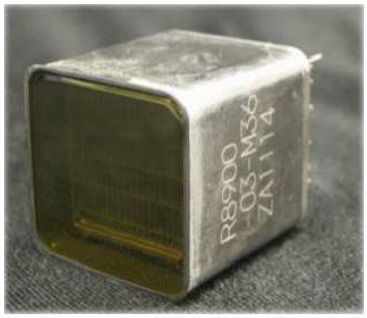

Figure 3.14: JEM-EUSO photomultiplier.

As we said, in the first block we have the Front End Electronics. This is the part of the electronics devoted to the PMT's signal amplification, collection and at this level will be setted the threshold on current in order to discriminate between a signal from a photon and noise. In this section it is therefore decided the analog trigger at the level of one single pixel. This will be done by an ASIC application. The threshold has to be of the order of 0.25 of the current generated by a single photoelectron in order to allow single photon counting.

Once a count is detected, the position and the time of this event is saved in a ring memory of a programmable depth. If a predefined number of counts within a time frame happens then a pixel level trigger will be issued. All of those digital operations are performed in a FPGA [5].

[5]Field Programmable Gate Array: those semiconductor devices are generic but

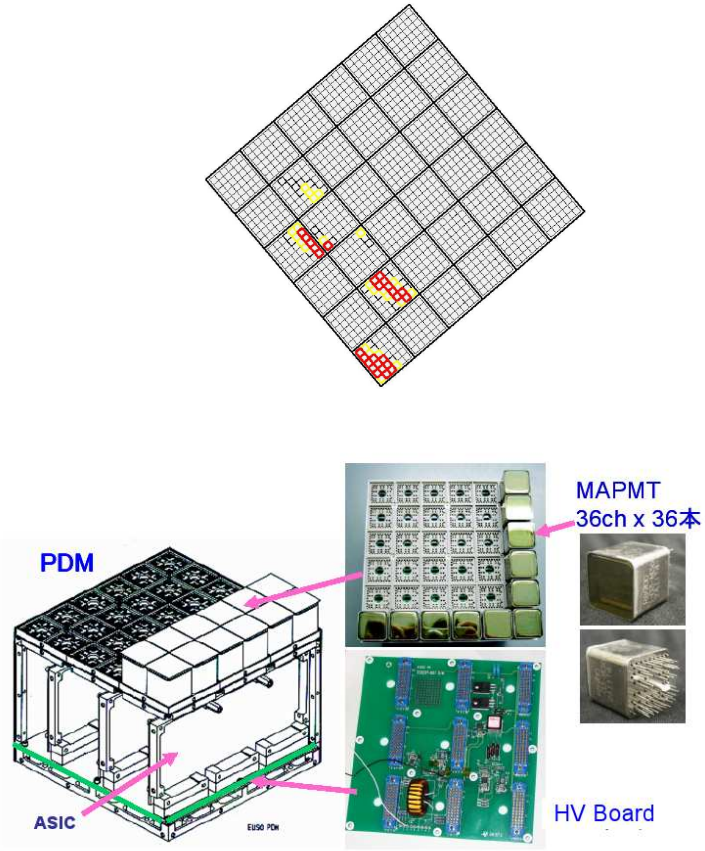

Figure 3.15: JEM-EUSO PDM.

In the second block at the level of the so called PDM control board the real core of the trigger algorithm (based on track or pattern recognition) is implemented. Aim of this block is to reduce the fake trigger events rate from several kHz/EC to some Hz/EC.

The third step occurs at Cluster Control Board (CCB) level. A group of 8 PDMS is organized in one Cluster. At this level the fine trigger is performed. The algorithm is similar as for the PDM trigger, however a lower event rate

programmable components. They distinguish themselves from the ASICs (Application Specific Integrated Circuits) exactly by the fact that in this last category we find all the components created specifically for some application while FPGAs are programmable. We could also say that FPGAs and ASICs are respectively the software and hardware approach to a problem. Therefore FPGAs are more suitable candidates for small scale use while ASICs for large scale and commercial productions.

makes possible to repeat the algorithm at a much finer grade. This level should further reduce the trigger rate to some mHz/EC making it compliant with the telemetry constraints.

The last block is the Focal Surface Control Board, which manages all the operations regarding the functionalities of the instrument as a whole: the movements of the lid, the atmospheric sensor, the communication between unities, interface management, trigger mode, operational mode (tilted or nadir) and many others.

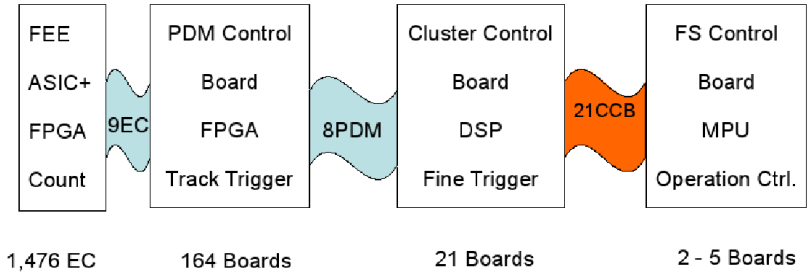

Figure 3.16: JEM-EUSO electronics scheme.

JEM-EUSO is being designed to operate also in tilted mode. In tilted mode the surveyed area will be larger than in Nadir mode. Therefore we will observe a much greater number of high energy particles. On the other hand we will also have a much stronger background and showers will be more distant. Tilting JEM-EUSO will affect the threshold. To observe the lower part of the spectrum, we have to operate in nadir mode. If we want to observe the higher part of the spectrum (where the flux is lower) we could work in tilted mode.

As last issue the atmospheric monitoring is worth to be mentioned. The profile of a shower in presence of clouds is shown in Fig. 3.18. Comparing with Fig. 3.1 we see essentially 2 differences. The first one is that the fluorescence profile is truncated. The second one is that the intensity of the Cerenkov peak is increased. This is respectively because the final part of the shower will develop under clouds and because of the high albedo of clouds. Even more difficult to treat is the presence of aerosols or not dense clouds. In such cases those features are not even clearly visible. Anyway the knowledge of the clouds conditions appears to be a crucial issue especially in the reconstruction section where we should interpret the light curve and try to infer from that the real shower profile.

A UV laser device (the LIDAR) is designed as part of the EUSO instrument

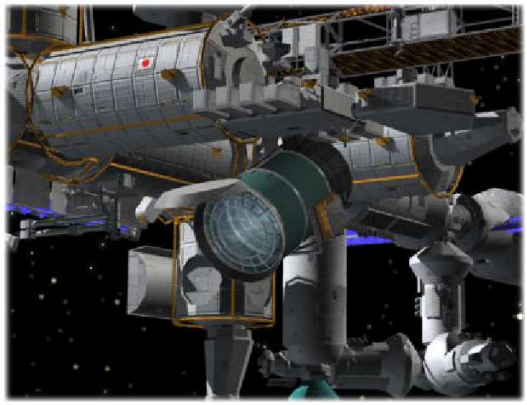

Figure 3.17: JEM-EUSO in tilted view operational mode.

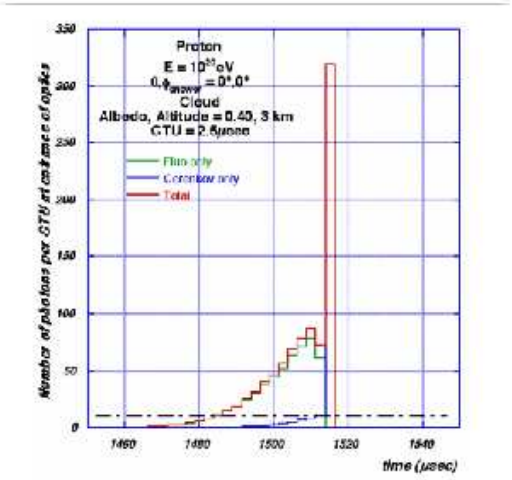

Figure 3.18: Light profile (photons at the pupil) of a shower with clouds (3 km height) presence [90].

in order to sample the detected atmosphere. This device sends a laser beam to Earth and by measuring the pulse timing detects the presence of clouds. The question whether to put in JEM-EUSO a LIDAR receiver or use the telescope itself as a receiver is still under discussion. Atmospheric sounding will be done also with an IR camera. This will have as field of view the same as the main optics. This camera will have to make an imaging of the clouds in the field of view of JEM-EUSO. The tandem LIDAR-IR camera will give in real time a good knowledge of the clouds condition.

Besides clouds, other atmospheric transient phenomena will affect the measurement. In this class we group lightnings and other electromagnetic phenomenas occurring in the upper atmosphere like elves, sprites and blue jets. Also very crucial is the issue of meteorites. They can however be very well distinguished by their very long duration. We eventually mention also the disturbance of cities, planes, ships and other human originated UV sources. For all of those kind of events some specific trigger mode has to be thought. For example meteors have a huge signal compared to EAS and therefore PMTs shouldn't work in single counting mode but rather in charge integration mode. Lightnings, sprites and elves are much extended: a trigger mode should be able to detect all of those kind of patterns. Whenever one of those events occurs the electronics should be able of switching mode in order to recognize them. These aspects were studied already for EUSO and details can be found in [90].

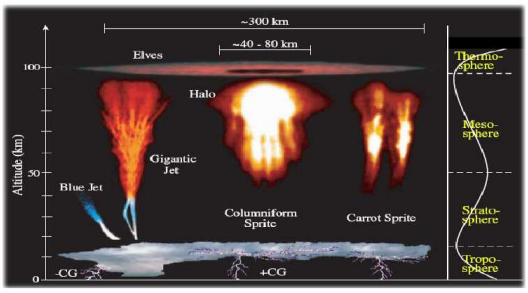

Figure 3.19: Atmospheric transient phenomena associated with lightnings [77].

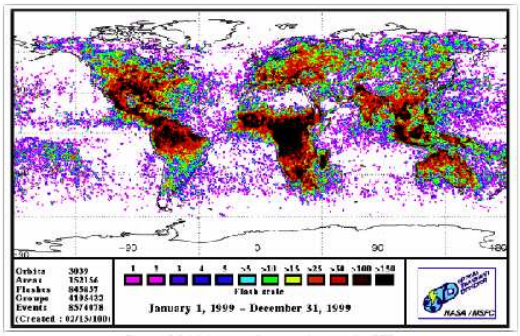

Figure 3.20: Lightnings frequency from satellite OCD [90].

3.4 S-EUSO

Super-EUSO is a mission proposed to ESA in the framework of Cosmic Vision 2015-2025 plan. This is an European led mission which plans to fly to investigate Cosmic Rays from space. At the present time the mission has not been selected by ESA among the first candidates, but a deeper study was recommended in order to solve some technological problem. In this view the JEM-EUSO mission can be considered as the pathfinder mission for S-EUSO.

Compared to the EUSO and JEM-EUSO the S-EUSO mission is structured in a totally different way. First of all the instrument will be a free flyer, which implies many advantages. First, the variability of the height of the orbit. An elliptical orbit with variable height between 800 and 1100 km is currently studied, to variate the energy threshold during the observational life. The second advantage is the easier operation of the instrument in tilted mode since we need no engine to tilt the telescope. The third advantage is the possibility to adjust the orbit to maximize the flight time over night, minimize flight over cities or under moon light in order to increase the duty cycle. Eventual, constrains on resources and safety are for a free flyer much less stringent than for the man-staffed ISS.

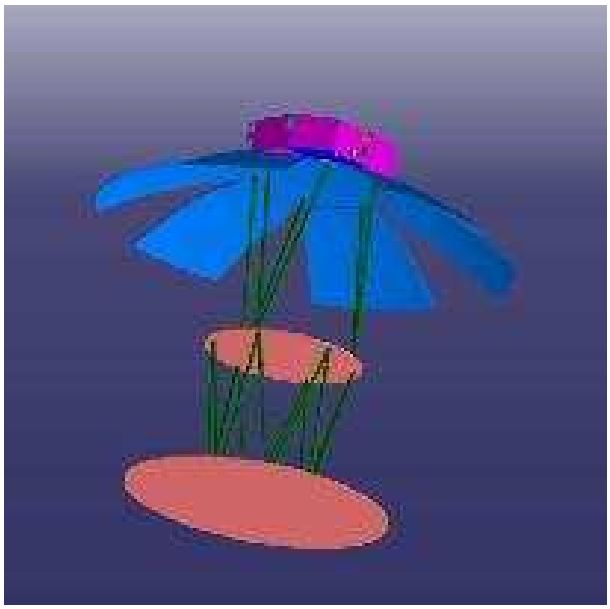

Figure 3.21: S-EUSO schematic view.

In S-EUSO the optics is catadioptric and not more refractive as in the case of JEM-EUSO. It will be based on a Schmidt design. A combination

of mirrors and lenses is used here like in the case of the Schmidt-Cassegrain telescopes. At the entrance pupil a front correcting plate is placed. This is exactly on the spherical center of the main mirror. The main mirror will focus the light on the photodetector which is in the camera at the focus of the mirror. The main parameters of the S-EUSO mission are summarized in table 3.4.

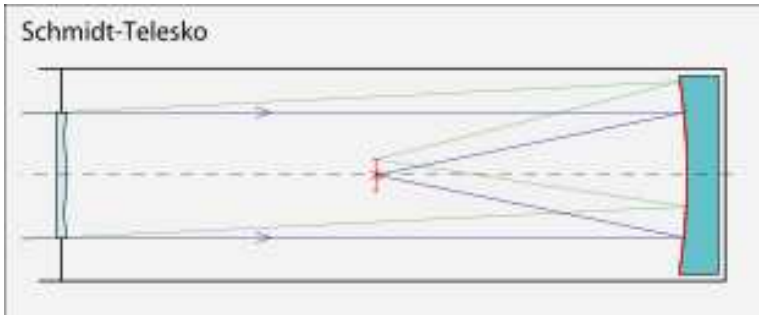

Figure 3.22: Schmidt telescope schematic view.

Aim of this kind of optics is to reach a large field of view just with a single spherical mirror. The FOV will in the end reach ± 25 deg. The developed design has a 7m diameter entrance pupil. However that is an easy to scale instrument. Anyway such a large diameter will oblige to use a deployable structure for the main mirror and perhaps also for the correction plan. Some conception study done for the OWL instrument can be seen in Fig. 3.23. We see here how the mirror has to be folded to be successively deployed in the space.

Figure 3.23: Impression of unfolding of OWL.

Optics must be adaptive. Due to the large diameter and the pretty light structure of the mirror we have to expect a not negligible deformation of the structure due to (for example) thermal expansion effects. That's why is necessary to build an active control of the mirror surface in order to compensate those thermal effects. This is however not a critical point since we don't need a really high resolution. Furthermore the frequency of an adaption in our case will not exceed some Hz. This kind of technology is already fully available at a much better quality than we require compared to on ground telescopes.

General details on the optics structure are however still under discussion. For example: is still not decided whether a single or multiple pupil layout will be used.

The electronics is still in the definition phase. Some constraint have been put on the capabilities of those detectors. First of all the pixel size should be of the order of some millimeter making this aspect not too different from the JEM-EUSO pixelization. A high quantum efficiency is required. Silicon photomultiplier are the most suitable candidates and are at the moment the baseline for the focal surface detectors. A time resolution of the order of some nanosecond should be achieved. The power and mass budgets should be respected.

The overall scheme both of electronics and focal surface could be similar to that of JEM-EUSO.

Charachteristic	Value
Height	500-1200 km
Orbital period	100 min
Operational life	5-10 years
Instrument duty cycle	0.1-0.2 (orbit dependent)
Optical band width	330-400 nm
Main mirror diameter	11 m
Pupil diameter	7 m
Field of view	$\pm$ 25 deg
Optics lenght	9 m
Focal surface diameter	4 m
Optics structure	Deployable catadioptric system
PMT	Si-PMT
FS layout	?
Geometric instantaneous aperture (800km)	$1.3 \times 10^6 km^2 sr$

Table 3.4: S-EUSO mission parameters [91].

Also an atmospheric monitoring device should be present in order to infer about the atmospheric conditions on the ground below the observatory.

To conclude we can mention the possibility to put on S-EUSO instrument also a radio antenna to detect the radio impulse from the shower [92] [93].

Chapter 4

Euso Simulation & Analysis Framework

4.1 Introduction

The acronym ESAF stands for Euso Simulation and Analysis Framework. The ESAF tool has been developed by the EUSO collaboration to provide EUSO scientists with an end-to-end simulation framework. In this chapter the software will be described in detail in order to introduce the reader to the real core of this work that will be later extensively discussed in chapter 5.

For each UHECR event generated, ESAF simulates the entire process from shower generation to light production and transport, to the detector response and eventually to the reconstruction algorithm. In the future also the scientific analysis will be introduced. ESAF has been designed in order that each part could be ran independently from the others. It is possible to run different parts of the simulation separately to check different configurations of the software. Another reason for the ESAF modularity is the possibility to reuse the reconstruction and the physical analysis once the instrument will fly.

The software is written in C++ using an Object Oriented Programming (OOP) approach. This allows very high modularity making easy the reuse of already written code or the change of modules without impacting on the entire code. ESAF runs on the ROOT package [100] [101]. Aim of this choice is to use this already tested, well recognized software. In fact the main application of ESAF inherits from *TRint*[1]. Moreover ESAF makes

[1]TRint is the ROOT Interactive Interface. It allows interactive access to the ROOT system via the CINT C/C++ interpreter.

large use of linear algebra classes, graphical classes, graphical interfaces and random number generators.

As can be seen in Fig. 4.1, ESAF is structured in a multiple layer structure. The higher layer is the *EusoApplication* module. This is the part devoted to the organization of all the different and more specific unities. It connects all the submodules of the second layer.

The *LightToEuso* module is devoted to the shower simulation, light production and transport. The *EusoApplication* requests to *LightToEuso* a number of photons on the pupil. In other words this subsystem delivers to the next (the *EusoDetector*) the photons to be considered for the detector simulation. The other modules do not know anything about how these photons are produced. Photons can be red by file, produced in real time by different shower parametrizations (SLAST [102] [103], UNISIM [104]...) or (in the future) produced in real time by a Montecarlo simulator [108] as CORSIKA [105]. This part will also -in the future- simulate other phenomena like lightnings, meteorites or light transients.

The subsystem *EusoDetector* is devoted to the simulation of the detector response from "photons on pupil" to telemetry. The optics, the focal surface and the electronics are simulated. In this part the user can decide at which degree of accuracy has to be done the simulation. In fact starting from the optics one can simulate this task using a parametrization or doing a full Montecarlo simulation. The same applies to the electronics: the user can choose between different kinds of parametrization with different complexity level. At this stage the *LightToEuso* and *EusoDetector* parts are linked together in the so called *Simulation* application which is the executable of the entire chain from shower generation to telemetry production. *Simulation* runs both *LightToEuso* and *EusoDetector*.

The reconstruction module (*Reco*) accepts a telemetry object from the *EusoDetector* without knowing anything about the previous steps. The aim of this module is to reconstruct the physical properties of the shower like energy, direction and mass. This is a complicated task and requires assumptions on the shower development, atmosphere and earth albedo. Furthermore, extensive calculation are requested in many of the reconstruction parts. The reconstruction is performed on ground. The software developed in ESAF constitutes the base for the future analysis on real observed data.

The package will be completed by the *Analysis* module. This is the module devoted to physical analysis that will also perform the real data analysis. However this module hasn't been written yet.

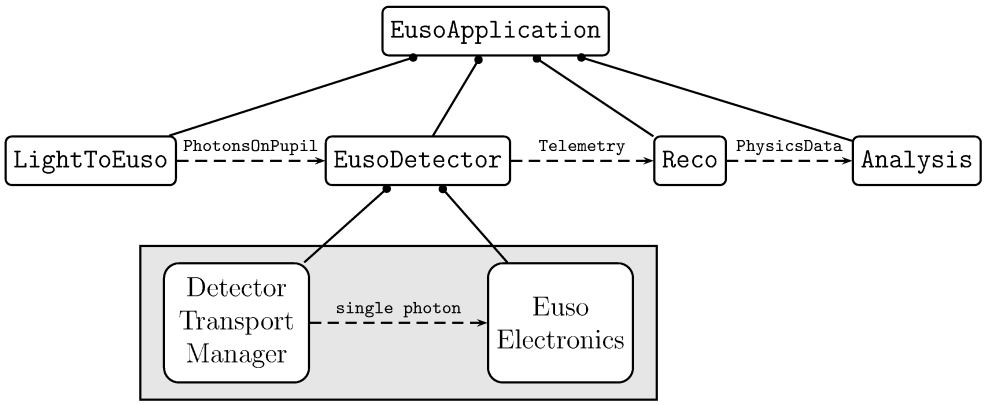

Figure 4.1: Structure of ESAF [107].

Some useful definition.

- ***Object Oriented Programming*** **: a programming paradigm that uses "objects" and their interactions to design applications and computer programs.**
- ***Class*** **: in object-oriented programming a programming language construct used to group related attributes and methods. It describes the rules by which objects behave.**
- ***Object*** **: an instance of a class. Instances of a class share the same set of properties. They may, however, differ in what those properties contain. Instances are created just at runtime following the "instructions" of the class.**
- ***Method*****: An object's ability. With methods an object is able of interacting with the external world.**
- ***State or attributes*****: set of object's characteristics.**
- ***Inheritance*****: concept referring to the possibility a class has to inherit characteristics from other classes.**
- ***Wrapper*** **: plays the role of message transformers, which are applied each time a message is sent or received through an interface.**

4.2 LightToEuso

The *LightToEuso* application is divided in three subsystems. The first one is the *ShowerSource*. This part is devoted to the simulation of the Extended Air Shower. It is an abstract interface that provides the *LightSource* with a *ShowerTracks* object. This object can be generated in several ways.

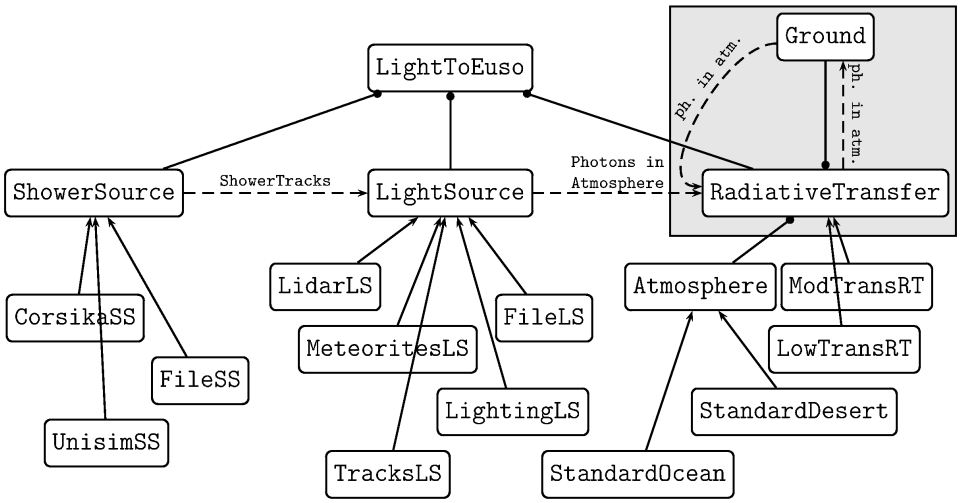

Figure 4.2: Structure of Light to Euso system [107].

The wrapper *CorsikaShowerSource* reads the shower parameters, calls the *CorsikaShowerSimulation* and eventually imports the results in ESAF. This is unfortunately not fully implemented yet.

The second one is the *UnisimShowerSource* wrapper. This module calls the *UnisimShowerSimulator*, which has been developed by INFN in Florence [104]. This simulator offers possibility to run fast parametrical simulations. Moreover it makes possible the generation of neutrino induced showers.

The third possibility is with the Shower Generator SLAST [102]. This acronym stands for Shower Light Attenuated to the Space Telescope. This software has been written in FORTRAN 77 and then translated into C++. It is present in ESAF both as interface with the FORTRAN part and as a complete simulator in C++. SLAST is not doing as CORSIKA a full Montecarlo simulation but it does a simple parametrization of the shower, which is a good way to optimize time consumption.

Another very good approach is to generate data with a shower generator, produce an input file and use it for ESAF. This is already implemented both for CORSIKA, Unisim and in a more general way for other kind of sources.

Once the shower has been generated a list of photons must be produced. This is the task of *TracksLightSource*. This class will generate a number of photons to be delivered to the radiative transfer part. *TracksLightSource* is inheriting from *LightSourceClass* as other classes like *MeteoriteLightSource* or *LightningLightSource*. Those classes that would allow the simulation of other phenomena haven't been implemented yet. These classes provide the radiative transfer with an object *PhotonInAtmosphere*.

Duty of the radiative transfer part is to bring the photons from the source to the entrance pupil. Of course it is useful to make the transport just for those photons with suitable direction. That means that just photons in direction of the detector will be simulated. This subsystem includes different atmosphere modellizations. Furthermore it includes also the possibility for photons to be reflected on the ground (the albedo in the code is set for simplification to 0.05).

4.3 EusoDetector

As the photons are on the pupil they are delivered to the next system. From this point starts the *EusoDetectorSimulation*.

As can be seen schematized in Fig. 4.3 the software is organized as the instrument in detector optics and electronics (which includes also the focal surface). The optics components are modeled as cylinders concentric to the longitudinal axis of EUSO.

4.3.1 Optics

In ESAF all the classes capable of interacting with photons will inherit from *DetectorPhotonTransporter* (see Fig. 4.4). Those classes will have the method *Transport* that will accept a photon object in entrance and deliver another in exit after the interaction. The family of *DetectorPhotonTransporters* is done by:

- *PhotonGenerator*
- *OpticalSystem*
- *FocalSurface*
- *Wall*

- *OpticalAdaptor*

The class *DetectorTransportManager* will treat all the *DetectorPhoton-Transporter* objects as black boxes. The ray tracing between different transporters will be done by this class that will propagate the photons rectilinearly between the various *DetectorPhotonTransporters*. Depending by which object has been hit a different transport method will be called. We will clarify the working principle of the detector optics following a photon path in the optics.

First of all the entrance of the photons in the optics is managed by the class *PhotonGenerator*. This is somehow the interface between the *LightTo-Euso* system and the *EusoDetector*. The photon is delivered to the *Detector-TransportManager* that propagates it rectilinearly in the detector. At this point the photon trajectory can intersect either the main optical system or the wall. One of those two classes further processes the photons. In the case of *OpticalSystem* the photon is either absorbed or transmitted and a new direction is calculated. In the case of the wall the photon can be reflected or transmitted.

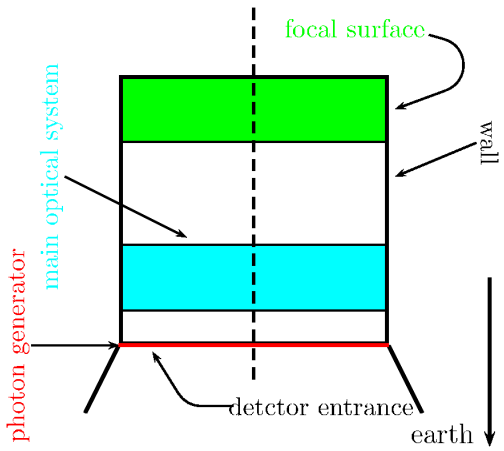

Figure 4.3: Structure of *EusoDetector* system [107].

The *DetectorPhotonTransporter* propagates the photon rectilinearly either to the wall or to the focal surface (and the optical adapter). If the photon reaches the focal surface it could hit also an optical adapter. Now the photon can be reflected, transmitted or absorbed. If the photon manages to reach the window of the photomultiplier the photon object is delivered to the electronics.

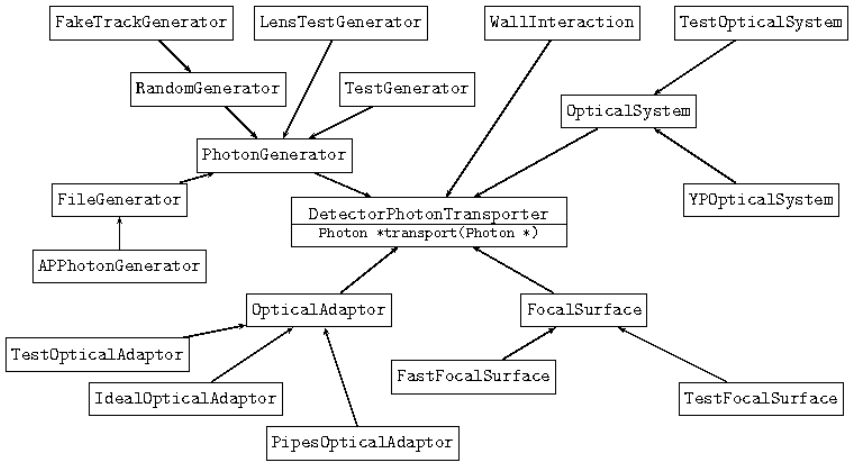

Figure 4.4: Detector Photon Transporter Classes [107].

Essential for this thesis is a particular kind of optical system simulation module: the *ParamOpticalSystem*. Based on the parametrization of the optics it allows us to simulate very efficiently many different kinds of optics with reduced computing time. Each photon is propagated according to its position on the lens and to its direction. The distance from the center of the focal surface is given by:

$$r = \frac{D_{max}}{\theta_{max}} * \theta \tag{4.1}$$

Whereas D_{max} is the maximum distance from the lens center (in other terms the radius), θ_{max} is the maximum incidence angle reachable (30 deg) and θ is the photon incidence angle. Furthermore the photon can be either absorbed or transmitted. A parametrization file expresses the probability for the photon to be absorbed for each entrance angle. The position on the focal surface will be calculated like explained before and then a random scattering in x and in y direction will be added. To decide the width of this scattering a parameter file, which defines the geometry of the so called Point Spread Function, will be given to the software. As parameter the σ of the Gaussian of the Point Spread Function for each incidence angle is given. In the same file a further column tells how many photons have been scattered outside

of the point spread function. This is to take into account the photons that will be scattered very far from the center of the point spread function. They won't be distinguishable from background anymore. The form of a simulated Point Spread Function is shown in Fig. 4.5. The equation of the PSF is:

$$psf(x,y) = Ae^{\frac{(x-x_0)^2}{2\sigma_x^2}+\frac{(y-y_0)^2}{2\sigma_y^2}} \tag{4.2}$$

This is an oversimplification since the real Point Spread Function is not a Gaussian but especially at large angles it has a much more complex form.

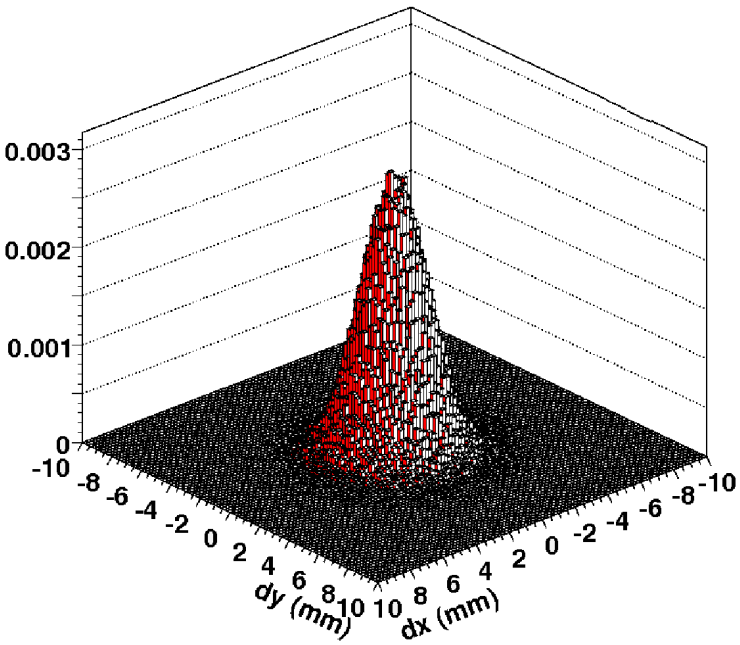

Figure 4.5: Schematic view of point spread function. This is not the real PSF rather just an approximation. We invite the reader to look at Fig. 5.21 to have an idea of a real PSF.

We then have to include in the simulation the focal surface layout. Each photomultiplier must be positioned and oriented in the space. We have to decide in which elementary cell, macrocell, PDM is the PMT activated by the incoming photon (see chapter 3 for the definitions of those elements). ESAF needs 3 vectors to decide the position of the PMT: the position of the uppermost left corner, the local y axis of the photomultiplier and the normal to the photomultiplier surface. The parametrization table is visible in Fig. 4.6. Fig. 4.7 can help in understanding the reference system.

Furthermore in order to understand the meaning of the configuration table one should look at Table 4.1.

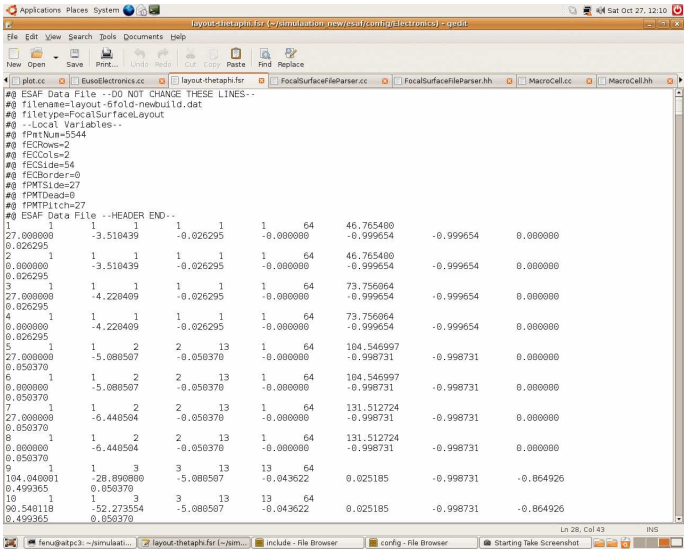

Figure 4.6: View of the focal surface parametrization.

In the configuration we are using the distance from the longitudinal axis at which the photon falls is also determined by the interaction between the photon trajectory and the focal surface profile. The equation of the height of the focal surface (parallel to the longitudinal axis) as function of the radius has to be provided to ESAF. To change the parametrization of the focal surface force to change also this equation. Once the position has been obtained the code looks in which PMT the photon falls.

4.3.2 Electronics

Once the photon hits the photomultiplier the signal is delivered to the electronics. We describe the most important classes in what it follows.

The *ElectronicsFactory* is the class that initializes each object in the electronics simulation. Then we have the class *EusoElectronics* which is the higher layer of the electronics simulation. This class holds the pointers to the macrocells. At the beginning of each event the method *Simulate* of *EusoElectronics* will define the significant time interval in which the electronics event will exist and it will calculate a random phase in order to simulate the random position of the event with respect to the GTU clock. After that the *Simulate* methods of each macrocell are called. At the end as output we will have an object *MacroCellData* which contains the response of the electronics to the event.

Colounmn number	Meaning
1	PMT ID
2	MC ID
3	PDM ID
4	EC ID
5	FE Chip ID
6	Offset row
7	Offset col
8	PMT Type
9-10-11	Position x-y-z
12-13-14	Normal x-y-z
15-16-17	Orientation x-y-z

Table 4.1: Meaning of the parametrization table of Fig. 4.6.

Another object is the *Photomultiplier*. The method *Add* of this class allows to add a photon to the PMT. This method is called by the optics. The response will be given as a set of *PmtSignals* objects. The PMT signals will be approximated by a Gaussian current peak. The amplitude and sigma of this pulse are given as parameter. The gain is decided also as parameter and is possible to be setted as a variable quantity. The *Simulate* method of the same class is called after the photon reached the focal surface. This function transfers the signals to the front end electronics. At this stage it is possible to add the background distributed as a poissonian source of noise. This is just in order to avoid the simulation of a huge number of background photons (look chapter 3 for more informations about background). Always for the PMT the function *PmtGeometry* is the description of the geometrical properties of the PMT.

Concerning the front end electronics we have the class *FrontEndChip*. This class holds a pointer to the attached PMT. The function GTU will return a *ChipGtuData* object where are stored the timing of the X and Y and the fast OR logic.

The *MacroCell* class constitutes the triggering unit of the electronics. The method *Simulate* returns the object *MacroCellData*. This method will also call the trigger algorithms.

In the end, we will have the *Telemetry* class in which all the data necessary for the reconstruction are collected and saved on the ROOT file.

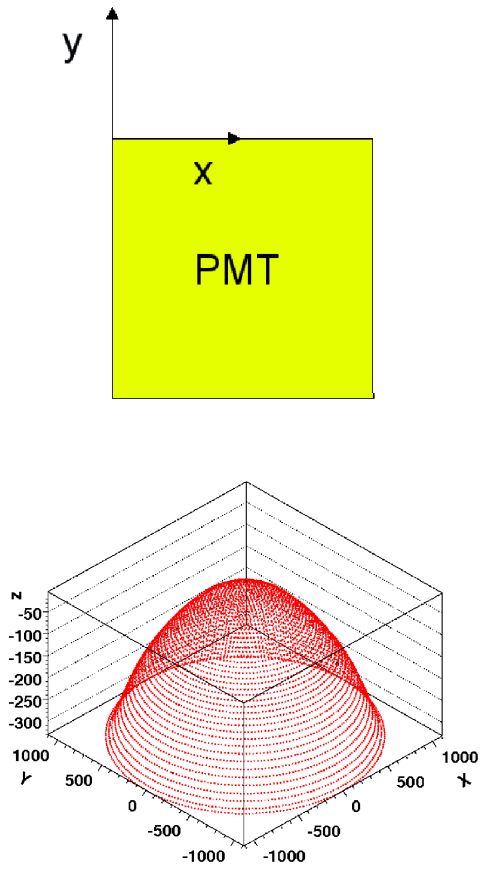

Figure 4.7: PMT's orientation and x-y-z coordinates system for ESAF focal surface. Data in axis are in millimeters.

4.3.3 Trigger algorithm

The trigger algorithm is essential for the optimization of the performances. Several trigger algorithms are implemented in ESAF and in the course of the thesis a new algorithm, specifically developed for JEM-EUSO, was implemented. Aim of the trigger is to try to extract the signal from the background sea. As we explained in chapter 3 the background photons are much more than those of signal. Therefore the electronics will have to reject as much counts as possible without rejecting the signal itself. Fortunately the signal has some peculiar characteristics that can be used to distinguish it. The shower generate a spot moving on the focal surface. On the other hand, the background is distributed randomly.

The first step is to set thresholds on each single pixel at the level of

the Front End Electronics. Only pixels with a number of counts above a predetermined threshold are considered fired. The threshold strongly reduces the presence of pure background counts. In fact it is the occurrence of "event plus background" that makes more probable the rise of the signal above threshold.

However the background is poissonianly distributed and local oscillations might bring it above threshold. This give rise to "fake triggers". On the other hand, it is not possible to reduce too much the probability of having the so called "fake triggers" increasing the threshold because in this case we would reject the signal itself. In the end the threshold has to be a trade-off between a low fake trigger rate and a sufficiently high signal detection efficiency. However if the fake trigger rate is too high the detector will be blind for good events. We invite the reader to check in the section specifically devoted to "fake triggers".

A further trigger level has to be inserted namely the *TrackingTriggerAlgorithm*. At a higher level those algorithms look for specific patterns using the fact that the signal is a spot moving on the focal surface in the time.

The *ChipTrackingTrigger* algorithm for example selects all the pixels around a pixel above threshold and it builds a track if one of them is above threshold in the following GTUs. If the track is longer than a preselected number of pixels we have trigger otherwise not. In order to clarify better the principle of working of this algorithm we show Fig. 4.8 (Courtesy of R. Pesce).

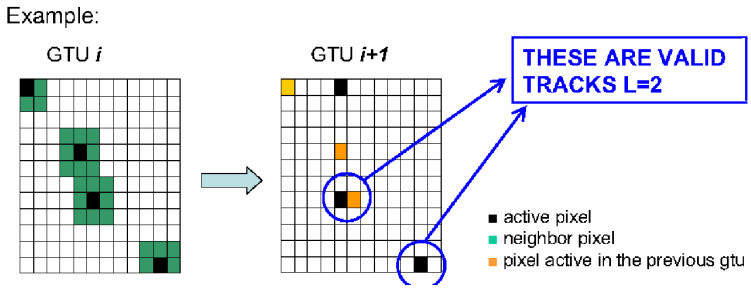

Figure 4.8: Chip tracking trigger algorithm [109].

As part of the diploma work we implemented in ESAF another tracking trigger algorithm namely the *LinearTrackingTrigger* algorithm originally conceived by M. Bertaina in Torino University [110]. The basic idea is to try to integrate the signal in a box following a predetermined set of directions. First of all at the level of each single pixel we define two thresholds dividing the pixels in three categories: red, yellow and "non active". The red are the

pixels with the higher number of counts, yellow pixels are pixel above the lower threshold while "non active" are even below the yellow threshold and are considered as background.

The algorithm selects all the red pixels and builds around each of them a 4 pixels symmetric box. According to a predefined set of directions the box will be moved following rectilinear tracks. Several different tracks are chosen in order to cover all the possible directions. However the number of directions must be limited due to the computational time required also considering the fact that these operations will be done in real time on board. The yellow and red pixel counts falling in this box must be added to an integration variable. If the integration result is higher than a preset threshold a trigger is issued. We show in fig. 4.9 a couple of schematic views in order to clarify the algorithm.

In our work we also estimated the performances of the LBL trigger algorithm. This was simply to have a more complete comparison of the real capabilities of the different trigger algorithms. We will describe it very briefly since this was not developed by the authors and we didn't find any official documentation describing this software. The basic idea of this software is to integrate on single pixels for a predetermined number of GTUs. After this interval we will move in one of the nearby pixels continuing the integration for the same amount of time. This operation has to be repeated a predetermined number of times. If the number of counts integrated exceeds a preset threshold a trigger is fired.

4.3.4 Fake triggers

We already say that a crucial aspect of each simulation is the background. We also explained that in presence of background a certain number of Fake Trigger Rates (FTR) is expected. Aim of a trigger algorithm is to reduce this rate without affecting too much the real events rate. For example a too high FTR would make impossible the calculation of the efficiency curves we will show in chapter 5. This is because for weak signals (not able of generating triggering tracks) we will have several fake tracks generated by background that will increase the dead time. On the other hand too strong thresholds will reduce the trigger efficiency in the energy range of interest.

ESAF can also work in a configuration in which just background is generated. This makes possible running tests to have an idea of how many fake events we would see with a particular set of thresholds. In fact ESAF can add counts in the Front End Electronics in order to simulate background.

We choose 1Hz/EC as a reasonable FTR for the PDM control board trigger. That means that each second on the entire focal surface we will

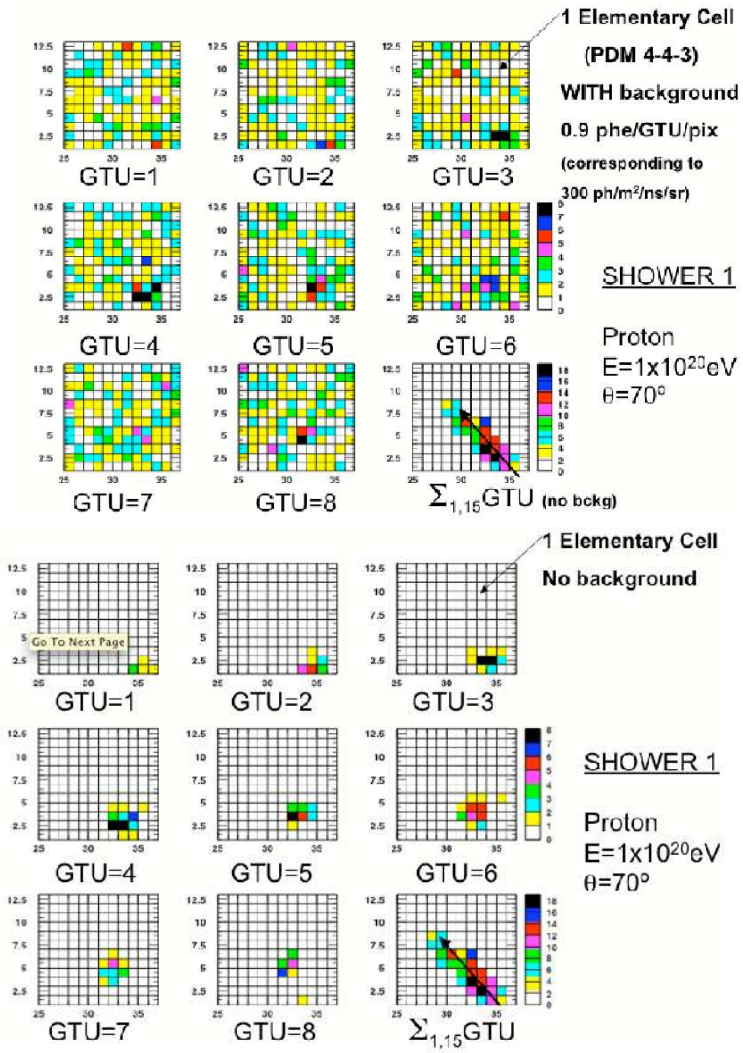

Figure 4.9: Principle of Linear Tracking Trigger Algorithm [110]. On the upper panel we see how it could look like the PDM with signal + background. We see here also the track that can be extracted from the integrated signal. In the bottom panel we observe just the signal. Color scale indicate how many counts have been reached in each pixel.

have something like 1000 fake events. However we expect by introducing the Cluster Control Board trigger to reduce a lot this rate. Furthermore the PDM trigger itself has to be further improved.

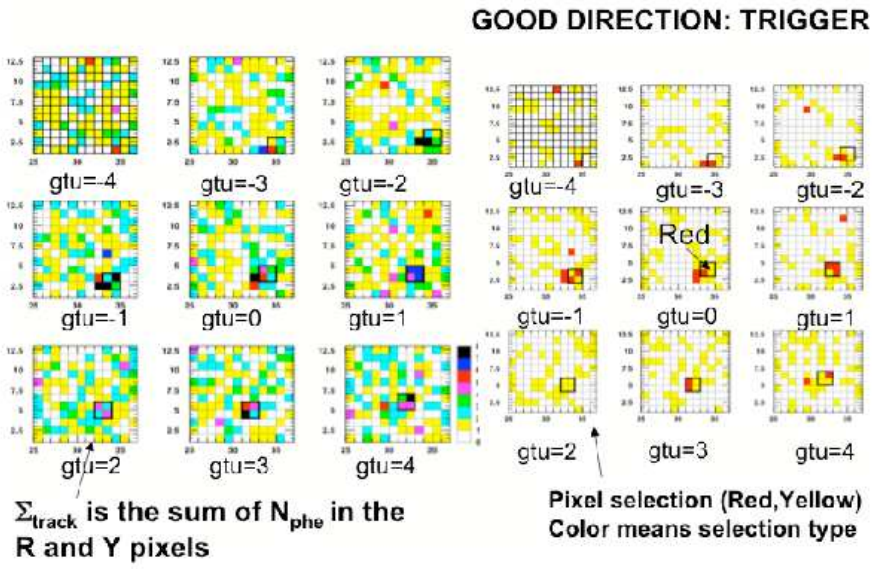

Figure 4.10: Principle of Linear Tracking Trigger Algorithm [110]. We observe here the integration box moving on the PDM. On the left we see the signal + the background. Color scale indicate how many counts have been reached in each pixel. On the right we see the box moving on the PDM. Pixels are here divided in tree categories: red, yellow and "non active".

4.4 Reconstruction

Aim of the reconstruction part is to take the detector response and to reconstruct the physical properties of the event. We give below an overview of the structures making this part.

Those structures are:

- Input module: this module handles the reading of the events for the reconstruction. (Both from .root files and real data stream).
- Event container: It's the container structure for the event that should be reconstructed.
- Reconstruction Framework: this is the structure that builds the chain of reconstruction modules.
- Modules: here we have all the modules for the reconstruction. Those modules will be called and each of them will accomplish a particular task.

- Configuration files: in this section are input files and the definition of the processing modules to load.

- Access to databases: the reconstruction will need to access the run conditions database and to the detector calibration database.

Let's give a general idea of how the reconstruction procedure works. First of all in order to recognize an event we will have to find a group of triggering events clustered in a limited region of the focal surface. We apply a pattern recognition algorithm to extract real events from the fake triggers sea. The signal is represented by a spot moving on the focal surface. Therefore we would expect to find several active pixels along a track. The principle of clustering works as follows: we identify all the triggering pixels with θ and ϕ field of view coordinates. Using these coordinates we try to link the points between them. For example we could connect two points and say that the weight of this connection is inversely proportional to the distance between the points. If the weight is above a threshold those points are defined to be in a cluster. The process continues and in the end we will possibly have a group of points clustered. We can define a cluster to be significant just if it is larger than a preset threshold.

Furthermore we try to clusterize the events in order to further treat those data. In fact once the significant cluster has been build we will have to find the direction of the shower. We first find the common plane in which both detector and track lay. This is done by means (for example) of least square fit. Then we need to do a timing clustering between the cluster's points in order to find the time profile of the shower. Knowing the speed of the spot on the focal surface is possible to reconstruct the inclination of the shower. This is because of the constant velocity of the shower (that is moving at the speed of light) and of the fact that the distance between shower and detector is almost constant during the shower development.

A really powerful tool to determine the geometry of the shower is the Cherenkov peak in the light profile created by the diffused reflection of the Cerenkov beam on Earth's surface. This greatly helps in reconstructing the shower direction and the shower depht. The shower direction is better reconstructed for a geometrical reason: the Cerenkov peak falls on the projection of the track. This will help the fitting process to find the direction of the shower. Moreover, by measuring the time delay of the Cerenkov spike we also obtain a precise information on the height of the shower.

Once the geometry of the shower is reconstructed, we could calculate the total energy of the shower. This could be done by integrating the total signal of the track. However we have to correct the profile with a modellization of

the atmospheric absorption profile as function of the depht. In ESAF we are using the LOWTRAN parametrization (we invite the reader to check the paragraph 2.5.2). The profile must be corrected also from the scattered Cerenkov component.

In the end will also be possible to reconstruct the type of particle using the depht of the maximum of the shower. Which kind of observables can be used to distinguish between different kind of particles has been discussed in chapter 2.

We give in Fig. 4.11 an overview of the principle of the reconstruction part.

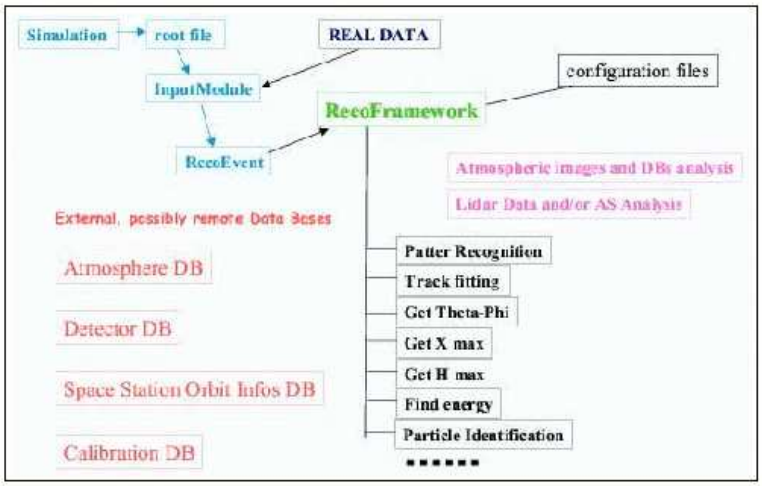

Figure 4.11: General scheme of reconstruction procedure [111].

Chapter 5

Results

We describe in this chapter the core of this diploma work presenting and discussing the results obtained from our studies on EUSO, JEM-EUSO and S-EUSO. As we already said in chapter 4, the ESAF software has been developed in the framework of the studies for the EUSO mission. Our work aims at extending ESAF to the JEM-EUSO and possibly S-EUSO instrument.

The first part of the diploma thesis has been devoted to the implementation and testing of the ESAF package through the reproduction of the results for the old EUSO configuration. We therefore evaluated both the detector response and the reconstruction performances of EUSO.

The second main part of our work has been devoted to the implementation of the *LinearTrackingTrigger* in the ESAF package. This is thought to be the baseline for the JEM-EUSO trigger algorithm. However after implementing this algorithm in ESAF we used the well known EUSO configuration to compare the different trigger algorithms and assess their performances.

The third part of our work was the implementation of the JEM-EUSO instrument. New parametrizations for the optics, for the focal surface and for the detector efficiency were included in ESAF. The performances of JEM-EUSO were then estimated.

We concluded our work tring to give a first assessment of the S-EUSO performances.

In the next months we will work on the implementation of the cluster control board algorithm, on the PDM algorithm itself, on the reconstruction for JEM-EUSO and on the S-EUSO implementation.

5.1 EUSO Simulations

5.1.1 EUSO detection response

As we said the first step was the "reactivation" of ESAF. The ESAF software has not been completed and therefore its usage results to be not simple. We learned how to use it, some basics of ROOT, of C++ and of Object Oriented Programming. Preliminary work has been devoted to the implementation and optimization of the ESAF package.

Using the parameters summarized in table 3.1 (but see also EUSO Phase A Red Book) we first recalculated the EUSO trigger efficiency shown in Fig. 5.1. Here we see that 50 % is reached at energy greater than 10^{20} eV while the instrument is fully efficient at $4 * 10^{20}$ eV. The efficiency drop to 0 at $2 * 10^{19}$.

As shown in Fig. 5.2 we have also calculated the efficiency as function of angle and energy. We observe that the trigger efficiency strongly depends on the inclination angle. For more inclined angles a lower threshold in energy is measured. This can be understood because inclined showers produce more light compared to the more vertical. This is due to the greater lenght that can be achieved by horizontal showers and to the larger height at which the shower develops. The UV light is less absorbed from production to the detector because it traverses a smaller amount of air. It can be seen that selecting just very inclined showers we could reach 100 % efficiency even at energies lower than 10^{20} eV. This implies that also lower energies events would have been observed by EUSO.

5.1.2 EUSO reconstruction

We present here some result on the reconstruction of events by EUSO. First we simulated for four different angles showers with energy sorted by a power law $\propto E^{-1}$ and we blindly tried to reconstruct the direction angle and the energy. The angles we considered were 10, 25, 45 and 80 degrees.

Inclination angle (deg)	Average Reco. angle (deg)	0.68 val. Reco. angle
10.5	16.4	33%
25.5	22.08	21%
45.5	45.91	7%
80.5	80.54	1%

Table 5.1: EUSO reconstruction data. Real theta compared with reconstructed. The RMS value is the range in which 68% of the events will fall.

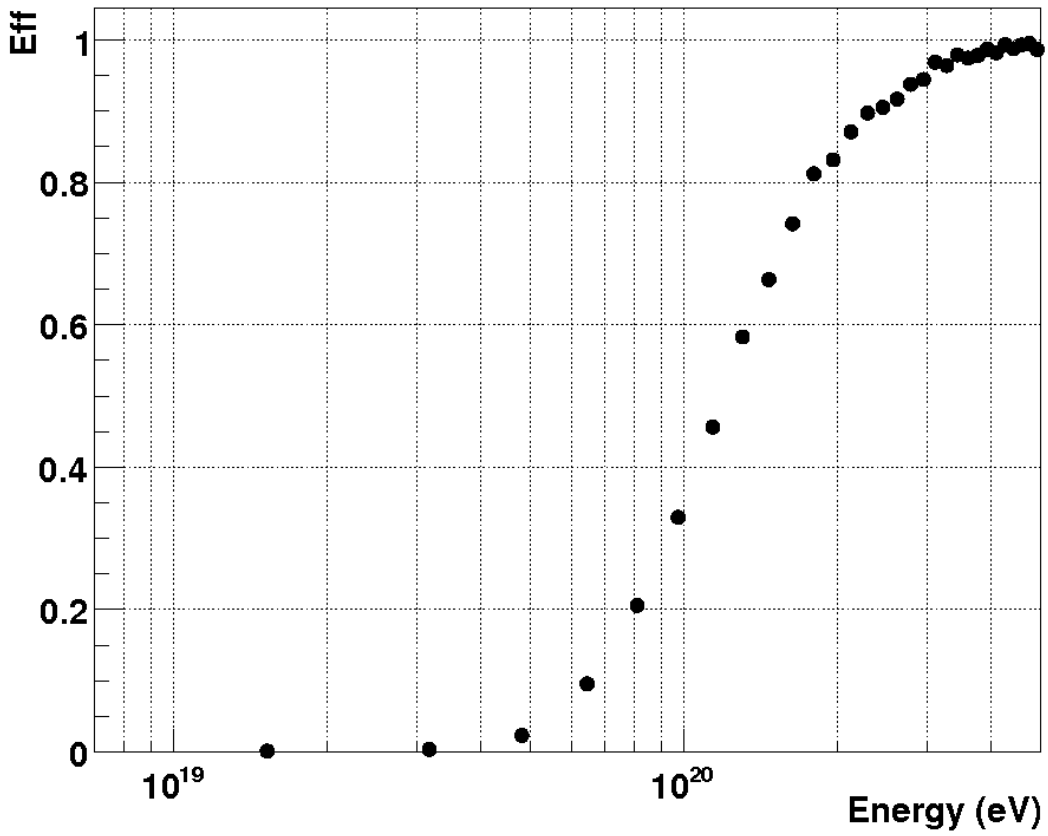

Figure 5.1: EUSO "Report Phase A" baseline optics efficiency curve. The curve has been obtained with background of 0.6 $\frac{photoel}{(pix*micsec)}$ (or 500 $\frac{photons}{(ns*sr*m^2)}$).

In Fig. 5.3 the reconstructed thetas are compared with the "true" theta, the green histogram gives the true inclination angles of the particle while the red histogram gives the reconstructed theta values. Reconstruction works much better for the very inclined events. This is because the long tracks on the focal surface are better estimated in the fits with respect to shorter tracks. On the other hand for low inclination angle e.g. 10 deg a very bad reconstruction of the angle theta is obtained. At these angles we have such short tracks and with so few points (see inserts in Fig. 5.3) that the least square fits are not even able to converge. Moreover in the clusterization there could be so few points that no significant cluster is even found. In table 5.1.2 the values of average reconstructed angles and root mean square are reported.

In Fig. 5.4 we plot for four different angles the *energy reconstruction*.

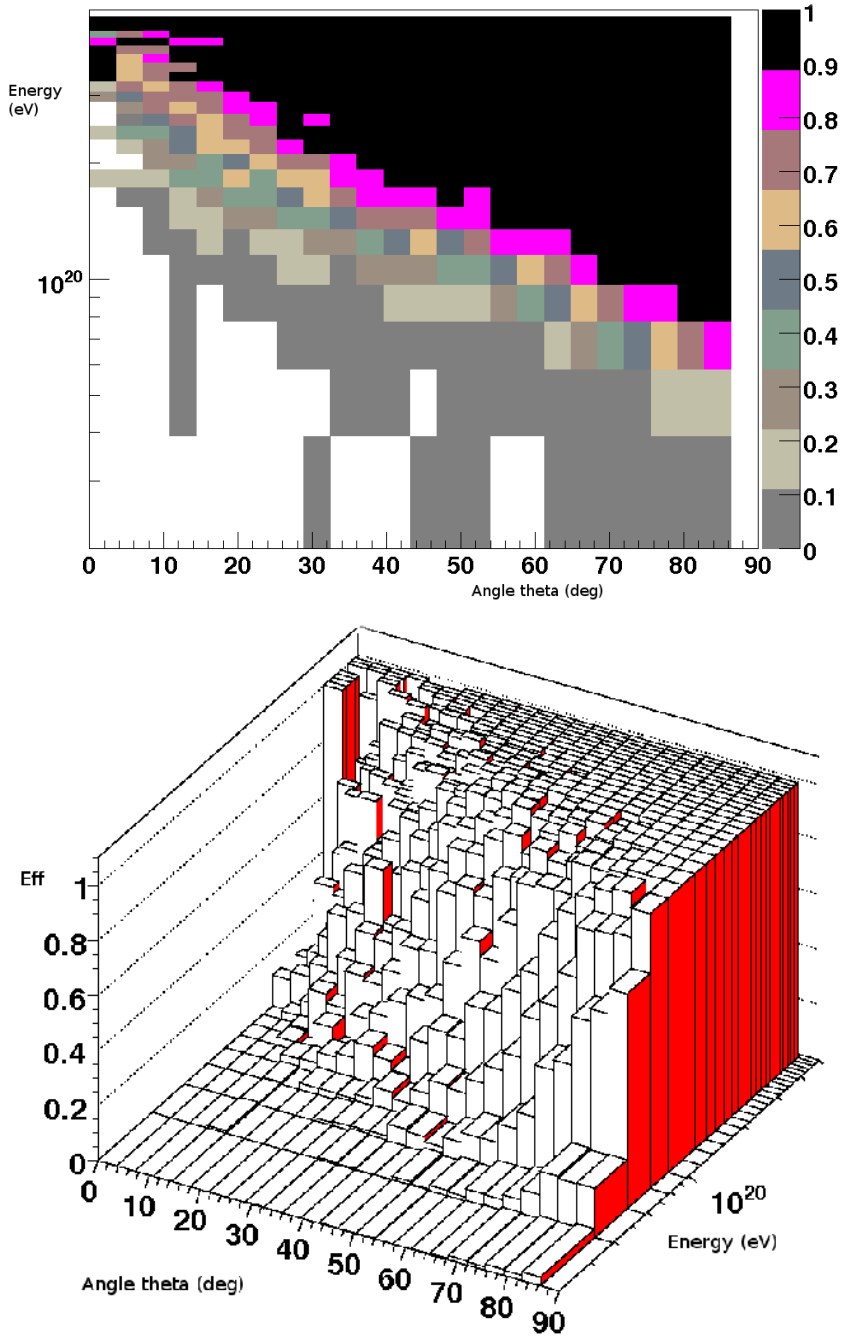

Figure 5.2: EUSO efficiency as function of energy and inclination angle. Curves have been obtained with background of 0.6 $\frac{photoel}{(pix*micsec)}$ (or 500 $\frac{photons}{(ns*sr*m^2)}$).

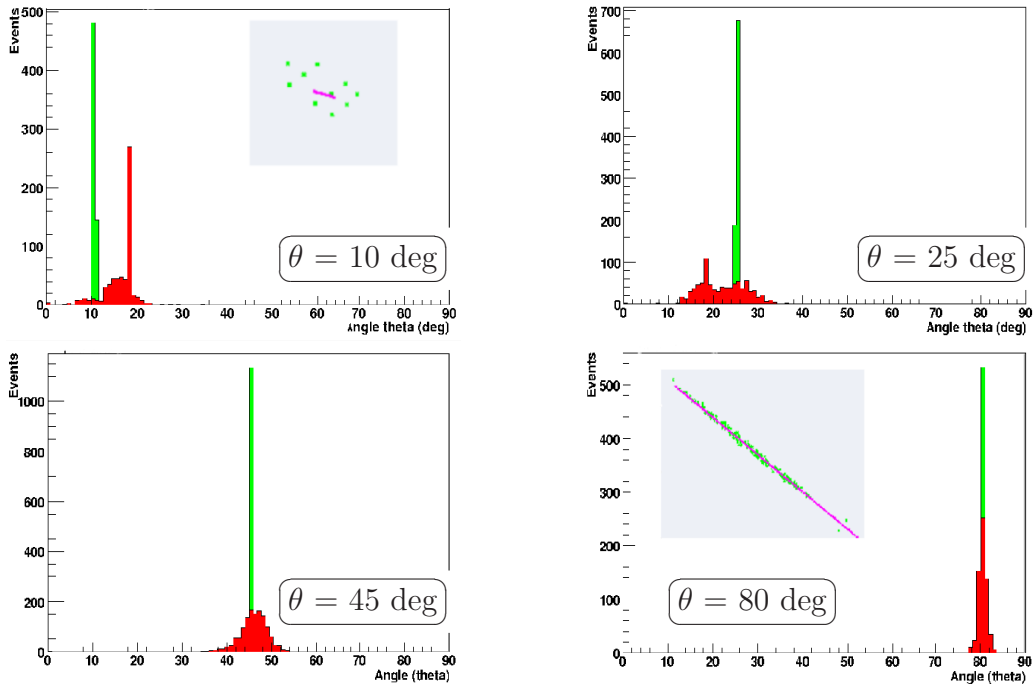

Figure 5.3: Reconstructed inclination angle (theta) superposed with true theta. Green histogram true theta, red histogram reconstructed theta. Results have been obtained with "Phase A EUSO Report" baseline configuration with background of 0.6 $\frac{photoel}{(pix*micsec)}$ (or 500 $\frac{photons}{(ns*sr*m^2)}$). In the inserts we see the cluster of activated pixels of two showers for very different inclination angle.

Here we plotted the difference between the logarithm of the true energy and the logarithm of the reconstructed energy. The energy spectrum follows always power law with index -1.

At 10 deg a sort of tail on the left part of the plot appears meaning that some events have not been properly reconstructed. This tail represents 5.9% of the total amount of triggering events. We analyzed carefully the characteristics of the events of the tail and we found that 83% of them have energy under 4×10^{20} eV. Those events are almost all in the range where the instrument (at this angle) is not fully efficient. We think that this is an unavoidable problem related to the bad light profile of this kind of showers. In fact for these events, it is not possible to make any profile reconstruction to calculate the dimension of the shower. This is due to the discontinuous and weak signal received on the focal surface, that converts in a discontinuos and weak time profile of the produced photoelectrons. We invite the reader to look at insert on 10 deg plot of Fig. 5.4. Those events are in the end

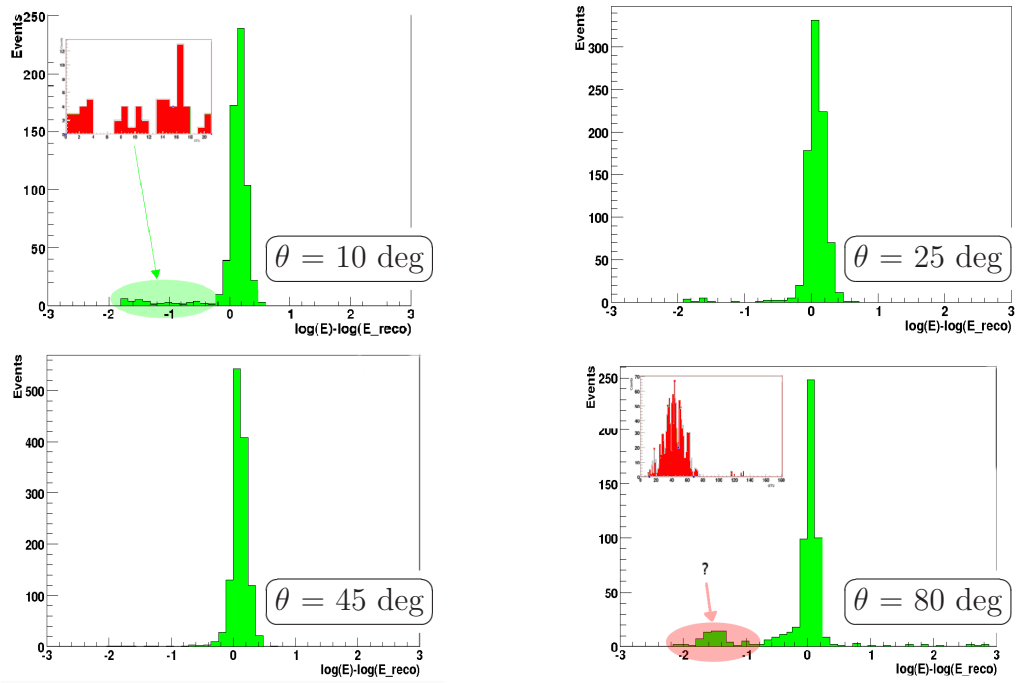

Figure 5.4: Reconstructed energy. We plot here the difference between the logarithm of the real and the logarithm of the reconstructed energy. Results have been obtained with "Phase A EUSO Report" baseline configuration with background of 0.6 $\frac{photoel}{(pix*micsec)}$ (or 500 $\frac{photons}{(ns*sr*m^2)}$). We show in the inserts the typical profile of a shower belonging to the tails we stress in the plots. We think that the tail for 10 deg is due to the bad profile of the shower. We do not understand the origin of the tail for 80 deg. This huge energy difference is not related to the profile.

not reconstructable neither in direction nor in energy and this suggests that strong cuts should be introduced to select usable events.

Also at high angles ($\theta = 80$ deg) a part of the events is badly reconstructed. We see in the 80 deg plot a peak on the left of the main one. In this peak we have 11.6% of the events. We analyzed carefully those events and it came out that they are high energy events. In fact 90.1% of them are in fact above 1.5×10^{20}eV. At this angle the instrument is in this energy range fully efficient. We carefully analyzed the time profile of many of those showers and we found that for those events the profile reconstruction doesn't work. This is not understandable since the curve representing the produced photoelectrons time profile is really strong and has the typical bell shape. We invite the reader to look at insert on 80 deg plot of Fig. 5.4. This should be easily reconstructable since this kind of profile is similar to the theoretical shower profile models we are using in the profile fitting algorithms. We concluded

Inclination angle (deg)	Average energy difference	RMS energy difference
10.5	0.076 (1.19)	0.35 (0.44-2.23) = 150%
25.5	0.053 (1.13)	0.25 (0.56-1.78) = 107%
45.5	0.096 (1.24)	0.17 (0.67-1.47) = 64%
80.5	-0.102 (0.79)	0.6 (0.25-3.9) = 460%

Table 5.2: EUSO reconstruction data. Tabulated $Log(E_{real}) - Log(E_{reco})$. In parenthesis data expressed as ratios between real and reconstructed energy ($\frac{E_{real}}{E_{reco}}$). The RMS value is the range in which 68% of the events will fall. In the third column between parenthesis are two values $\frac{E_{real}}{E_{reco}}$ calculated by using the value RMS as exponent but with different sign. The percentual value is obtained by dividing the width of the range in third column by the ratio in second column. We give here an example for the first line. In the second column we calculate $10^{0.076} = 1.19$. In the third column $10^{-0.35} = 0.44$ and $10^{0.35} = 2.23$. And the percentual value $\frac{(2.23-0.44)}{1.19} = 150\%$.

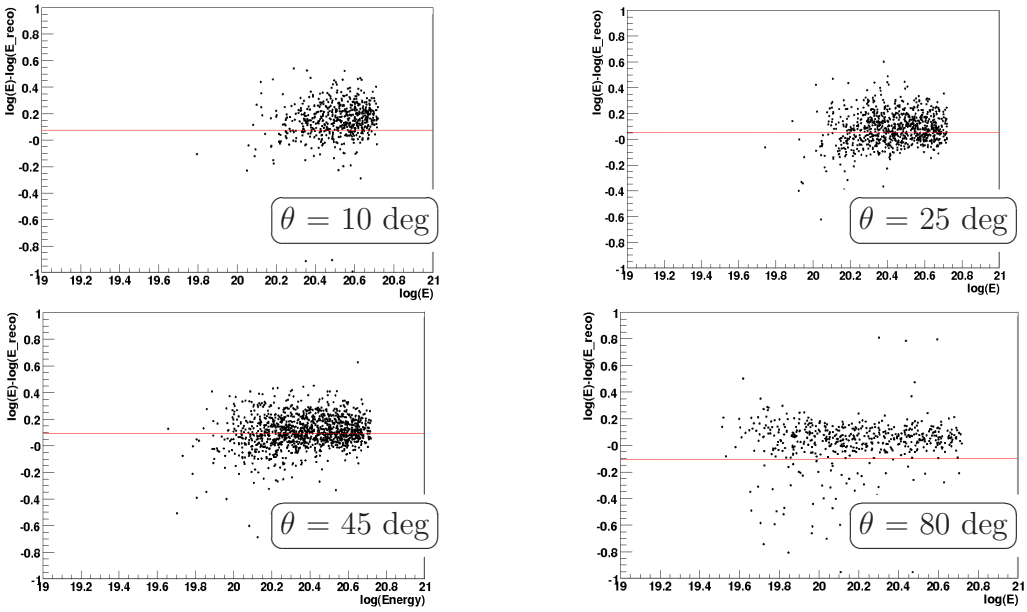

Figure 5.5: Reconstructed energy as function of the logarithm of primary energy. Red lines are mean values on the entire population. Results have been obtained with "Phase A EUSO Report" baseline configuration with background of 0.6 $\frac{photoel}{(pix*micsec)}$ (or 500 $\frac{photons}{(ns*sr*m^2)}$). It is observable by eye how for 10 and 80 deg the mean value is shifted compared to the population of events visible in this plot. This is due to the effect of the tails we showed in plots 5.4. We remember that those tails are out of the range of the plot but they still contribute to the average calculation.

that there should be a bug in the code. Further work is needed in order to

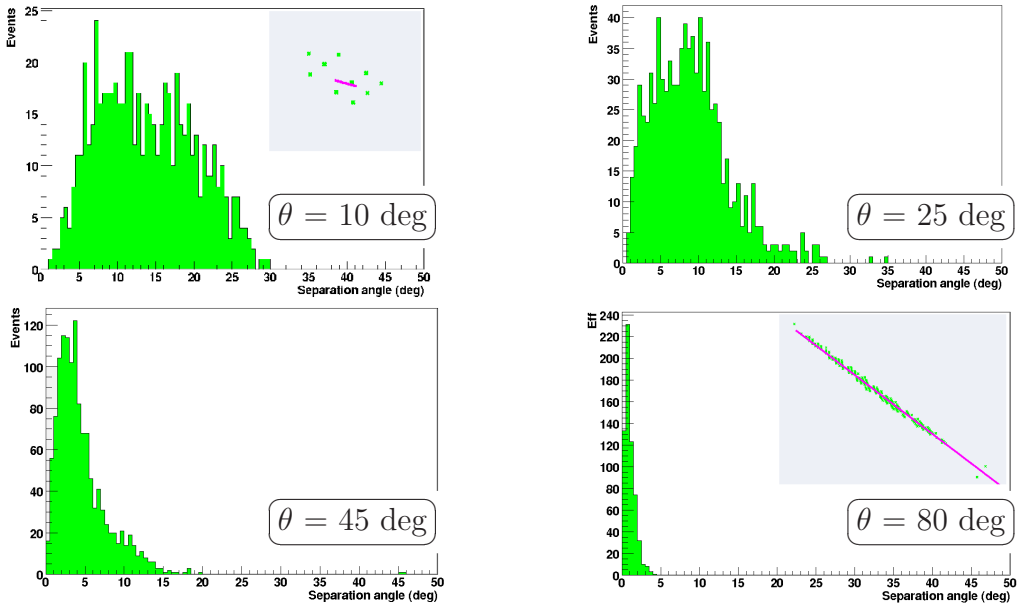

Figure 5.6: Separation angle real-reconstructed direction. Results have been obtained with "Phase A EUSO Report" baseline configuration with background of 0.6 $\frac{photoel}{(pix*micsec)}$ (or 500 $\frac{photons}{(ns*sr*m^2)}$).In the inserts we see the cluster of activated pixels of two showers for very different inclination angle.

solve it. Fortunately the error on those events is so big that they can be (for the moment) easily filtered.

In Fig. 5.5 the energy reconstruction quality as function of the primary energy is shown. We see, as expected, a strong dependence of the threshold from the angle. The higher the angle is the more points extend to lower energies.

We also estimated the separation angle [1] reconstruction (see Fig. 5.6).

Those events were always for four different angles with a power law energy spectrum with index -1. As before a better reconstruction is obtained for high inclination angle while at small theta the reconstruction is not working properly (see in table 5.3).

We make different plots for fixed energies: 6×10^{19}, 10^{20}, 3×10^{20} and 5×10^{20} eV.

[1]For separation angle we mean the angle in degree between the real and the reconstructed direction on the plain that contains both trajectories. The equation we used to calculate this angle is $\arccos(bc + de + a)$ whereas $a = \cos(\theta_{true})\cos(\theta_{reco})$, $b = \sin(\theta_{true})\sin(\theta_{reco})$, $c = \cos(\phi_{true})\cos(\phi_{reco})$, $d = /sin(\phi_{true})/sin(\phi_{reco})$ and $e = \sin(\theta_{true})\sin(\theta_{reco})$.

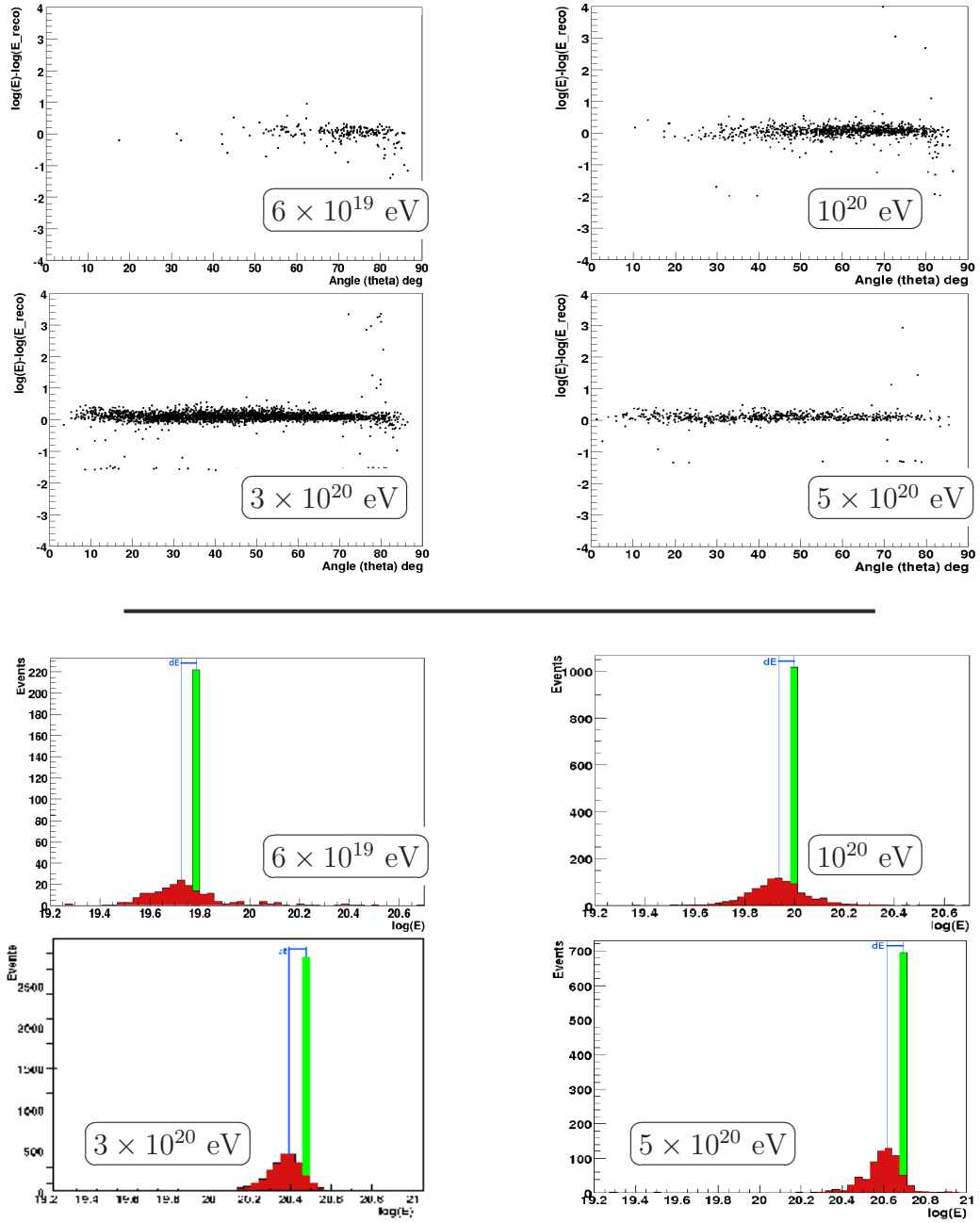

Figure 5.7: Upper panel: energy difference as function of the inclination angle. Lower panel: reconstructed energy compared with the real one. We observe in the lower panel a systematic effect of underestimation of the reconstructed energy. Blue lines have not been calculated but have just been obtained by observing the plots. In fact reading table 5.4 we see for example that for 10 deg the reconstructed energy is overestimated. This is not visible in plot. The average must be affected by some tail out of the range of the plot. Results have been obtained with "Phase A EUSO Report" baseline configuration with background of 0.6 $\frac{photoel}{(pix*micsec)}$ (or 500 $\frac{photons}{(ns*sr*m^2)}$).

Inclination angle (deg)	0.68 value in separation angle (deg)
10.5	17.25
25.5	10.75
45.5	5.25
80.5	1.25

Table 5.3: EUSO separation angle. The 0.68 value is tabulated.

In Fig. 5.7-upper panel we plotted the difference between real and reconstructed energy as function of the inclination angle. At higher energies also low angle events are visible. That's always because of the dependence of the energy threshold from the angle.

Primary energy (eV)	Average energy difference	RMS energy difference
6×10^{19}	-0.0575 (0.87)	0.44 (0.36-2.75) = 270 %
10^{20}	0.287 (1.94)	0.29 (0.51-1.95) = 74%
3×10^{20}	0.082 (1.2)	0.2 (0.63-1.58) = 79 %
5×10^{20}	0.0918 (1.23)	0.23 (0.59-1.7) = 90 %

Table 5.4: EUSO reconstruction data. Tabulated $Log(E_{real}) - Log(E_{reco})$. In parenthesis data expressed as ratios between real and reconstructed energy ($\frac{E_{real}}{E_{reco}}$). The RMS value is the range in which 68% of the events will fall. In the third column between parenthesis are two values $\frac{E_{real}}{E_{reco}}$ calculated by using the value RMS as exponent but with different sign. The percentual value is obtained by dividing the width of the range in third column by the ratio in second column. We give here an example for the first line. In the second column we calculate $10^{-0.0575} = 0.87$. In the third column $10^{-0.44} = 0.36$ and $10^{0.44} = 2.75$. And the percentual value $\frac{(2.75-0.36)}{0.87} = 270$ %.

Inclination angle (deg)	0.68 value in separation angle (deg)
6×10^{19}	2.25
10^{20}	3.25
3×10^{20}	5.5
5×10^{20}	5.75

Table 5.5: EUSO separation angle. The 0.68 value is tabulated.

In Fig. 5.7-lower panel we show a comparison between the real and the reconstructed energy. The reconstructed energy appears to be slightly underestimated. We read the mean value and the RMS value in table 5.4.

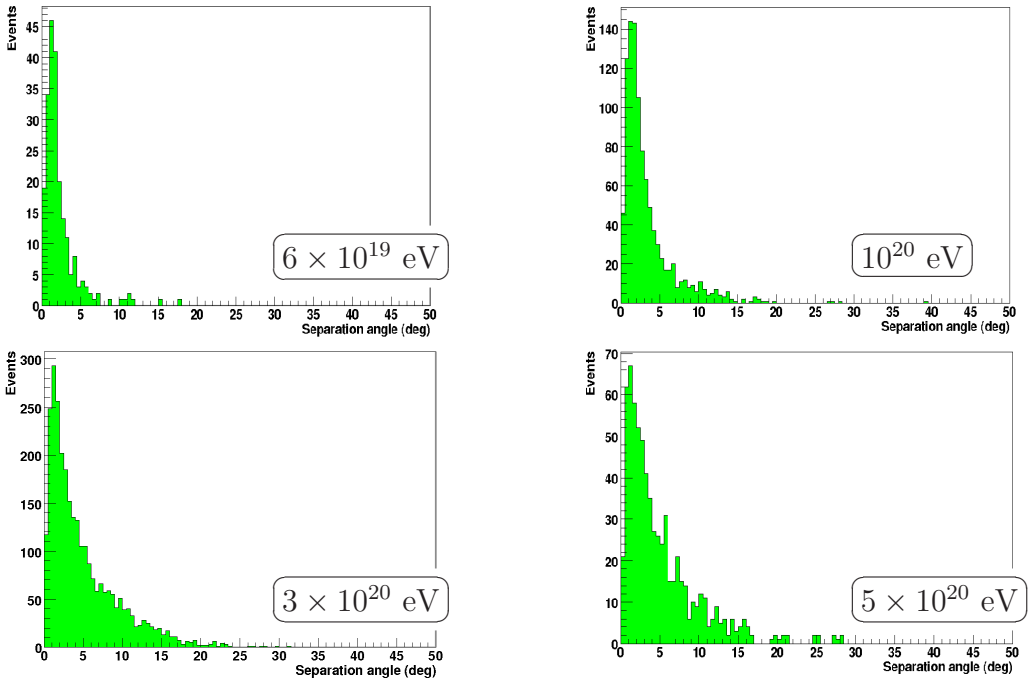

Figure 5.8: Separation angle. Results have been obtained with "Phase A EUSO Report" baseline configuration with background of 0.6 $\frac{photoel}{(pix*micsec)}$ (or 500 $\frac{photons}{(ns*sr*m^2)}$). We invite the reader to check in plot 5.9 to understand the puzzling result of a better anglular resolution for smaller energies.

In plot 5.8 the separation angle for different energies is shown. We see that for larger energies the distribution is broader. This result is confirmed from data in table 5.5. This suggests that the angular reconstruction is worst at higher energies. The answer to this apparently surprising result is in Fig. 5.9 where we show the dependence between separation angle and inclination angle. At higher energies also vertical events are detected and reconstructed with our direction reconstruction algorithm. However for those events there is a bad direction reconstruction. In fact as already explained there is a better angular reconstruction for horizontal showers. This will affect the statistic of plots 5.8 making the separation angle distribution for higher energies broader.

From our analysis a series of problems emerges in the reconstruction. The first one is the bad direction and energy reconstruction for vertical events. These are respectively due to the short tracks those showers generate and to the lack of points on which to perform the fits to find the shower profile. This would therefore require a careful design of the mission since low theta showers are not reconstructable neither in direction nor in energy. In fact

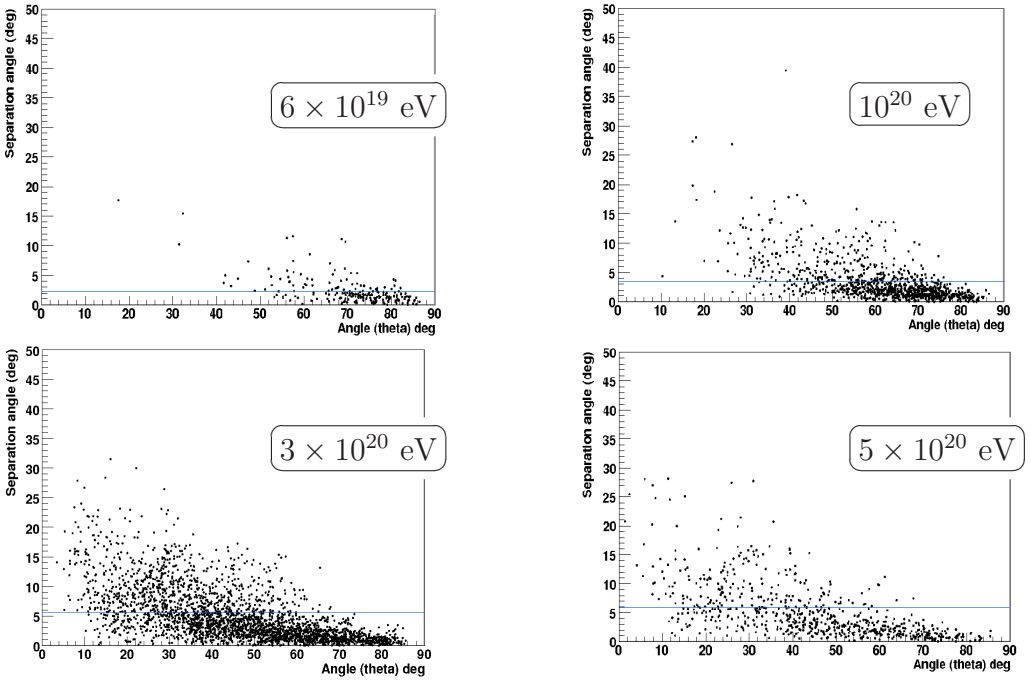

Figure 5.9: Separation angle as function of inclination angle. Results have been obtained with "Phase A EUSO Report" baseline configuration with background of 0.6 $\frac{photoel}{(pix*micsec)}$ (or 500 $\frac{photons}{(ns*sr*m^2)}$). The reason of the best angular resolution for small energies is clearly visible here. For smaller energies also very inclined showers are visible. For those events we have bad angular reconstruction. This affects the statistics of plot 5.8. Blue lines are the 0.68 values for the distribution of the separation angles.

higher trigger thresholds might exclude events that in any case won't be properly reconstructed.

The second problem is for very inclined showers. As we saw the energy reconstruction is not working for 10% of the events [2]. On this point we do not have at the moment any explanation. Probably further work on the software is needed in order to remove this bug.

What we recommend is to consider very inclined or low inclined showers always separately from the remaining statistics. Let's say that from the data we analysed that a range between 30 and 75 deg would deliever better results. Fortunately showers with extreme angles are a minority because of the distribution of events as function of the inclination. This is peaked to 45 deg (see Fig. 5.10).

The third issue is the underestimation of the reconstructed energy in all

[2]Considering a power law index -1 and this particular energy range.

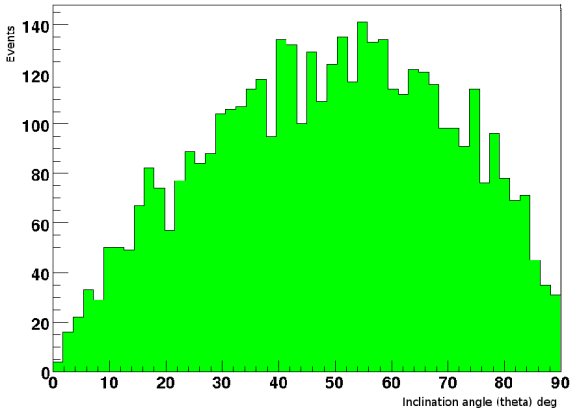

Figure 5.10: True primary particle inclination angle. The distribution is peaked around 45 deg for a geometrical reason.

the conditions. This is true even in the case where the average on the total population would say that there is an overestimation. In fact, in those cases the average of the reconstructed energy is shifted toward higher values by the not correctly reconstructed fraction of events. We invite the reader to look in all the plots where the energy reconstruction is evaluated. This feature is particularly apparent in plots 5.5 and 5.7-lower panel. This might have an origin on some wrong setting of the ESAF parameters. Further work is required to solve this problem.

5.2 JEM-EUSO studies

5.2.1 New trigger implementation

The second part of the thesis has been devoted to the implementation in ESAF of the configuration of the JEM-EUSO mission. This is critical to assess the performances of this newly designed mission.

At first we implemented a new kind of trigger algorithm: the *LinearTrackingTrigger* algorithm. The first evaluation of the capabilities of it was done using the old EUSO instrument configuration. More specifically we compared the performances of three triggers: the *LinearTrackingTrigger*, the *ChipTrackingTrigger* and the *LBL*.

In Fig. 5.11 we summarize the trigger efficiency with the EUSO configuration for three different algorithms. As we see the *LinearTrackingTrigger* performs better than the *ChipTrackingTrigger* considered in the ESA phase

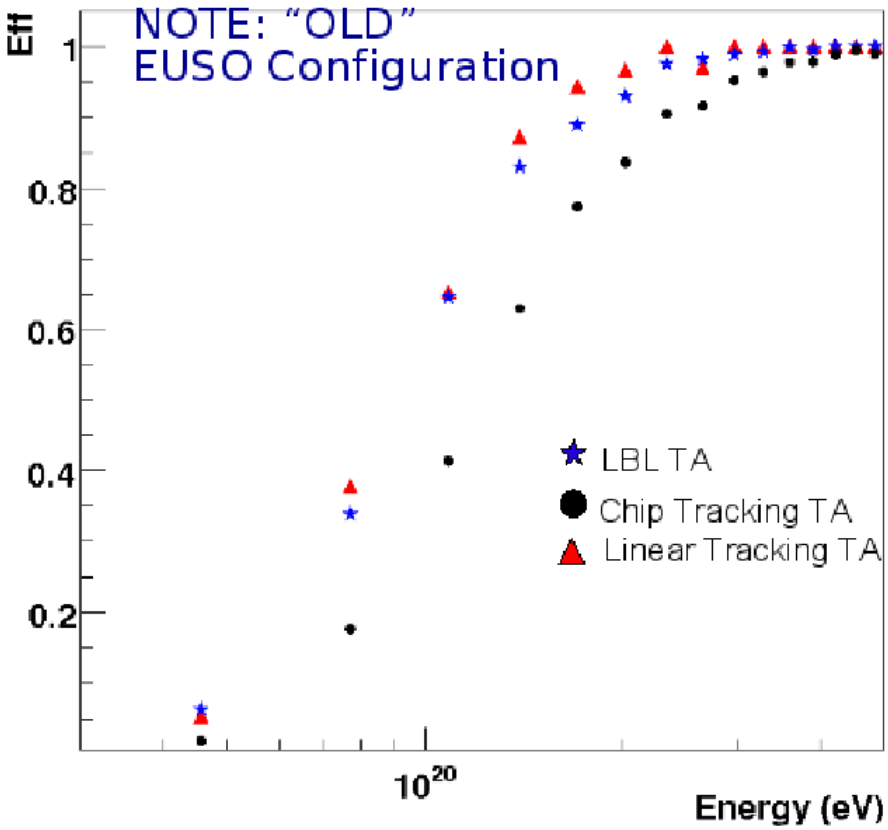

Figure 5.11: Trigger efficiency comparison between different algorithms. Results have been obtained with "Phase A EUSO Report" baseline configuration with a background of 0.6 $\frac{photoel}{(pix*micsec)}$ (or 500 $\frac{photons}{(ns*sr*m^2)}$).

A study. The relative improvement is of the order of 20%. The *LBL* provides comparable results. However no group is developing this algorithm at the moment. Therefore we suggest to use the *LinearTrackingTrigger* as a baseline for the JEM-EUSO instrument.

We also evaluated the performances and the differences between the trigger algorithms for fixed angles. We have chosen three inclination angles 10, 45 and 75 degrees for which we calculated the trigger efficiency as function of the energy (see respectively Fig. 5.12, 5.13 and 5.14). We stress that the comparison was done using the JEM-EUSO configuration described in section 5.2.2.

The LBL performs better for small inclinations while the Linear Tracking Trigger Algorithm (LTTA) is better for larger inclinations. This is because of the different principles of the algorithms. The LTTA is more performant

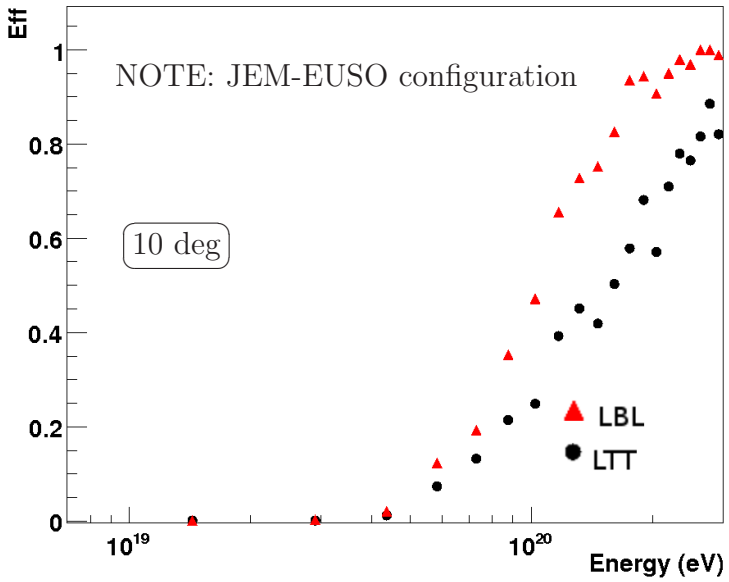

Figure 5.12: Trigger efficiency comparison between *LinearTrackingTrigger* and *LBL*. JEM-EUSO configuration.

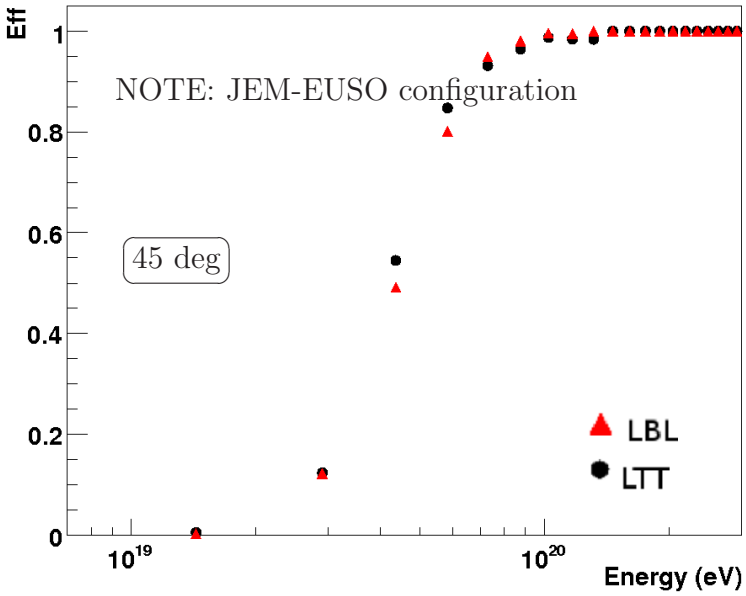

Figure 5.13: Trigger efficiency comparison between *LinearTrackingTrigger* and *LBL*.JEM-EUSO configuration.

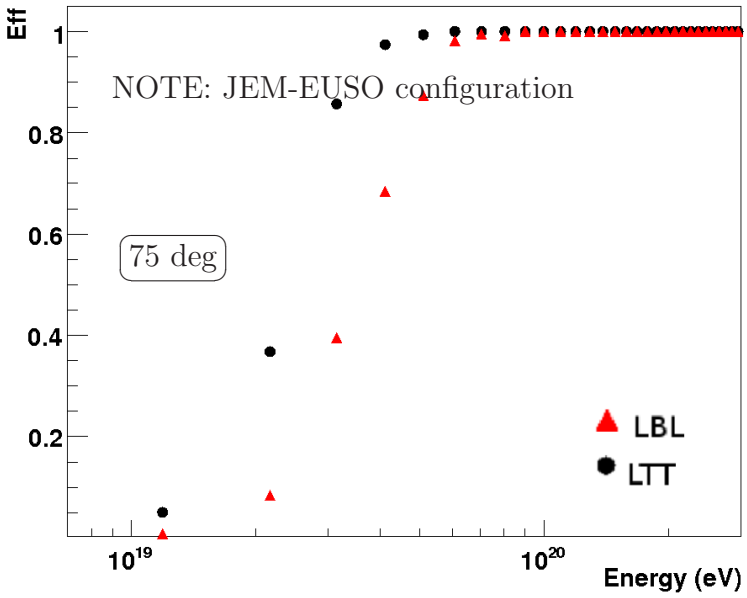

Figure 5.14: Trigger efficiency comparison between *LinearTrackingTrigger* and *LBL*. JEM-EUSO configuration.

in following spots moving for long tracks on the focal surface. In fact the integration box can move for many Gate Time Unit (GTU)s and in the end cover a really long path on the focal surface. LTTA can follow better inclined showers which are capable of generating long tracks on the focal surface. *LBL* on the contrary performs integrations moving just few steps. This is more suitable for those showers insisting a lot of time on the same pixels. Those are the really inclined showers. A reason for the better performances at low theta is that the *LBL* has more freedom in choosing the direction of the integration path. The LTTA on the contrary moves the integration box just in a limited set of directions.

We suggest to choose the LTTA because it gives better performances for events at the lower energies. At low energies we expect a higher flux compared to the one we would see with *LBL* at higher energy. Furthermore the direction reconstruction is for high theta much better.

Another reason to choose for the LTTA is the reasonable hope we have to further improve the algorithm while the LBL is not more under development. Several improvements are foreseen. The first step would be to go from the Elementary Cell (EC) level (at which the algorithm is now implemented) to the Photo Detection Module (PDM) level. Then we will introduce a threshold dependence on the background level (which should be radius dependent) in

the trigger algorithm. The idea is to calculate the map of the background on the focal surface and for each PDM decide a different set of thresholds.

Another important point would be the implementation of the Cluster Control Board trigger algorithm and of an algorithm based on the persistency to be put before the *TrackingTriggerAlgorithm*. Those changes could help to further lower the threshold.

5.2.2 JEM-EUSO implementation

To study the JEM-EUSO performances we implemented in ESAF a parametrization of its configuration. What we included in ESAF is:

1. The new optics parametrization.

2. The new focal surface layout.

3. We used the already present parametrization of the improved Hamamatsu R8900M-03-M36 detection efficiency.

As already explained in the previous chapter, in ESAF we use the so called *ParamOpticalSystem*. This allows us a fast implementation of the optics configuration. In fact to define a new optics we have just to know the throughput efficacy [3] and the point spread function [4] both as function of the incidence angle.

To calculate those characteristics we used a code to generate a number of photons passing through the JEM-EUSO optics. The code was provided to us by Riken. The point spread function has been fitted with a Gaussian function even if the real one is not symmetric. We show in Fig. 5.21 the output of the code for the generation of the optics in order to have an idea of the form of the photon distribution on the focal surface.

We used those coordinates to perform the fit in order to have an estimate of the point spread function. To fit the distribution of photons on the focal surface we used the equation $psf(x,y) = Ae^{\frac{(x-x_0)^2}{2\sigma_x^2}+\frac{(y-y_0)^2}{2\sigma_y^2}}$ in which $\sigma_x = \sigma_y$. In a two dimensional symmetric Gaussian distribution of events within the sigma will fall more or less 39% of the events. We simply calculated at which

[3] This is (as explained in chapter 4) an effective detector area "seen" by a photon coming with a certain inclination. This is obtained by multiplying the total optics pupil area with the cosinus of the entrance angle and the absorption coefficient.

[4] The Point Spread function is the spread in which the photons from a point-like source are distributed. In fact the optics is not perfectly refracting but the irregularities of the lenses will make photons scatter in different directions than the one obtainable from the laws of optics.

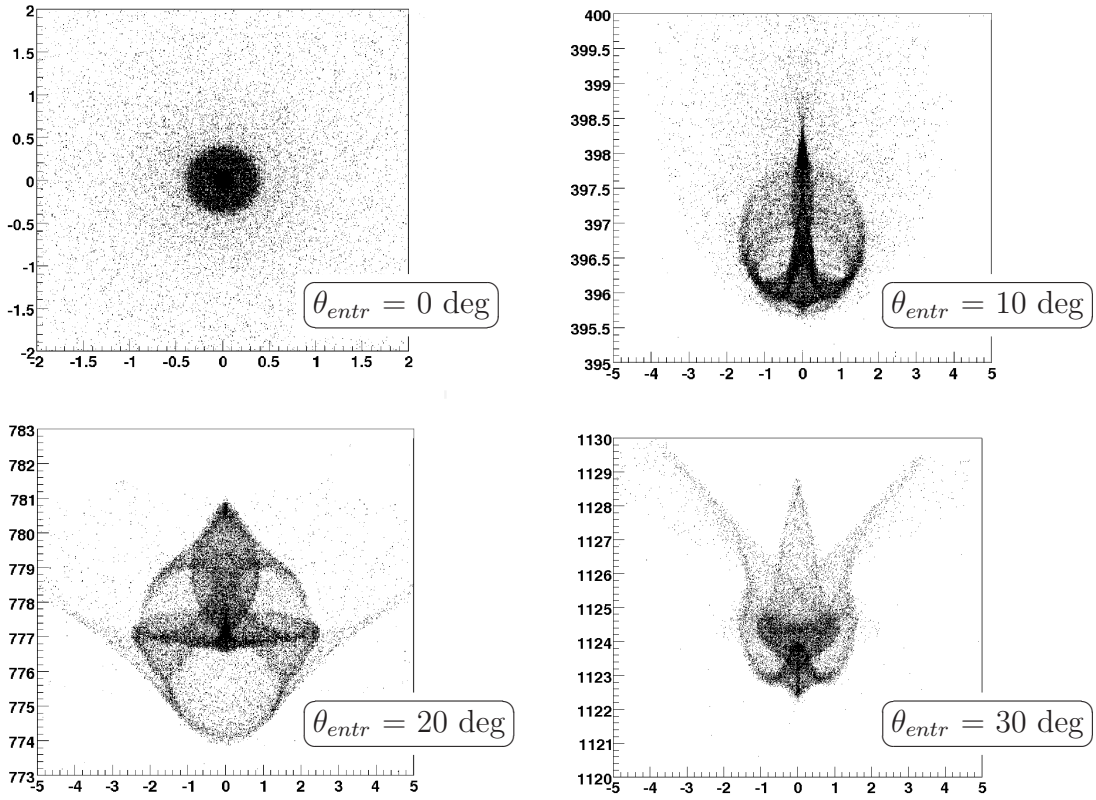

Figure 5.15: Point spread functions. In the axis are represented the positions of the photons in mm. Those point spread functions are obtained for entrance angles equal to 0,10,20,30 degrees (from up-left to bottom-right).

radius from the PSF center 39% of the events are contained. We setted this value as the σ of the PSF.

In Fig. 5.16 we compare the total efficacy of the optics for EUSO and JEM-EUSO. This is the effective area of the optical system. We will obtain it multiplying the area of the pupil by the cosinus of the entrance angle and by (1-the absorption coefficient). $Eff = A\cos\theta(1 - Abs)$.

In Fig. 5.17 we show the Point Spread Function (PSF) sigma as function of the angle. This is to assign a sigma value to the random scattering around the center of the PSF (see previous chapter). In Fig. 5.18 a parametrization of the fraction of the photons falling within a radius of 10 mm from the PSF center is shown. All those photons not falling within 10mm will be distributed on a large area and in the end they will be indistinguishable from background. In case the photon reaches the FS and it's still in the PSF it

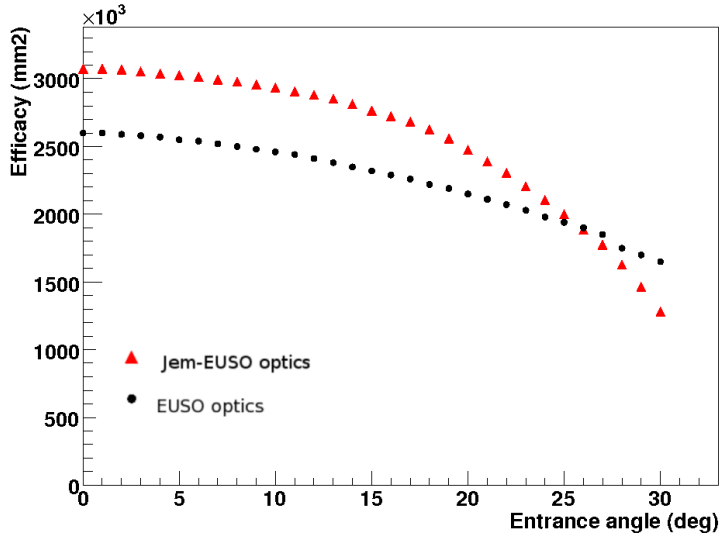

Figure 5.16: Total efficacy function of the optics.

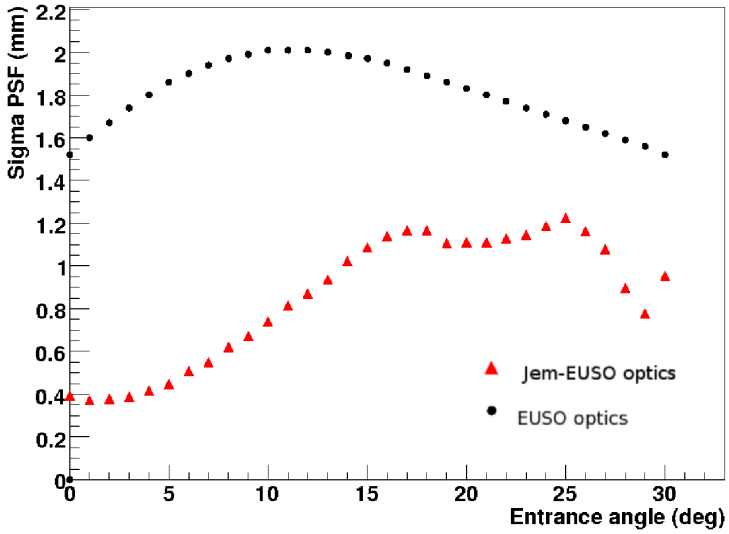

Figure 5.17: Sigma of the Point Spread Function of the optics.

will be distributed on the focal surface randomly with a Gaussian distribution having a sigma as given in the parametrization and a center as calculated in equation 4.1.

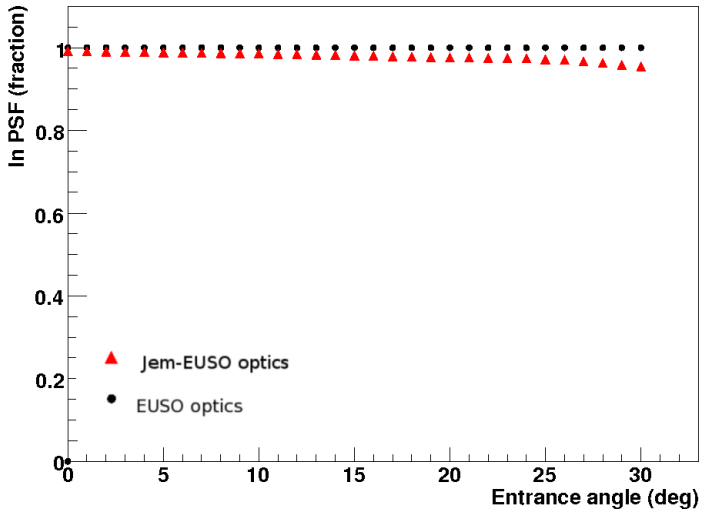

Figure 5.18: Fraction of photons in Point Spread Function.

We inserted also the parametrization of the focal surface provided by Riken. The position, normal and orientation of each element is required. We invite the reader to go to the previous chapter to look for more detailed informations on the focal surface. Due to the characteristics of the present configuration of the software we needed also to fit the z-positions of the elements on focal surface as function of the radius. We need this information in order to have the equation of the profile of the focal surface. We needed to change the code introducing the new equation for the focal surface profile. However this change has not totally solved the problem yet. Therefore we had to introduce a correction factor on the detection efficiency of the PMT in order to have a good estimate of the triggering efficiency of JEM-EUSO. In fact, in the EUSO focal surface all the PMTs were deployed separately on the focal surface. Therefore an equation describing the position of the PMTs would perfectly intersect the position of all the elements. Therefore photons will be always properly deployed in one specific PMT (see previous chapter for a more detailed explanation). In the new focal surface the PMTs are structured in PDMs. Those unities are square and each PMT is on a plane that contains other 36 PMTs. To describe the position of all the PMTs we would need an equation for each PDM. However in the current structure of ESAF to determine the position on the focal surface of each photon just one profile equation is required. That turns out with the fact that not all the PMTs are correctly described by a single function. The points on the plot radius-z are scattered around the curve which is fitting the profile. We

choose a nine degree profile equation to fit all the positions of the elements. This will result in a worst placement of the photons in the PMTs. In the end,due to this technical problem, we had that the efficiency curve is still 10% worst than in the case of the $\theta - \phi$ layout. At this point we could have done essentially two things: the first would have been to implement a new routine in order to distribute the photons in the focal surface. The other possibility is to correct this problem with a factor in the detector efficiency. We have chosen the second one for time reasons. We assumed that the new focal surface would give a 10% better efficiency than the older one. This is due to the better filling factor of the new focal surface which amounts to 10% more than the other one. In the end we added to the detection efficiency a 20% more in order to bring the focal surface curve where is expected to be. We also used a more conservative correction factor equal to 10% in order to have a range in which we safely parametrize the real curve.

The quantum efficiency of the photocatode of the PMT is shown in Fig. 5.19. In order to have a single value we should calculate an average on the values between 300 and 450 nm. This is the range in which *ShowerLightSource* is generating light. Then we will have to multiply the value resulting from the average with the collection efficiency. This is more or less of the order of 70% . The resulting number came out to be 0.269. This was considered to be the photodetection efficiency of our simulation. This is a first approximation that sets the efficiencies of all the PMTs to be the same.

In Fig. 5.20 the trigger efficiency of JEM-EUSO is compared with the one of EUSO. In black is the area where the EUSO efficiency curve could be. The red area is the one of JEM-EUSO. The delimiting curves are obtained with different background levels namely 0.3 and 0.6 photoelectrons/(μs*pix) for EUSO, 0.84 and 1.65 photoelectrons/(μs*pix) for JEM-EUSO. The delimiting curves are also obtained assuming an external background ($< B >$) of the order of 250 and 500 photons/(m^2*ns*sr) for both instruments. The number of background photoelectrons has been calculated in the following way:

$$\mu_{pix} =< B > A\Omega\epsilon\Delta t/N_{pix} \tag{5.1}$$

Where $< B >$ is the average external background flux, Ω is the solid angle seen by EUSO, ϵ is the rate between incident photons and photoelectrons, Δt is the time interval, A is the area of the pupil and N_{pix} is the number of pixels. The $\pm$ 30 deg EUSO Field Of View is equivalent to $\Omega = 0.85$ sr. A is more or less $4m^2$ and $N_{pix} \sim 2 \times 10^5$ as in the case of EUSO. The difference between EUSO and JEM-EUSO is expressed by ϵ. For the first instrument is assumed to be 0.07 for the second 0.19. Those efficiencies are roughly the efficiency of the optics multiplied with the efficiency of the photomultiliers.

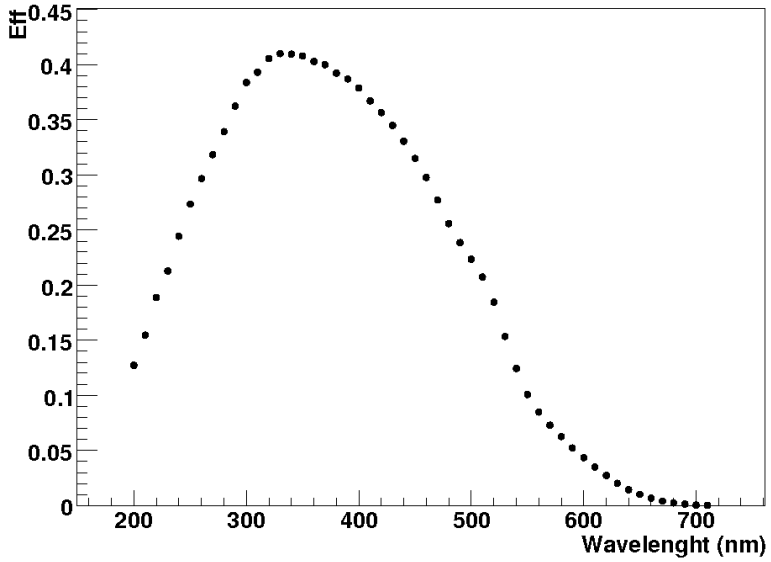

Figure 5.19: Photocatode quantum efficiency. Only values between 300 and 400 nm are relevant for JEM-EUSO.

This means that just 7% and 19% of the photons arriving at the pupil are producing photoelectrons. We also note that in the plot for JEM-EUSO the more optimistic curve has a 20% focal surface correction factor while the more pessimistic just 10%.

The efficiency curves delimiting the areas reach the half efficiency value (0.5) at 1.1×10^{20} and 8.5×10^{19} eV for EUSO. The half efficiency values will be 6.5×10^{19} and 4.5×10^{19} eV for JEM-EUSO. We calculated the mean value for both the instruments and we obtained 9.3×10^{19} eV for EUSO and 5.5×10^{19} eV for JEM-EUSO. We see that the ratio between the half efficiency of the two instruments is 1.69.

The obtained results are in good agreement with what we expected. In fact if we take into account an improvement of the optics of a factor 1.5 and 2 for the PMTs we will have a total improvement of the instrument of the order of 3 (1.5*2=3 $\sim \frac{\epsilon_{EUSO}}{\epsilon_{JEM-EUSO}} = \frac{0.19}{0.07}$). That means also that we will have a total improvement of a factor 1.7 of the ratio signal-background. That's because of the fact that we have 3 times more signal but also a factor $\sqrt{3} \simeq 1.7$ more fake trigger rate. That's an approximation and one should perform a calculation on the poissonian distribution of the background but

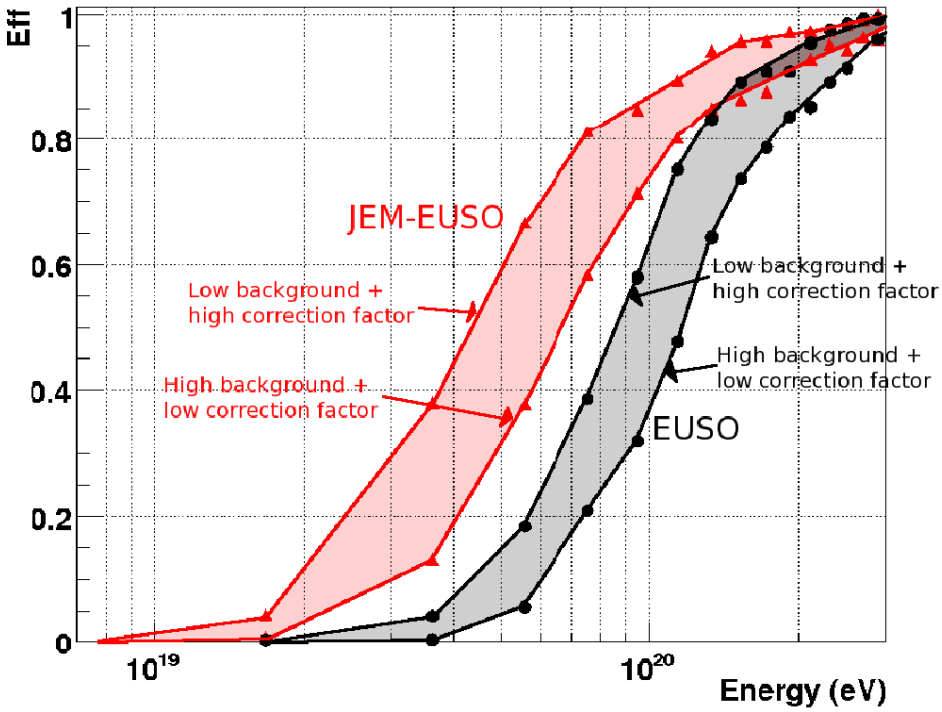

Figure 5.20: JEM-EUSO efficiency (red) compared with EUSO (black). The left curve for JEM-EUSO is obtained with a 0.84 photoelectrons/pixel/microsecond background + a factor 1.2 in the detection efficiency. The right curve for JEM-EUSO is obtained with a 1.65 photoelectrons/pixel/microsecond background + a factor 1.1 in the detection efficiency. The left curve for EUSO is obtained with a 0.31 photoelectrons/pixel/microsecond background. The right curve for EUSO is obtained with a 0.6 photoelectrons/pixel/microsecond background. The two levels of background are equal to 500 and 250 photons/ns/sr/m^2 for both the instruments. The conversion has been obtained with equation 5.1.

it still gives an idea of the larger oscillations of the background that are of the order of the square root of the average.

However there should be also the improvement due to the better focal surface filling factor. This factor should correspond to a factor 0.1 more in the thresholds ratio. The ratio between the half efficiencies should therefore be $\sim$ 1.8 and not 1.7 like the one we see. We can anyway say that this difference is smaller than the band width represented by the extreme curves.

In the end we have inserted also the efficiency plot as function of the energy and of the angle (see Fig. 5.21). The curve for JEM-EUSO is shifted to lower values. We see that for higher angles we still have a 100% efficiency for events with an energy of 4×10^{19} eV. This class of events (if this turns out to

be the real JEM-EUSO efficiency) could be used to calibrate the instrument reconstruction with data from ground arrays. Those arrays have a smaller exposure than space based observatories and for this reason they cannot detect a really high number of events above 10^{20} eV. A cross calibration would be really useful to reduce systematic effects.

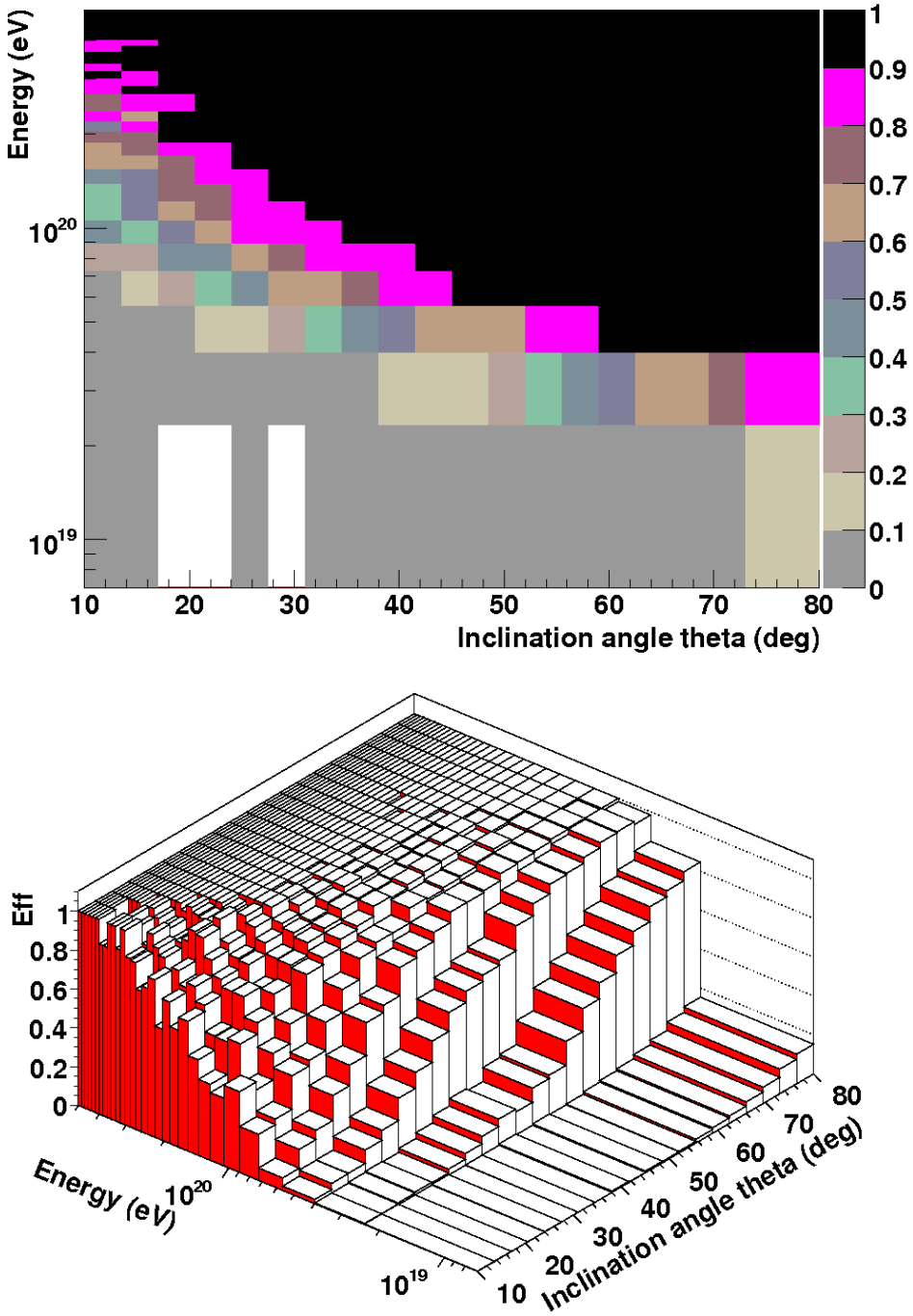

Figure 5.21: JEM-EUSO efficiency as function of energy and inclination angle.

5.2.3 A first assesment of S-EUSO performances

To conclude this thesis we also made a preliminary estimate of the performances of S-EUSO. At the moment we do not have a final configuration for S-EUSO so it has been implemented as overscaled version of JEM-EUSO. However we rely on the fact that this study shouldn't be much far from reality. That's essentially because we are using a parametrical optics and the only things we need to characterize the optics itself are throughput efficacy and spot dimension (see chapter 4 and section 5.2.2). Those data have been provided to us by A. Zuccaro of INOA in Firenze. In the throughput efficacy will also be included the obscuration effect of the focal surface. Other aspects like photomultiplier detection efficiency, height of the instrument from earth surface, dimension of the instrument,background level and Field Of View can be easily changed in ESAF. The focal surface layout was kept as the one of EUSO. The trigger algorithm used is the *LTTA*.

The only point that could be really critical at this stage is the dimension of the focal surface[5]. In fact the S-EUSO focal surface is larger and a change in the angular position of a shower will result in a larger change in linear position of the spot on the focal surface. Since the pixel size for S-EUSO is probably not going to change much with respect of JEM-EUSO, the signal will insist a shorter time on each pixel. Our simulated instrument is simply scaled and therefore also the pixel size is increased. The signal in our simulation will insist on each pixel always the same time as in the case of EUSO. The signal in our simulation is therefore probably slightly overestimated with respect to the real S-EUSO. We can say that the signal overestimation factor is probably proportional to the ratio of the dimension of the focal surfaces. We can therefore reasonably expect a signal overestimation factor between 1 and 2. This is a relatively small effect if compared to other changes brought by S-EUSO like those related to the increased area improved detection efficiency and orbit variation. Nevertheless we decided to insert the correction to the signal overestimation in the simulation. We simulated at first the instrument with the full efficient PMT (PDE=0.6) and than we introduced the more extreme correction factor namely 2. The PDE was set therefore equal to 0.3.

Always using the ESAF parametrizations routines we therefore changed:

1. Scale factor of the instrument

2. Photomultiplier detection efficiency

3. Optics parametrization

[5]We remember that S-EUSO Focal Surface will have 2 m radius while EUSO had 1.13m.

4. Field Of View

The scale factor has been set to 2.9. This will make the 2.3 m pupil JEM-EUSO to reach the 6.7 m diameter of S-EUSO. The Photomultiplier detection efficiency has been set to 0.6 and the Field Of View to ± 25 deg. In Fig. 5.22 and 5.25 the optics parametrizations we used are shown. For the meaning of these plots we invite the reader to look in section 5.2.2.

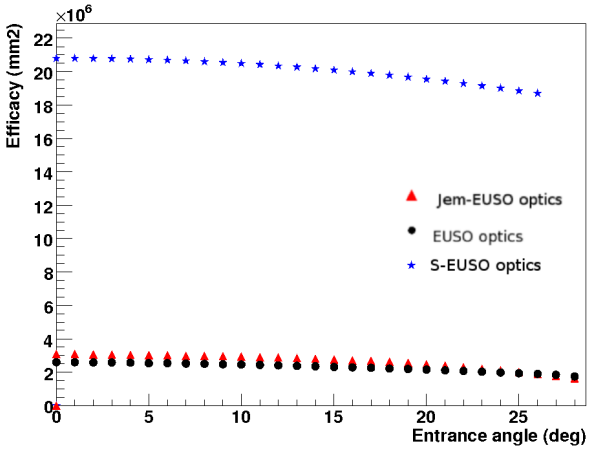

Figure 5.22: The S-EUSO optics total efficacy.

In Fig. 5.24 we show the efficiency plot of S-EUSO. In green we represent S-EUSO at an height of 430 km. In blue S-EUSO at 1200 km. The extremes for the two areas are obtained with two background levels. The first one is equal to 3.5 and the second to 5.1 photoelectrons/(μs*pix). This corresponds to the external background levels of 340 and 500 photons/(m^2*ns*sr). The conversion has been obtained using formula 5.1 with an $\Omega = 0.58$sr, a pupil area of 35.2 m^2 and 3 times more pixels than EUSO ($\sim 6 \times 10^5$) [6]. The ϵ has been calculated assuming a PDE of 0.6 and an efficiency of the optics $\sim$ 0.5. We used $\epsilon \sim 0.3$. The delimiting curves on the right are also corrected with the factor 2 due to the signal overestimation correction factor.

In Fig. 5.24 we see the efficiency curves for S-EUSO. The extreme values of the half efficiency for the 430 km curve are 5×10^{18} and 1.1×10^{19} eV. This corresponds to an average of 8.25×10^{18} eV. The extreme values of the

[6]We remember that the area of the focal surface of S-EUSO is more or less 3 times grater than the one of JEM-EUSO. Furthermore we expect a similar pixel size.

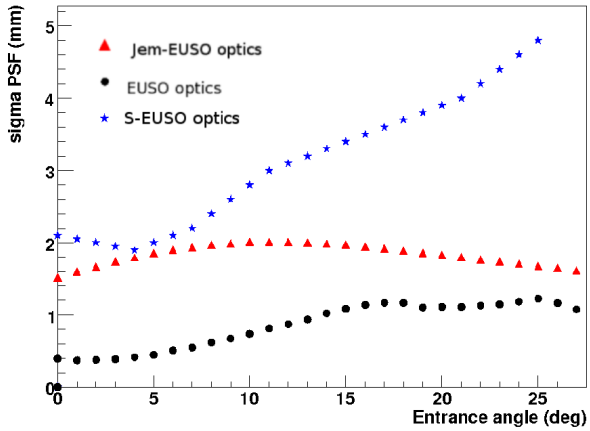

Figure 5.23: The S-EUSO optics spot sigma.

half efficiency for the 1200 km curve are 2.5×10^{19} and 5.5×10^{19} eV. This corresponds to an average of 4×10^{19} eV.

The first thing we can say is the fact that the ratio between the averages of the two efficiencies is more or less 6. This is a little bit less than the expected ratio which should be 7.8. This is simply assuming that the difference in the signal is of the order of the square of the differences in the height. In fact $(\frac{1200}{430})^2 = 7.8$. Further study is needed to understand this difference.

We see in the end how adjusting the height by a factor 3 could shift the threshold by one order of magnitude allowing to cover a really large rage in energy. The decision of the orbit is also a crucial aspect in order to design the mission. Further study is needed also in order to decide at which height to put the instrument.

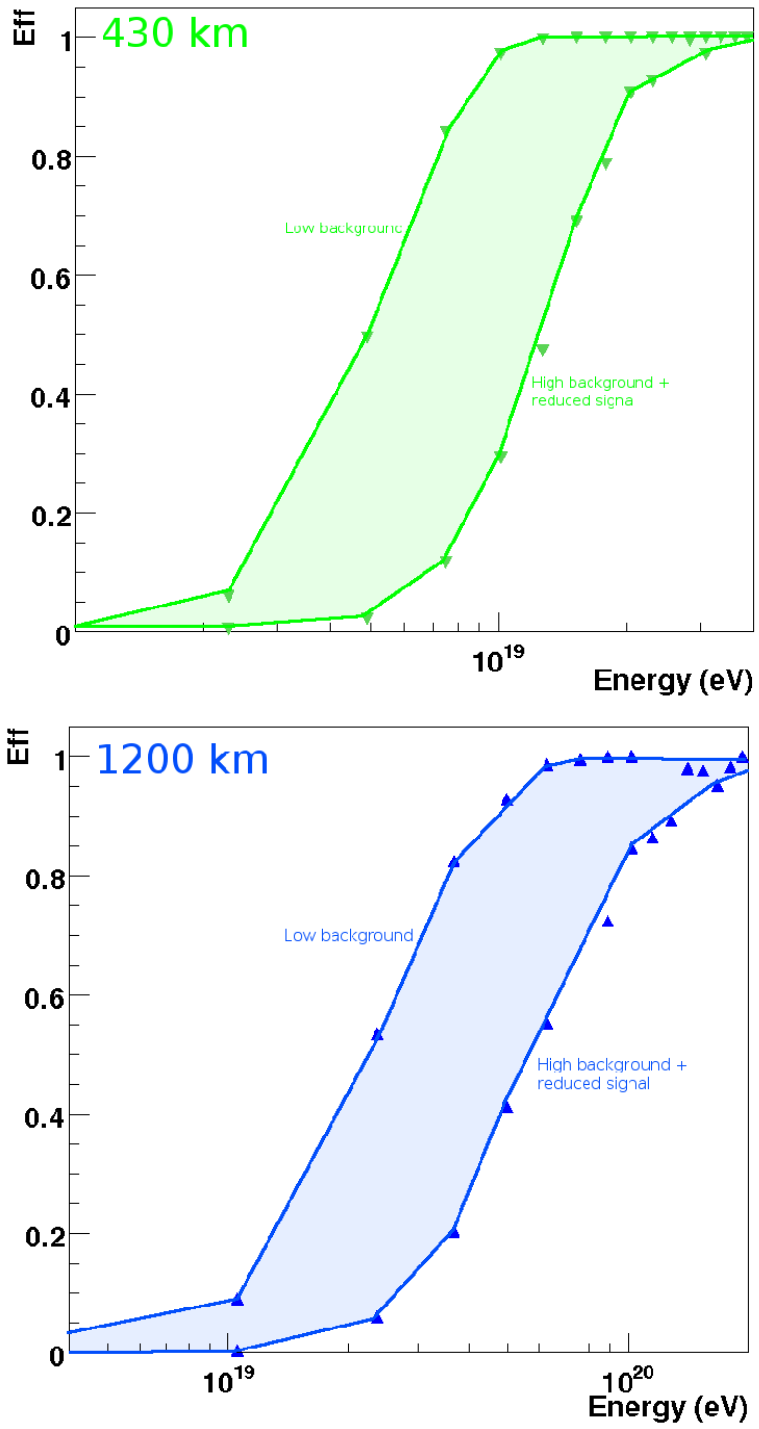

Figure 5.24: S-EUSO efficiency plots at 430 and 1200 km height. The extreme cases at both heights have been obtained with a background of 340 and 500 photons/(m^2*ns*sr). The conversion between this flux and the rate par pixel is obtained with 5.1. The extreme cases are also obtained with a correction factor due to focal surface differences equal to 1 and 0.5.

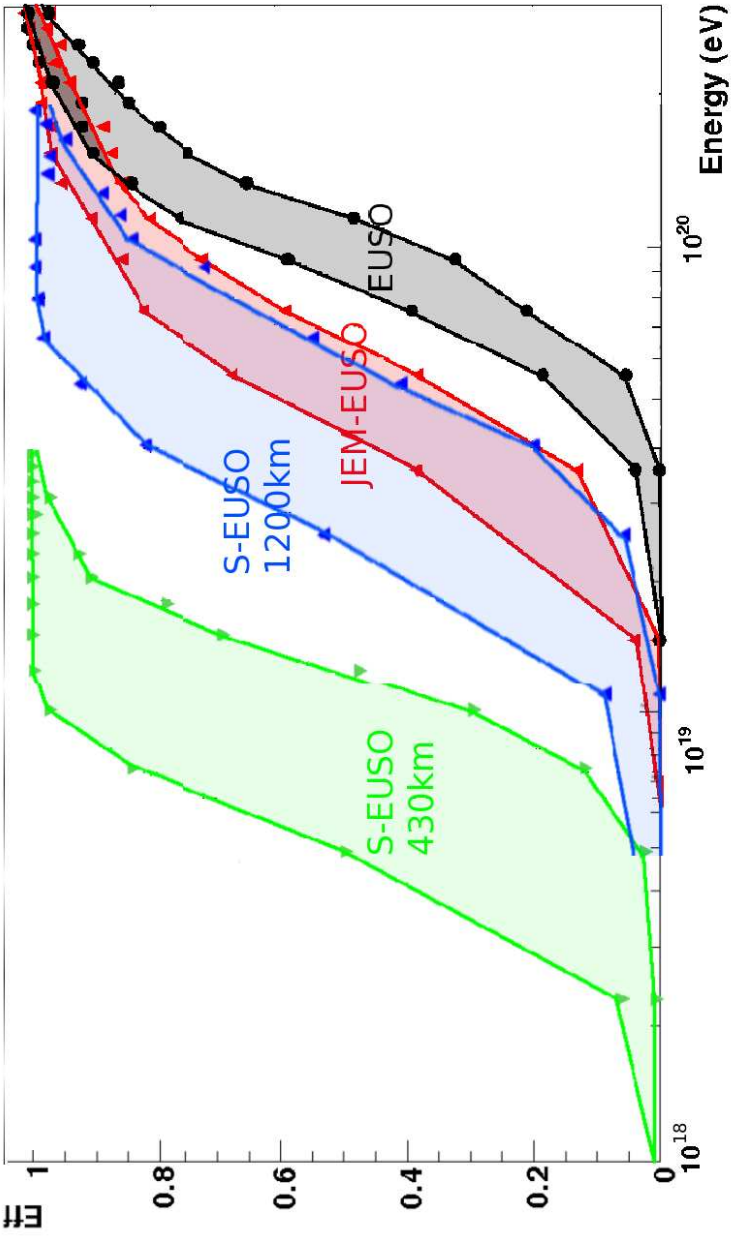

Figure 5.25: Comparison between the three instruments. EUSO, JEM-EUSO, S-EUSO(1200km) and S-EUSO (430km). This is the graphical superposition of the plots 5.24 and 5.20.

Conclusions

Aim of this thesis was the study of the expected capabilities of different configurations of space based observatories for Ultra High Energy Cosmic Ray research. In what follows we very briefly summarize the results obtained and we comment on them.

After reactivating the ESAF code, the first step was to validate the ESAF package itself as implemented at IAAT, reproducing the results for the EUSO mission as reported in the EUSO "Red book", which summarizes the ESA Phase A Study of the mission. The trigger efficiency obtained by us nicely overlaps with the curves of the Report, both reaching the half efficiency value in the proximity of 10^{20} eV.

Moreover, still using the EUSO configuration, we have obtained some new results with respect to those presented in the "Red Book". First, we have calculated the detection efficiency as function of energy and angle. Then, for the EUSO configuration, we have characterized the reconstruction algorithms. We have studied the reconstruction for particles as a function of inclination angles and as a function of the energy. This has demonstrated the capabilities of the EUSO reconstruction and allows a preliminary estimation of the angular and energy resolution of EUSO.

We have also devoted part of the work on the comparison between different trigger algorithms. First the recently developed *LinearTrackingTrigger* algorithm (LTTA) was implemented in the ESAF code. Then, we performed a comparison between the LTTA and other trigger algorithms implemented for the EUSO phase A study, calculating the overall trigger efficiency. Other studies on the trigger were done in order to evaluate the performances at different angles. Based on our results, the LTTA, implemented by us, has resulted to offer the best performances. Also on the base of our studies, the LTTA is going to be the baseline for the JEM-EUSO instrument.

As a second major part of the research work, we have implemented the JEM-EUSO instrument in the end-to-end simulation code. This is an entirely new development of the ESAF package. More specifically, a new parametrization of the optics, of the photomultipliers and of the focal surface

layout have been implemented. Based on this new JEM-EUSO configuration, we have evaluated the trigger efficiency curves of the mission. According to our studies, the half efficiency threshold for JEM-EUSO (summing the improvements of LTTA, optics efficacy, PMT efficiency and layout) results to be shifted to lower energies by a factor 1.7 with respect to the EUSO one. Studies were done for different background fluxes. We have shown efficiency plots including more optimistic and more conservative assumption for background and systematic uncertainties of the implementation. The results closely match expectation. A deeper study of the efficiency as function of the energy and angle has been also performed.

The third part of the work has been devoted to a preliminary assessment of the S-EUSO instrument. This part has to be considered carefully since there is not yet a final S-EUSO configuration and different options are considered. We have therefore simulated for S-EUSO a JEM-EUSO-like instrument scaled to a greater radius, with an improved photomultiplier efficiency, a reduced field of view, variable orbit and a parametrization of the optics like the one of S-EUSO. We also had to insert a correction factor in order to take into account differences in the focal surface structure. Trigger Efficiency curves have then been estimated. Results are obtained for two different orbit heights (430 and 1200 km). In each of those orbits we consider a range delimited by the the more optimistic and more pessimistic situation for background and correction factor. Our results again matched expectations.

In conclusion we have demonstrated that the ESAF code is a powerful tool to test performances of different configurations of space missions for Ultra High Energy Cosmic Ray search. Our results on JEM-EUSO, presented, at several collaboration meetings, are being used by the JEM-EUSO collaboration to define and optimize the baseline of the instrument. In the future, it is also expected that the S-EUSO collaboration will use the ESAF tool.

To conclude our work we wish to give here some suggestion on possible future developments. In order to make a more reliable assessment of the instruments we recommend to move to a Montecarlo optics simulation. We used till now a parametrization for time reasons. The use of a more detailed parametrization for the photomultipliers (already present in ESAF) is also required.

The trigger algorithm can be improved, implementing the LTTA at PDM level. The dependency of the trigger thresholds from the background rate is also a crucial aspect that could be implemented. The thresholds should also be different for each PDM depending on the position on the focal surface. A trigger algorithm based on persistency has to be introduced before the LTTA. Also the Cluster Control Board trigger is a really promising improvement.

A key future step, is also the implementation of the reconstruction algo-

rithms for JEM-EUSO and S-EUSO. This will allow us a deep scientific understanding of the performances in terms of high quality events, analysis cuts to be applied and discrimination between different primaries.

Together with the implementation of the physical analysis, reconstruction will then allow studies of observable fluxes of particles, anisotropies, and composition, helping us to definitely define the science case of UHECR search from space.

Conclusioni

Scopo della presente tesi è il dare una stima delle potenzialità di diverse configurazioni di un osservatorio nello spazio per l'indagine di raggi cosmici.

Come già spiegato, il primo passo (dopo aver riattivato il software ESAF) è stato il riprodurre i risultati del Report di Fase A di EUSO. Questo è stato al fine di dimostrare le capacità del software. Abbiamo iniziato con la riproduzione delle curve di efficienza di trigger. Le nostre curve riproducono quelle del Report di Fase A.

Sempre nell'ambito della simulazione di EUSO abbiamo aggiunto anche qualche risultato a quelli già presenti nel Red Book. Infatti una simulazione dell'efficienza come funzione dell'angolo e dell'energia e' stata eseguita. Anche uno studio sull'algoritmo di ricostruzione è stato eseguito. A questo proposito abbiamo presentato due serie di grafici: nella prima fissando gli angoli di inclinazione e nella seconda l'energia della primaria. Questo ha dimostrato le capacità del software di ricostruzione e ci ha permesso di dare una stima preliminare della risoluzione in energia e angolare del software.

Abbiamo inoltre effettuato uno studio sugli algoritmi di trigger. A tal fine abbiamo implementato l'algoritmo *LinearTrackingTrigger*. Successivamente abbiamo effettuato un paragone delle efficienze di trigger come funzione dell' energia su vari algoritmi usando la configurazione dello strumento EUSO. Abbiamo inoltre eseguito uno studio sui vari algoritmi di trigger in varie condizioni di angolo di ingresso della particella primaria. A partire dai nostri risultati il *LinearTrackingTrigger* è risultato essere il migliore algoritmo fra quelli da noi considerati. Anche sulla base dei nostri studi l'LTTA verrà scelto molto probabilmente come baseline per JEM-EUSO.

Abbiamo successivamente implementato nel software una parametrizzazione dello strumento JEM-EUSO. A tal fine abbiamo implementato una parametrizzazione dell'ottica, dell' efficienza del fotomoltiplicatore e della disposizione degli elementi della superficie focale. Abbiamo stimato la curva di efficienza di JEM-EUSO e una comparazione con quella di EUSO è effettuata nella tesi. Abbiamo eseguito le simulazioni facendo assunzioni più o meno restrittive su background e altri fattori sistematici. Sommando tutti i miglio-

ramenti rispetto a EUSO (ottica,fotomoltiplicatori, disposizione della superficie focale e aggiunta dell'LTTA) la curva di JEM-EUSO risulta essere migliore di quella di EUSO dell'ordine di un fattore 1.7. Questo e' in buon accordo con quanto atteso. Abbiamo inoltre rappresentato a grafico l'efficienza di JEM-EUSO come funzione dell'angolo e dell'energia.

Infine abbiamo tentato una stima preliminare dell'efficienza dello strumento S-EUSO. Questi risultati andrebbero tuttavia trattati con la dovuta cautela in quanto nessuna specifica simulazione per S-EUSO è stata eseguita. Si tratta infatti di una versione scalata di JEM-EUSO in cui l'efficienza del fotomoltiplicatore è aumentata, l'ottica riproduce le caratteristiche di quella di S-EUSO, la quota è considerata variabile tra 430 e 1200 km e il raggio dello strumento è anch'esso aumentato. Anche in questo caso le simulazioni sono state eseguite facendo assunzioni più o meno restrittive su background e altri fattori sistematici. Anche qui i risultati ottenuti sono in buon accordo con quanto atteso.

Nella presente tesi abbiamo dimostrato le potenzialità del software ESAF nell'ambito dello studio e pianificazione di osservatori di raggi cosmici nello spazio. I nostri risultati sono stati presentati nell'ambito dei meeting delle collaborazioni JEM-EUSO e S-EUSO e sono stati utilizzati per l'ottimizzazione e lo studio di questi due osservatori. Il lavoro da noi presentato rimane inoltre aperto per molti futuri sviluppi e miglioramenti.

Zusammenfassung

Ziel dieser Diplomarbeit ist das Potential eines Weltraumgestützten Observatoriums für Kosmische Strahlung abzuschätzen. Damit benutzen wir die ESAF Software.

Wie schon erklärt haben wir als erstes die Ergebnisse vom "Report of Phase A Study" von EUSO reproduziert. Wir haben angefangen mit der Studie der Effizienzkurve von EUSO. Unsere Versuch war erfolgreich. Unsere Ergebnisse reproduzieren die Kurven aus dem Report.

Im Rahmen der EUSO Simulationen haben wir auch andere Ergebnisse produziert die nicht im "Red Book" vorhanden waren. Die Effizienzkurve als Funktion des Winkels und der Energie ist in der Diplomarbeit aufgetragen.

Außerdem haben wir den Rekonstruktion Algorithmus getestet. Im unserer Arbeit haben wir zwei Serien von Plots gemacht. In der Erste haben wir die Rekonstruktion für festen Teilchen Einfallswinkel simuliert. In der zweite die Rekonstruktion für feste teilchen Energie wurde durchgeführt. Das wurde gemacht um die Eigenschaften des Rekonstruktionssoftwares zu zeigen und um eine preliminäre Schätzung von der Energie und Winkel Auflösung des Instrumentes zu berechnen. Auch dieses Studium kann für erfolgreich abgeschlossen gehalten werden.

Wir haben einen neuen Triggeralgorithmus implementiert nämlich den *LinearTrackingTrigger*. Wir haben erstmal einen Vergleich zwischen den Effizienzkurven verschiedener Algorithmen für EUSO gemacht. Eine Studie über die Eigenschaften der Algorithmen für verschiedene Primärteilchens Einfallswinkel wurde durchgeführt. Wir haben festgestellt dass unsere Trigger die besten Ergebnisse liefert. Es wird wahrscheinlich als "baseline" für das JEM-EUSO Instrument gewählt.

Dann haben wir die JEM-EUSO Parametrisierungen eingeführt. Das heißt Optik, Photomultiplier und Focalfläche Layout Parametrisierung. Wir haben eine Effizienzkurve für Jem-EUSO produziert und mit der Kurve von EUSO verglichen. Durch die Addierung von allen den Verbesserungen ist die JEM-EUSO Kurve einen Faktor 1.7 besser als diejenige von EUSO. Dies stimmt mit unseren Erwartungen überein. Die Simulationen wurden für

verschiedene Hintergründe und Korrekturfaktoren für aufgetretene Systematische Fehlern durchgef"uhrt. Die Effizienzkurve als Funktion des Winkels und Energie ist in der Diplomarbeit auch für JEM-EUSO aufgetragen.

Letztendlich haben wir eine grobe Einschätzung für die S-EUSO Effizienzkurve gemacht. Diese Ergebnisse sollten sorgfältig behandelt werden da es um keine detaillierte S-EUSO Simulation sondern nur um eine skalierte Jem-EUSO Studie handelt. Wir haben die S-EUSO Optik, Photomultiplier, Layout Parametrisierung eingefügt. Die Höhe wurde als variabel zwischen 430 und 1200 km behandelt. Die Simulationen wurden für verschiedene Hintergründe und Korrekturfaktoren für aufgetretene Systematische Fehlern durchgeführt. Auch hier stimmen die Ergebnisse dem überein was wir erwartet hätten.

Im dieser Diplomarbeit haben wir das Potential von der ESAF software im Rahmen einer Studie und Planung einer Weltraumgestützten Observatoriums für Kosmische Strahlung gezeigt. Unsere Ergebnisse wurden in den JEM-EUSO und S-EUSO Kollaborationen Meetinigs benutzt. Außerdem unsere Ergebnisse werden für die Studie und Optimierung diese Observatorien verwendet.

Acronyms

AGASA Akeno Giant Air Shower Array

AGN Active Galactic Nuclei

ASIC Application Specific Integrated Circuit

CCB Cluster Control Board

CORSIKA COsmic Ray SImulation for KAscade

CR Cosmic Ray

CMB Cosmic Microwave Background

DSP Digital Signal Processor

EAS Extended Air Showers

EC Elementary Cell

EM ElectroMagnetic

ESA European Space Agency

ESAF Euso Simulation & Analysis Framework

EUSO Extreme Universe Space Observatory

FEE Front End Electronics

FOV Field Of View

FPGA Field Programmable Gate Array

FS Focal Surface

FTR Fake Trigger Rate

FZK ForschungsZentrum Karlsruhe

GRB Gamma Ray Burst

GTU Gate Time Unit

GZK Greisen Zatsepin Kuzmin

HiRes High Resolution Fly's Eye

INFN Istituto Nazionale di Fisica Nucleare

ISM InterStellar Medium

IR InfraRed

JEM Japanese Experimental Module

JEM-EUSO Extreme Universe Space Observatory on the Japanese Experimental Module

KASCADE KArlsruhe Shower Core Array DEtector

LIDAR Light Detection And Ranging

LOFAR LOw Frequency ARray

LOWTRAN LOW-resolution TRANsmittance

LOPES Lofar Prototype Station

LTTA Linear Tracking Trigger Algorithm

MPU MicroProcessor Unit

NS Neutron Star

OOP Object Oriented Programming

OWL Orbiting Wide-angle Light-collectors

PAO Pierre Auger Observatory

PDE Photo Detection Efficiency

PDM Photo Detection Module

PMMA PolyMethyl MethAcrylate

PMT Photomultiplier

PSF Point Spread Function

ROC ReadOut and Control

S-EUSO Super Extreme Universe Space Observatory

Si-PMT Silicon Photomultiplier

SLAST Shower Light Attenuated to the Space Telescope

SN Supernova

SNR Supernova Remnant

UHECR Ultra High Energy Cosmic Ray

UHE-Neutrino Ultra High Energy Neutrino

UV UltraViolet

Bibliography

[1] Cosmic rays / by A. M. Hillas. - Oxford : Pergamon Pr., 1972.

[2] Physikalische Zeitschrift, 10th year, no. 5, pages 152-157

[3] V.F. Hess. Phys. Z. 13 (1912), p. 1084

[4] M. S. Longair, High Energy Astrophysics v1, pp 1-31

[5] Y. Sekido H. Helliot (1985), Early history of cosmic ray studies

[6] W. Bothe , W. Kolhorster, Das Wesen der Hoehenstrahlung, Z. Phys. 56 (1929) 751

[7] P. Auger, R. Maze, T. Grivet-Meyer, Comptes Rendus 206, 1721 (1938)

[8] P. Auger, P. Ehrenfest, R. Maze, J. Daudin, Robley, and A. Fron, Rev. Mod. Phys.11, 288 (1939)

[9] J. Linsley, Phys. Rev. Lett. 10, 4 (1963).

[10] J. Linsley, L. Scarsi, B. Rossi, "Energy spectrum and structure of large air showers" , J. Phys. Soc. Japan (supp. A-III) 17, 91 (1962)

[11] J. Clay, P. M. Van Alphen, C. G. T. Hooft, Physica 1, 829 (1934)

[12] Phys. Rev. 45, 212 - 214 (1934)

[13] Tennent , Proc. Phys. Soc., 1967, 92

[14] H. R. Allan, Proc. Phys. Soc., Vol. 76 Part 1, n. 487 (1 july 1960)

[15] http://hires.physics.utah.edu/reading/flyseye.html#SEC10

[16] Baltrusaitis R. M. et al., Nucl. Instrum. Methods Phys. Res., Sect. A, Vol. A240, No. 2, p. 410 - 428

[17] S. C. Corbato et al., Nucl. Phys. B (Proc. Suppl.) 28B, 36 (1992)

[18] B. N. Srivastava and I.M. Mirza Phys. Rev. 176 (1968) 137

[19] J.T. Fons et al. Phys. Rev. A53 (1996) 2239

[20] A Measurement of the Fluorescence Efficiency of Air, F.Kakimoto, E.C. Loh, M. Nagano, H. Okuno, M.Teshima and T.Ueno

[21] L. Fülöp, T. Biró, Int. Journ. Theor. Phys, V. 31 N. 1, 1992

[22] N. Chiba et al. Nucl. Instr. & Meth. A 311 (1992), p. 338

[23] M. Teshima et al. Nucl. Instr. & Meth. A 247 (1986), p. 399

[24] Nuclear Physics B - Proceedings Supplements Volume 85, Issues 1-3, May 2000, Pages 324-331

[25] AUGER COLLABORATION, "Properties and Performance of the Prototype Instrument for the Pierre Auger Observatory", Nuclear Instruments and Methods, A523 (2004), 50.

[26] J. J. Beatty [AUGER Collaboration], Int. J. Mod. Phys. A 16S1C (2001) 1022.

[27] J. A. Simpson, Annu. Rev. Nucl. Part. Sci. 33, 323 (1983)

[28] arXiv:astro-ph/0602190v1

[29] T. Stanev, High Energy Cosmic Rays, pp 92-96

[30] J. Cronin, T.K. Gaisser, and S.P. Swordy, Sci. Amer. v276, p44 (1997)

[31] M. S. Longair, High Energy Astrophysics v2, p 40

[32] G.V. Kulikov and G.B. Khristiansen, Zh. Eksp. Teor. Fiz. 35 (1958) 635

[33] Cocconi G 1996 Astropart. Phys. 4 2813

[34] V.S. Berezinsky, S.I. Grigorieva, Astron. Astrophys. 199 (1988) 1.

[35] V. Berezinsky, A.Z. Gazizov, S.I. Grigorieva, Phys. Lett. B 612 (2005) 147-153

[36] V. Berezinsky, A.Z. Gazizov, S.I. Grigorieva, Phys. Rev. D 74, 043005 (2006)

[37] T. Stanev, High Energy Cosmic Rays, pp 210-217

[38] A. M. Hillas, The Origin of Ultra-High-Energy Cosmic Rays, Ann. Rev. Astron. Astroph. 22, 425 (1984).

[39] C. A. Norman, D. B. Melrose & A. Achterberg, Ap. J., 454, 60 (1995)

[40] T.E. Clarke, P.P. Kronberg & H. Böringer, Ap. J. 547,, L111 (2001)

[41] H. Kang, D. Ryu & T.W. Jones, Ap. J., 456, 422 (1996)

[42] J.P. Rachen & P.L. Biermann, Astron. Astrophys., 272, 161 (1993)

[43] http://www.shef.ac.uk/physics/teaching/phy320/topic7new.html

[44] http://www.des.umd.edu/pics/rs/photon.gif

[45] F. Halzen & E. Zas, Ap. J., 488, 669 (1997)

[46] A.P. Szabo & R.J. Protheroe, Astropart. Phys., 2, 375 (1994)

[47] M. Milgrom & V. Usov, Ap. J., 449, L37 (1995)

[48] M. Vietri, Ap. J.,453, 883 (1995)

[49] E. waxman, Ap. J., Phys. Rev. Lett.,386 (1995)

[50] C. Cesarsky & V. Ptuskin, Proc. 23rd Int. Cosm. Ray Conf. (Calgary), 2, 341 (1993)

[51] C.T. Hill, Nucl. Phys., B224, 469 (1983)

[52] C.T. Hill, D.N. Schramm & T.P. Walker, Phys. Rev., D36 1007 (1987)

[53] V.S. Berezinsky & A. Vilenkin, Phys. Rev. Lett., 79, 5202 (1997)

[54] M. Birkel & S. Sarkar, Astropart. Phys.,9 ,297 (1998)

[55] T. Weiler, Astropart. Phys., 11, 303 (1999)

[56] D. fargion, B. Mele & A.Salis, Ap. J., 517, 517 (1999)

[57] arXiv:0704.3721v1 [astro-ph]

[58] T. Stanev, High Energy Cosmic Rays, pp 62-65

[59] L.A. Anchordoqui, M.T. Dova, L.N. Epele and J.D. Swain, Phys. Rev. D 55, 7356 (1997) [arXiv:hep-ph/9704387]

[60] V.S. berezinsky and G.T. Zatsepin, Phys. Lett. B 28, 423 (1969)

[61] F.W. Stecker, Astrophys. J. 228, 919 (1999)

[62] arXiv:astro-ph/0506128v3

[63] R.J. Proteroe & P.A Johnson, Astropart. Phys.,4 , 253 (1996)

[64] E. Fermi, Phys. Rev. 75, 1169 (1949)

[65] T. Stanev, High Energy Cosmic Rays, pp 65-72

[66] http://www.cosmic-ray.org/

[67] http://www.physics.adelaide.edu.au/astrophysics/hires/index.html

[68] Nucl. Instr. & Meth. in Phys. Res. A311 (1992) 338-349

[69] http://www-akeno.icrr.u-tokyo.ac.jp/AGASA/

[70] http://www.auger.org/

[71] Nucl. Instr. & Meth. in Phys. Res. A588 (2008) 221-226

[72] M. S. Longair, High Energy Astrophysics v2, p 353

[73] Chandra

[74] M. S. Longair, High Energy Astrophysics v2, pp 307-327

[75] M. S. Longair, High Energy Astrophysics v1, pp 131-139

[76] M. S. Longair, High Energy Astrophysics v1, p 133

[77] Jem-EUSO Blue Book

[78] Auger Collaboration, Science, Vol. 318. no. 5852, pp. 938 - 943

[79] Gorbunov et al. , http://arxiv.org/pdf/0711.4060

[80] J. Mattews, A. P. 22 (2005) 387-397

[81] KASCADE proposals: http://www-ik.fzk.de/KASCADE_home.html

[82] K. Greisen, Phys. Rev. Lett. 16, 748 (1966).

[83] G. T. Zatsepin and V. A. Kuzmin, J. Exp. Theor. Phys. Lett. 4, 78 (1966), [ZhETF Pisma 4 (1966) 114117]

[84] M. Takeda et al., Astropart. Phys. 19, 447 (2003).

[85] K. Shinozaki, in Proc. Quarks 2006, an AGASA reanalysis in which the number of events above 1020 eV is reduced from 11 to 6.

[86] Auger collaboration

[87] A. N. Bunner, Ph.D. thesis, Cornell University (1967).

[88] P. Sommers, Astro. Ph., Vol. 14, 4, Jan 2001, P. 271-286

[89] Ch. Leinert et al., "The 1997 reference of diuse night sky brightness"

[90] EUSO Report on the Phase A Study

[91] Super-"Extreme Universe Space Observatory", Proposal submitted to ESA in response to the call for Cosmic Vision 2015-2025

[92] H. Falke et al. , Nature ,435 (2005) 313

[93] H. Falke, P. Gorham, Ap. Ph. 19 (2003) 477-494

[94] EUSO Proposal

[95] Linsley J. 1979, Call for project and ideas in High Energy Astrophysics

[96] http://www.telescopearray.org/outreach/detect.html

[97] M. Lemoine ,G. Sigl , Physics and astrophysics of ultra high energy cosmic rays, p 29

[98] R. Gandhi, et al , Phy. Rev. D58 093009 (1998)

[99] "Fresnel lenses" , Fresnel technologies inc.

[100] http://root.cern.ch/

[101] http://root.cern.ch/root/doc/RootDoc.html

[102] http://www.ge.infn.it/euso/main/Software/htmldoc SlastShowerGenerator.html#SlastShowerGenerator:description

[103] D.V. Naumov, SLAST: Shower Initiated Light Attenuated to the Space Telescope, LAPP-EXP-2004-02, 2002.

[104] S. Bottai, M. Tognetti, Proton and Neutrino simulation with UNISIM , EUSO int. rep. 2001

[105] D. Heck at al., The CORSIKA Air Shower Simulation Program, FZKA report-6019, ed. FSK, Karlsruhe, 1998

[106] J. Ninkovi et al., Nucl. Instr. Meth. A572 (2007) 454.

[107] D. De Marco, M. Pallavicini, Euso Simulation and Analysis Framework

[108] http://en.wikipedia.org/wiki/Monte_Carlo_method

[109] R. Pesce "Chip Tracking Trigger in ESAF" , Talk given at LPSC, Grenoble, oct 6 2005

[110] M. Bertaina "The Track Trigger Algorithm for the Jem-EUSO experiment"

[111] M. Pallavicini, A Thea, "Euso Simulation and Analisys Framework User Guide" ,Feb 26, 2004

Acknowledgements

I want to thank Mario Bertaina, Roberto Pesce and Dimitry Naumov for their precious help in developing ESAF and for their patience...

I want to thank also Yoshiya Kawasaki, Alessandro Zuccaro, Dieter Horns and Alessandro Thea for their their useful hints and for having provided me many useful things for the code.

Furthermore I want to thank my "german" and my italian tutor: Andrea Santangelo and Stefano Vitale.

I want to thank Nikolai von Krusenstiern for helping me with computer related problems.

Thanks to Benjamin Mück who corrected the german conclusions.

Thanks also to my office colleagues Dima, Santina, Alex, Victor, Benni and Gabriele who made possible a daily exchange of useful informations, suggestions and in the end made this year much more pleasant.

Thanks also to the coffee break people for the time we spent together at lunch time.

Thanks to all the people who helped me in those exhausting months before coming to Tübingen.

Thanks to all the people I met in those years in Trento and Tübingen. This has been a wonderful experience.

Thanks to my family and especially to my parents who made it possible.

Grazie, Danke, Thanks.

Erklärung

Hiermit erkläre ich, dass ich die Arbeit selbständig verfaßt und keine anderen als die angegebenen Quellen und Hilfsmitteln benutzt habe.

Tübingen, 18 Juni 2008

Francesco Fenu